

The Pennsylvania State University

The Graduate School

Department of Chemistry

**THE CHARACTERIZATION OF POLYMER THIN FILMS USING VIBRATIONAL
SPECTROSCOPY**

A Dissertation in

Chemistry

by

Tawanda James Zimudzi

© 2016 Tawanda J. Zimudzi

Submitted in Partial Fulfillment
of the Requirements
for the Degree of

Doctor of Philosophy,

December 2016

The dissertation of Tawanda J Zimudzi was reviewed and approved* by the following:

Michael Hickner
Associate Professor of Material Science and Engineering
Dissertation Advisor
Co-chair of Committee

John Asbury
Associate Professor of Chemistry
Co-chair of Committee

Miriam Freedman
Assistant professor of Chemistry

Seong Kim
Professor of Chemical Engineering

Kenneth Feldman
Professor of Chemistry,
Chemistry Graduate Program Chair

*Signatures are on file in the Graduate School

ABSTRACT

The overriding theme of this thesis is the characterization of thin polymer films synthesized on gold and silicon substrates using a variety of Fourier transform infrared (FTIR) techniques. We demonstrated that the peak shifts observed in surface overlayer attenuated total reflection (SO-ATR) were a result of the changing polarization in the z-axis of the experimental geometry. We leveraged the signal enhancement provided by SO-ATR and reflection absorption infrared spectroscopy (RAIRS) to obtain high quality spectra of samples below 50nm thick. By combining this signal enhanced spectroscopy with transmission and ATR we were able to obtain chemical and structural information which we report in this thesis.

Spin cast NAFION samples were prepared on silicon native oxide and gold substrates with film thicknesses ranging from 5 nm to 250 nm. The influence of NAFION film thickness on the infrared spectrum of the polymer was investigated in SO-ATR geometry at incident angles between 60° and 65°. In the grazing angle SO-ATR geometry, the thickness of the film significantly affected the position and absorbance of characteristic peaks in the FTIR spectrum of NAFION. Two major peaks in the NAFION spectrum at 1220 cm⁻¹ (predominantly $\nu_{as}(\text{CF}_2)$ and $\nu_{as}(\text{SO}_3^-)$) and 1150 cm⁻¹ (predominantly $\nu_{as}(\text{CF}_2)$), appeared to systematically blueshift to 1256 cm⁻¹ and 1170 cm⁻¹, respectively, as the thickness of the film decreased from 250 nm to 5 nm. The changes in the NAFION thin film FTIR spectrum can be attributed to two factors; (1) ordering of NAFION at the interface during spin coating and film formation and (2) the increase in the p-polarization character of the infrared evanescent wave as the polymer film became thinner between the attenuated total reflection (ATR) crystal and the film substrate overlayer. The increase in p-polarization resulted in an increase in characteristic peak absorbance of dipoles aligned normal to the substrate due to the overlayer enhancement of the electric field with NAFION films on Si or Au film substrates. These

results show that the specific thin film sampling geometry, especially in ATR experiments, must be considered to rationally quantify changes in NAFION thin film infrared spectra.

Highly crosslinked aromatic polyamides are of significant importance due their use in water treatment membranes. We present an FTIR study of polyamide films prepared by interfacial polymerization and molecular layer by layer deposition that are used as reverse osmosis (RO) membranes. We assign the aromatic ring modes that occur in the fingerprint region and demonstrate that the peak at 1492 cm^{-1} is due solely to the B1 bending stretch mode of the meta bi functionalized ring that originates from the m-phenylenediamine (MPD) molecule. We assign the peak at 1243 cm^{-1} to the amide N-H vibration and demonstrate that it is a good alternative to the Amide II peak for swelling studies on polyamide films. The free acid peak in mLbL samples decreases in intensity as film thickness increases which is indicative of increasing crosslink density. The free acid content in mLbL films was found to be higher than that observed in interfacially polymerized films. The growth of the initial layers of mLbL polyamide film differs on gold and silicon substrates with MPD displacing the initial monomer on gold. At cycle numbers beyond 10 however film growth on the two substrates was found to be indistinguishable. The growth rate of mLbL films is also affected by the solvent selected to rinse excess polymer with thicker films consistently observed for isopropyl alcohol rinsed films.

Molecular layer by layer assembled polyamide films were synthesized on smooth gold and silicon wafer with native oxide substrates. The orientation of the amide C=O and disubstituted aromatic rings were analyzed using surface overlayer attenuated total reflection (SO-ATR) and reflection absorption infrared spectroscopy (RAIRS). It was determined that on both substrates there was strong ordering for films 10 cycles thick or lower with an average tilt angle of 16° from the surface normal for the C=O group and 84° . This tilt angle translates to an orientation with the

aromatic ring laying close to flat on the surface with an average angle of 6° . FTIR and NEXAFS measurements further showed high anisotropy at low cycle numbers which completely disappeared at cycle numbers greater than 60. The acid concentration in mLbL films was characterized by interpolating integrated absorbance values of the free acid band at 1718cm^{-1} into a calibration curve line generated from interfacially polymerized samples of known acid content. The acid content in samples synthesized on silicon was found to be higher than that for samples generated on gold at low cycle numbers. The acid content ranged from 0.13 mmol.g^{-1} for 60 cycles to 0.56 mmol.g^{-1} for 5 cycles on silicon substrates. On gold however, the acid content ranged from 0.12 mmol.g^{-1} at 5 cycles to 0.35 mmol.g^{-1} at 12 cycles. On both substrates the acid content decreased as the cycle number increased and as the cycle number increased and at higher cycle numbers there was very little difference between the acid content of samples synthesized on gold and silicon.

TABLE OF CONTENTS

List of Figures	viii
List of Tables	xiii
Acknowledgements.....	xiv
Chapter 1 Introduction	1
1.1 Background	1
1.2 Motivation.....	3
1.3 References.....	7
Chapter 2 Literature Review	9
2.1 Introduction.....	9
2.2 Current Approaches to Thin Film Research.....	11
2.2.1 Analytical methods and challenges	11
2.2.2 Vibrational methods in fuel cell and RO thin film research.....	13
2.2.3. Signal enhanced FTIR methods	14
2.3 Current State Fuel Cell Ion Exchange Membrane Research.....	21
2.3.1 Proton exchange membranes.....	21
2.3.2 FTIR analysis of NAFION thin films.....	24
2.3.3 Perspective on ion exchange membrane research beyond NAFION	27
2.4 Probing Microstructure in Reverse Osmosis Membranes.....	28
2.4.1 Current state of polyamide RO membrane research.....	28
2.4.2 molecular Layer by Layer synthesized polyamide RO membranes	33
2.5 Conclusion	35
2.6 References.....	37
Chapter 3 Experimental Techniques: Theory And Applications	44
3.1 Introduction.....	44
3.2 Materials and Sample Preparation	44
3.2.1 NAFION thin films	44
3.2.2. Polyamide thin film composite membranes	46
3.3 Fourier Transform Infrared Spectroscopy (Ftir) Sampling Methods	47
3.4 SO-ATR Sampling Geometry	48
3.5 Spectral Simulation and Determination of Optical Constants.....	56
3.6 Determination of Orientation from Simulated and Experimental Spectra	61
3.7 References.....	63
Chapter 4 FTIR Analysis of Alignment in NAFION Thin Films at SiO ₂ and Au Interfaces	68
4.1 Introduction.....	68

4.2 Experimental Methods	72
4.2.1 FTIR sampling.....	72
4.2.2 Thin film preparation	72
4.3 Results and Discussion.....	74
4.3.1 Peak deconvolution and peak assignments	74
4.3.2 Effect of polarization on the ATR spectrum of NAFION	75
4.3.3 Orientation of NAFION on planar substrates.....	77
4.4 Conclusions.....	85
4.5 Supplementary Information	86
4.6 References.....	90
 Chapter 5 Understanding The Fingerprint Region in The Infra-Red Spectra Of Aromatic Polyamides	 95
5.1 Introduction.....	95
5.2 Methods.....	98
5.3 Results and Discussion.....	100
5.3.1 Fingerprint region peak assignment	100
5.3.2 Effect of sample preparation	106
5.3.3 Effect of hydration	110
5.4 Conclusion	112
5.5 Supporting Information.....	114
Aromatic Ring vibrations	114
5.6 References.....	122
 Chapter 6 Acid Content and Orientation Of Thin Polyamide Reverse Osmosis Membrane Films On Non-Porous Substrates	 126
6.1 Introduction.....	126
6.2 Methods.....	128
6.3 Results and Discussion.....	129
6.3.1 Orientation.....	129
6.3.2 Acid content	135
6.6 References.....	143
 Chapter 7 Summary of Findings and Directions for Future Research	 148
7.1 CONCLUSIONS.....	148
7.1.1 FTIR Analysis of Alignment in NAFION Thin Films at SiO ₂ and Au Interfaces	 148
7.1.2 Understanding the Fingerprint region of aromatic polyamide	150
7.1.3 The acid content and Orientation of molecular Layer by Layer polyamide films on silicon and gold substrates.....	 152
7.2 Future Work	155
7.2.1 In situ structure and composition changes	155
7.2.2 Analyzing the hydrogen bonding network in polymer thin films	158
7.2.3 Azides as an alternate probe for HOD in thin polymer films	160
7.3 References.....	164

LIST OF FIGURES

Figure 1-2. Schematic of a PEMFC. The proton exchange membrane is shown in blue, the catalyst layer is shown in grey, the gas diffusion layer is shown in black and the anode and cathode are labeled with a zoom in box showing the catalyst and gas diffusion layers where electron transport takes place.	4
Figure 1-2. Cartoon and transmission electron microscope representation of thin film composite membrane consisting of a polyamide active layer, polysulfone porous support and polyester non-woven fabric. A TEM image shows the relative thickness of each layer.	5
Figure 2-1. Schematic of three geometries used in SEIRA experiments.	15
Figure 2-2. Model interaction of incident radiation with metal island substrate with dielectric constant ϵ_m coated with adsorbate molecules with dielectric constant ϵ_d and b) the resultant lightning rod effect on an ellipsoidal particle. The electric field intensifies along major axis resulting in electric field hot spots between metal islands.	17
Figure 2-3. Image dipole effect, the surface parallel induced dipole is annihilated by the image dipole in the metal while the surface normal induced dipole is enhanced.	18
Figure 2-4. a) Repeat unit of NAFION and b) schematic representation of the phase separated morphology of NAFION with well-defined nano-channels. ⁸⁹	21
Figure 2-5. Catalyst layer carbon supported Pt nanoparticle coated with NAFION. ³¹	22
Figure 2-6. Proposed morphologies of Nafion thin films on silicon substrates at different thickness regimes ranging from highly oriented single layers below 4 nm to mixed morphology films above 55 nm.	23
Figure 2-7. ATR spectrum of bulk Nafion membrane similar to that used in MEA hydration studies overlayed with the corresponding Nafion thin film spectrum on a gold substrate. The water peaks and 1260 cm^{-1} peak discussed in the text are labelled.	25
Figure 2-8. Schematic for typical interfacial polymerization synthesis of aromatic polyamide (PA) on polysulfone (PES) support to form dense PA film	29
Figure 2-9. Network and aggregate pores proposed by Kim et al. Network pores are formed within highly crosslinked chains while aggregate pores are formed between loosely crosslinked chains. ⁷⁷	31
Figure 2-10. Schematic representation of the mLbL synthesis process on silicon substrates, using TMC and MPD as the monomers. ⁸⁶	33
Figure 2-11. Comparison of AFM height images of 30 cycle mLbL polyamide (Right) and commercial polyamide (Left) plotted using the same height scale. ⁸⁶	34

Figure 3-1. the experimental geometry of an SO-ATR experiment the evanescent wave propagating through the sample can be envisaged as comprising of some components in x y and z directions labelled.	49
Figure 3-2. Three-layer optical system of the SO-ATR geometry showing reflection and transmission of an incident beam through the three-layer system, only one of the multiple internal reflections within the film is shown.....	50
Figure 3-3. Optical absorbance at 1050 cm^{-1} as a function of thickness for a NAFION film on a silicon substrate based on parameters in Table 2.	53
Figure 3-4. P-factors calculated from Equations 16-17 for a 50 nm NAFION film in (a) grazing angle ATR and (b) SO-ATR geometry. P-polarization is represented by the solid lines and s-polarization by the dashed lines. Note the different scales.	56
Figure 3-5. Parallel slab model for a multiphase, parallel-layer sample consisting of a total of N phases. Light approaches the sample from infinite phase 1 at an angle of incidence ϕ_1 The directions of the electric field for s (out of plane) and p (in plane) polarizations are shown for incoming and outgoing propagation directions, designated by + and - superscripts, respectively.	57
Figure 3-6. Flow chart depicting the determination of molecular ordering from experimental and calculated spectra. The simulated spectrum is calculated as parallel-layer multislabs system where the optical properties and thickness of each layer is defined by the experimental geometry and sample thickness.	62
Figure 4-1. Experimental SO-ATR absorbance at 1050 cm^{-1} overlayed with a) transmission for silicon samples and b) reflection for gold samples.	76
Figure 4-2. Experimental values for NAFION absorption at 1050 cm^{-1} on a native oxide silicon substrate overlayed with predicted values.	77
Figure 4-3. Position of $\text{CF}_2/\text{SO}_3^-$ peak maximum as a function of film thickness for grazing angle ATR with s-polarized, p-polarized, and unpolarized light.	78
Figure 4-4. S and p-polarized ATR spectra of bulk NAFION film in grazing angle ATR geometry.....	79
Figure 4-5. NAFION film, 250 nm thick, on silicon substrate s-polarized and p-polarized in SO-ATR geometry.	80
Figure 4-6. NAFION film, 50 nm thick, on silicon substrate s-polarized and p-polarized in SO-ATR geometry.	81
Figure 4-7. Unpolarized SO-ATR spectra of 5 nm and 50 nm thick NAFION on a silicon substrate.	82
Figure 4-8. SO-ATR spectra compared to a) transmission for a 10 nm film on a silicon substrate and b) reflection for a 5 nm film on a gold substrate.	83

Figure 4-9. Ordered conformation of NAFION on surface for thin films where the backbone $\nu_{as}(\text{CF}_2)$, side chain $\nu_s(\text{SO}_3^-)$ and $\nu_{as}(\text{CF}_3)$ dipole changes are in the plane of the p-polarized z component of the evanescent wave.	84
Figure 4-10. Orientation of dipole changes relative to the surface for a molecule with C_{3v} symmetry undergoing a) a symmetric stretch and b) an asymmetric stretch.	85
Figure 4-11. P-factors calculated for a 50 nm NAFION film in SO-ATR (solid lines) and ATR geometry (dashed lines).	86
Figure 4-12. p polarized ATR spectra of a 500 nm NAFION film spin cast directly onto a hemispherical silicon ATR crystal.	88
Figure 4-13. s and p-polarized spectra of a) a 50 nm and b) a 500 nm NAFION film spin cast directly onto a silicon hemisphere. All spectra were collected at 65° incident angle.	88
Figure 4-14. P-Polarized spectra of 500nm and 50 nm thick films overlaid.	89
Figure 5-1. Chemical structures of monomers used in synthesis of mLbL films and the TMC-MPD fragment used in DFT calculations.	100
Figure 5-2. RAIRS spectrum of 60 cycle LBL PA film on gold showing the fingerprint region from 1000 cm^{-1} to 1800 cm^{-1} showing the three regions of peak deconvolution.	101
Figure 5-3. Low cycle number spectra overlayed with TMC spin cast on a gold substrate showing the peak position of free acid COO^- groups. The peak numbers correspond to the numbers in the body of the text.	102
Figure 5-4. a) The three main peaks of region II and b) the spectrum of TMC-MPD poly(amide) overlayed with that of TMC-DABA poly(amide). Both samples are 30 cycles on a gold substrate. The peak numbers correspond to the numbers in the body of the text.	104
Figure 5-5. a) Region III for a 60 cycle LBL film on gold and b) the spectrum for the corresponding region in an IP film with peak numbers corresponding to peak numbers in the body of the text.	105
Figure 5-6. a 2 cycle mLbL film on gold substrate showing spectral differences when rinsed by IPA and acetone and b) corresponding plot for a 60 cycle sample on gold. All spectra were normalized to the 1612 cm^{-1} peak	107
Figure 5-7. SO-ATR spectra of the initial mLbL cycles on a) silicon and b) gold substrates ..	108
Figure 5-8. XPS spectra of the first layer of mLbL film growth, cycle 0.5 is the deposition of TMC monomer and cycle1 is the deposition of MPD.	109

Figure 5-9. a, dry and Hydrated transmission spectra of interfacially polymerized TMC-MPD films and b) the peak position of the amide II peak (1532 cm^{-1}) and N-H bending mode as a function of time exposed to water vapor at 90% RHF	111
Figure 5-10. peak shifts observed in amide I and δ N-H peak for aa 60 cycle sample on gold exposed H_2O vapor at 90% RH.....	112
Figure 5-11. Cartesian coordinate representation of bending stretching vibrations 18 and 19 of MPD rings ²⁴	115
Figure 5-12. Fit of the MPD spectrum between 1350 cm^{-1} and 1800 cm^{-1} showing the positions of the major peaks of vibrations 8 and 19.....	116
Figure 5-13. the atomic motion in vibrations 18 and 9 of TMC and their observed peak positions in the monomer IR spectrum ²⁴	117
Figure 5-14. ATR spectrum of Neat TMC.....	117
Figure 5-15. Transmission spectrum of delaminated interfacially polymerized polyamide film which has not been adequately rinsed overlaid with one that has been thoroughly isolated over a 72-hour period.	118
Figure 5-16. XPS spectra of 1.5 – 10 cycle mLbL samples prepared on gold.....	120
Figure 6-1. The n and k spectrum in the MIR region used as accepted optical constants for spectral simulation.....	130
Figure 6-3. The tilt angle of the C=O bond of the amide group with respect to surface normal on gold and silicon substrates	132
Figure 6-4. Tilt angle of the disubstituted aromatic ring with respect to the surface.....	133
Figure 6-5. Angle dependent NEXAFS spectra of a) half cycle and b) 10 cycle mLbL samples showing the anisotropy of the antibonding C=C pi orbitals.....	134
Figure 6-6. a) the FTIR spectrum of the amide I peak showing the components added into the fitting model and b) the calibration line obtained by a beers law plot of the intensity of the free acid component in a.	136
Figure 6-7. The acid content of 5 - 60 cycle mLbL films synthesized on gold and silicon samples.....	137
Figure 6-8. The optical constants used to compute mLbl spectra.....	139
Figure 6-9. NEXAFS spectra of mLbL films synthesized on amino silane terminated silicon, this figure is analogous to figure 6-4 in the results and discussion section.	140
Figure 7-1. Ordered conformation of NAFION® on surface for thin films where the backbone $\nu_{\text{as}}(\text{CF}_2)$, side chain $\nu_{\text{s}}(\text{SO}_3^-)$ and $\nu_{\text{as}}(\text{CF}_3)$ dipole changes are in the plane of the p-polarized z component of the evanescent wave.	149

Figure 7-2. Experimental setup of the MEA-type cell for the in situ ATR-FTIR measurements at the NAFION–Pt/C and Pt3Co/C	155
Figure 7-3. Spectroelectrochemical cell used in SEIRA experiments ¹⁶	157
Figure 7-4. Figure 7-4 The OD stretch deconvolution of PS-S1 at a λ of 1.7 μ m. Hydration was obtained for each membrane by introducing the sample to 10% HOD vapor at 30% relative humidity. ²³	158
Figure 7-5. OD region of 30 cycle mLbL films exposed to 10 mol % HOD water vapor at 90% relative humidity	160
Figure 7-6. The antisymmetric stretching mode of the azide ion as a function of ω in reverse micelles formed using (a) AOT (b) Igepal and (c) CTAB surfactants. The dashed line is the frequency of an azide in bulk water. ³⁰	161
Figure 7-7. Figure 7-7 Structure of QAPPO samples discussed in the text where x is the degree of functionalization and y-2 is the number of carbons after the quaternary ammonium group	161
Figure 7-8. Peak position of azide asymmetric stretch as a function of hydration number for QA ppo sample of different cross linker length. This plot is analogous to fig 7-6 for reverse micelles the insert shows the spectrum of BTMA as the hydration number increases	162
Figure 7-9. a) Swelling strain measured by QCM as a function of humidity ³¹ and b) azide asymmetric stretch measured as a function of relative humidity.	163

LIST OF TABLES

Table 3-1. Modeling parameters used to simulate optical absorbance of NAFION in grazing angle SO-ATR.....	53
Table 4-1. Weight percent NAFION solutions for spin coating and resulting film thickness by ellipsometric measurements.	73
Table 4-2. Peak assignment for predominant peaks in the NAFION ATR spectrum.	75
Table 4-3. Penetration depth for ATR calculated at 1250 cm^{-1} under s and p-polarization in ATR on a silicon hemisphere.....	87
Table 5-1. Thickness of mLbL samples as determined by Ellipsometry	118
Table 5-2. Thickness of mLbL samples prepared with IPA or acetone rinse as measured by spectroscopic ellipsometry	119
Table 6-1. The acid content of the final KBr mixture used to generate pellets for calibration curve.....	135
Table 6-2. The fitting parameters used to obtain unscaled intensities of the free acid component of the amide I peak.	141
Table 6-2. The average acid content as determined by FTIR and curve fitting	142

ACKNOWLEDGEMENTS

I must first thank my advisor, Dr. Michael Hickner, for his guidance and for allowing me the opportunity to conduct research in his group and affording me the intellectual freedom and to explore and express my ideas. I would like to thank the members of my thesis committee, Dr. Asbury, Dr. Freedman and Dr. Kim, for contributing their expertise and insight along the way. I would also like to thank Dr. James Sturnfield and Dr. Robert Cieslinski from Dow chemical for providing valuable advice and material support that facilitated the completion of this work. I would also like to thank Douglas Kushner for his help with spectroscopic Ellipsometry, Ian McCrum for his assistance with DFT calculation.

I would also like to express my gratitude to Dr. Christopher M. Stafford (NIST) and Dr. Joshua Stapleton (Materials Characterization lab) to whom I vented my frustrations about temperamental M.C.T detectors and discussed all manner of sublunary matters including the true definition of a good doughnut.

I would like to thank my colleagues, collaborators and good friends in the Hickner research group, Harrison Jasper Cassady, Clara Capparelli, Sarah Smedley, Praveen Meduri, Geoff Geise, Changwoo Nam, Jiho Seo, Jing Pan, Juanjuan Han and William Ferrel. I would like to thank my PSU friends, Florian Baumann, Han Song, Christopher Greico, Welly Loc, Yan Cheng and Zhongwei Hu. Finally, I wish to express my deep gratitude to my family who in the face of trying times provided unwavering support and encouragement.

The Eleven Phases of an Experiment

1. Wild enthusiasm
2. Exciting commitments
3. Total confusion
4. Re-evaluation of goals
5. Disillusionment
6. Cross-accusations
7. Search for the guilty
8. Punish the innocent
9. Promote the non-participants
10. Verbally assassinate visible leaders
11. Write and publish the report

-Scientifically Speaking: A Dictionary of Quotations

Chapter 1

Introduction

1.1 Background

Clean energy and reliable access to potable water are among the biggest challenges the world faces today. While the recent advances in hydraulic fracturing have gone a long way in addressing the availability of energy, these technologies have done little to abate concerns about the effects of fossil energy on the Earth's ecosystem. Due to these concerns, electrochemical energy production and storage such as fuel cells and batteries as alternatives to fossil fuels has garnered significant attention. According to the environmental protection agency the transportation sector contributes 14% of the global greenhouse gas emissions and these concerns have led to significant interest in developing ¹a fuel cell electric vehicle. Since 1996 there has been a significant increase in research output supported by major motor vehicle manufactures and government agencies in developing fuel cell, lithium batteries and polymer supercapacitors.² The over the last 20 years great strides have been made in bring a commercial fuel cell electric vehicle into fruition culminating in the 2016 launch of the first consumer fuel cell vehicles the Toyota Mirai and Hundai Tuscon.³

However, the cost of fuel cells is still high compared to internal combustion engine vehicles due to the platinum group metals (PGM) used in fuel cells and the high manufacturing cost of membrane materials and electrochemical stacks. The US department of energy has set a PGM target of 11.3 g_{PGM} by the year 2020 which is still much higher than the less than 5g_{PGM} in current gas vehicles catalytic converters.⁴ In fuel cells, platinum is the main PGM used while in gasoline cars it has mostly been replaced by less expensive PGMs in catalytic converters. Some researchers have

suggested that for large scale adoption of fuel cell electric vehicles to become a reality these vehicles must be affordable and this is only possible if approximately 6 g of Pt are used per vehicle.⁵ According to the DOE, in the last decade the automotive fuel cell system cost has dropped from \$124/kW to \$55/kW but is still above the target \$30/kW.⁶ Another contributing factor to the expense of PEMFCs is the high cost of production and degradation at high temperatures of NAFION, one of its integral components. In a PEMFC, NAFION acts as a binder for the Pt catalyst as well as a separator between the two electrodes, allowing only the transport of protons to complete the half reactions.⁷ NAFION demonstrates a combination of oxidative and chemical stability while also possessing high conductivity at low relative humidity unrivaled by its alternatives.⁸ Two lines of research prevail as it pertains to fuel cells, one focused on finding alternatives to NAFION and PEMs in general, and another focused understanding and improving on current PEM technology. To this end it has been widely accepted that understanding how NAFION interacts with the platinum catalyst hold the key to reducing the amount of Pt required in fuel cells and increasing their performance.

It is estimated that less than one percent of the freshwater on earth is suitable for human consumption.⁹ The removal of salts from sea water and brackish water is the most advanced technology used to address the increasing demand for fresh water. Desalination offers a source of water otherwise not accessible for irrigational, industrial and municipal use. The multi-stage flash (MSF) distillation¹⁰, multi-effect distillation (MED)¹¹, electrodialysis (ED)¹², nanofiltration (NF) and reverse osmosis (RO)¹³ have all been used to desalinate sea water with RO making up 50% global installations due to its lower energy consumption. The greatest demand for desalination installations is the in Middle East where historically thermal based technologies such as MSF have dominated due to availability and low cost of fossil fuels. In recent years however the Middle East

has seen a surge in demand for RO technologies which is mirrored by similar growths in demand for RO installations in Asia and Europe.

RO based separation relies on a semi permeable membrane which under an applied pressure obstructs salt permeation hence preferentially allowing water molecules to pass through it. The performance of these membranes is characterized by the water flux and salt rejection with an ideal membrane possessing a high water flux and salt rejection higher than 99%. Accomplishing these metrics while resisting chloride degradation is possible by developing chemistries that allow the fine tuning of acid concentration (which is tied to water flux) crosslink density (which is tied to salt rejection). While decades of research have been dedicated to understanding and improving RO technology, the gains thus far have been relatively marginal primarily due to local chemical inhomogeneity and high surface roughness. The recent development of smooth, chemically homogeneous molecular layer by layer synthesized RO membranes on planar nonporous substrates by NIST opens up FTIR as a route to research both RO and NF membranes and make meaningful progress in improving the current technologies.

1.2 Motivation

In both PEMFC and RO membrane research, the problem of polymer thin film analysis has limited the tools available to probe the structural and chemical properties of these systems. FTIR is often the method of choice when studying the structure and chemistry of polymer films due to the ease of sample preparation and the wealth of knowledge that exists in literature to aid spectral interpretation. However, when the thickness of the polymer film falls below 100 nm, only infrared reflection absorption spectroscopy (IRRAS) becomes the only feasible option. A key motivation of this work is the development of an alternative FTIR sampling geometry that provides signal quality

equivalent or superior to IRRAS without the substrate limitation of IRRAS would provide a valuable alternative to interrogate thin film systems.

A PEMFC consists of an anode and a cathode, which provide the oxidation and reduction half reactions, a gas diffusion layer (GDLs), catalyst layers and a PEM, which acts as a separator to prevent the mixing of the reactants, a conductor for protons, and provides structural support Figure 1-1. While the structure and processes in the PEM are well studied relatively less is known about ionomers in the catalyst layer.

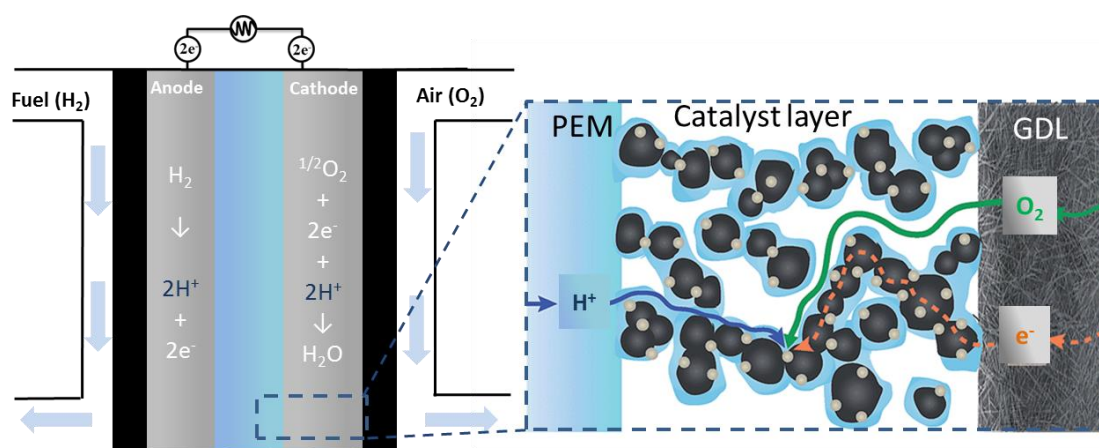


Figure 1-1. Schematic of a PEMFC. The proton exchange membrane is shown in blue, the catalyst layer is shown in grey, the gas diffusion layer is shown in black and the anode and cathode are labeled with a zoom in box showing the catalyst and gas diffusion layers where electron transport takes place.¹⁶

The majority of FTIR work on fuel cell ionomers has been focused on understanding hydration effects in NAFION films and hence has been limited to spectral regions fundamental to understanding hydration.^{14,15} FTIR has been used to study NAFION thin films in attenuated total reflection (ATR), infrared reflection absorption spectroscopy IRRAS and transmission geometries and yet it seems that there is no consensus on understanding the structure and function of ionomers at the electrochemical interface. The main reason for this lack of understanding is the fact that the spectrum of NAFION appears different depending on the sampling geometry. This problem has

been heightened by the fact that studies of NAFION thin films have been conducted on model substrates such as silicon in order to take advantage of alternative characterization techniques such as transmission electron microscopy (TEM), neutron scattering and contact angle measurements. While silicon may be convenient for studying ultrathin films, it presents several complications as a substrate for FTIR studies. A motivation of this research is to obtain high quality vibrational information on silicon substrates which can rationally be compared to spectra collected on alternative substrates and geometries to obtain structural information.

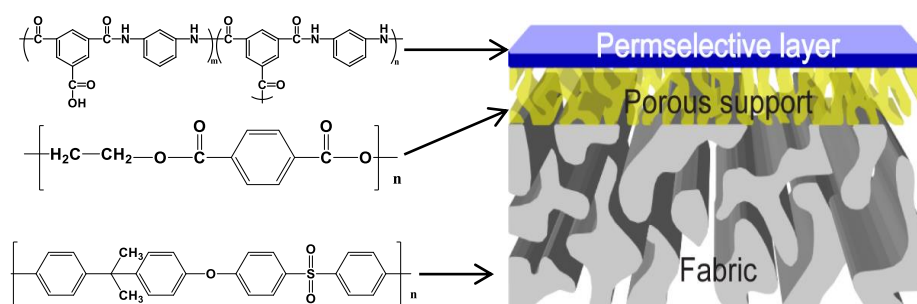


Figure 1-2. Cartoon representation of thin film composite membrane consisting of a polyamide active layer, polysulfone porous support and polyester non-woven fabric.

Typically, commercial and residential RO and NF water treatment systems are constructed as thin film composite (TFC) membranes with an ultrathin thin active layer (20-200 nm) synthesized on a microporous polysulfone substrate which in turn lies above of a reinforcing polyester non-woven support fabric, Figure1-2. The morphology, composition and density of the active layer has significant influence on the transport properties of the membrane, hence great effort has been expended to understand this layer in the hopes of optimizing membrane chemistry and increasing performance. Currently the active layer in thin film composite RO and NF membranes are based on a PA thin-film made by interfacial polymerization of an aromatic polyamine such as m-phenylenediamine (MPD) with aromatic polyacyl halides such as trimesoyl chloride (TMC).

There is still ambiguity about three important properties of these films, the monomer ratio, the cross link density and the orientation.

Detailed information on the nanostructure of the PA active layer is required to achieve a better understanding of the salt rejection and water transport in RO and NF films. By studying mLbL synthesized RO films where it is possible to precisely control the chemistry, we can obtain crucial information about monomer ratio, free acid concentration and orientation using FTIR which is directly relatable to transport properties. Studying such a model system provides the control required to establish unambiguous structure property relationships. The analytical framework developed in studying mLbL membranes can be extended to real composite membranes, aiding in interpreting vibrational data for these films and ultimately leading to a better understanding of how both chemical and structural properties affect the transport characteristics.

Although the focus of this thesis is thin film analysis for materials relevant PEMFC and RO applications, the problem of how to probe polymer films less than 100 nm is a common theme across several fields hence the strategies introduced here can be applied to a variety of systems.

1.3 References

- (1) Greenhouse gas emissions <https://www3.epa.gov/climatechange/ghgemissions/> (accessed Jul 7, 2016).
- (2) Capacitors, E.; Winter, M.; Brodd, R. J. What Are Batteries, Fuel Cells, and Supercapacitors? *Chem. Rev.* **2004**, *104* (10), 4245–4270.
- (3) Sunita Satyapal (US Office of Energy Efficiency & Renewable Energy). The Year of the Fuel Cell: Looking Back to Get Ahead <http://energy.gov/eere/articles/year-fuel-cell-looking-back-get-ahead>.
- (4) Fuel cell Multi-Year research, Development and Demonstration plan http://www1.eere.energy.gov/hydrogenandfuelcells/mypp/pdfs/fuel_cells.pdf.
- (5) Kongkanand, A.; Mathias, M. F. The Priority and Challenge of High-Power Performance of Low-Platinum Proton-Exchange Membrane Fuel Cells. *J. Phys. Chem. Lett.* **2016**, 1127–1137.
- (6) Spendelow, J.; Marcinkoski, J. *DOE Fuel Cell Technologies Office Record*; 2013.
- (7) Holdcroft, S. Fuel Cell Catalyst Layers: A Polymer Science Perspective. *Chem. Mater.* **2013**, *26* (1), 381–393.
- (8) Hickner, M. A.; Ghassemi, H.; Kim, Y. S.; Einsla, B. R.; McGrath, J. E. Alternative Polymer Systems for Proton Exchange Membranes (PEMs). *Chem. Rev.* **2004**, *104* (10), 4587–4611.
- (9) Geise, G. M.; Lee, H.-S.; Miller, D. J.; Freeman, B. D.; McGrath, J. E.; Paul, D. R. Water Purification by Membranes: The Role of Polymer Science. *J. Polym. Sci.* **2010**, *48*, 1685–1718.
- (10) Khawaji, A. D.; Kutubkhanah, I. K.; Wie, J.-M. Advances in Seawater Desalination Technologies. *Desalination* **2008**, *221* (1–3), 47–69.
- (11) Al-Shammiri, M.; Safar, M. Multi-Effect Distillation Plants: State of the Art. *Desalination* **1999**, *126* (1–3), 45–59.
- (12) Strathmann, H. Electrodialysis, a Mature Technology with a Multitude of New Applications. *Desalination* **2010**, *264* (3), 268–288.
- (13) Shenvi, S. S.; Isloor, A. M.; Ismail, A. F. A Review on RO Membrane Technology: Developments and Challenges. *Desalination* **2015**, *368*, 10–26.
- (14) Falk, M. An Infrared Study of Water in Perfluorosulfonate (NAFION) Membranes. *Can. J. Chem.* **1980**, *58*, 1495–1501.
- (15) Schmatko, T.; Colombari, P.; Gruger, A.; Régis, A. Nanostructure of NAFION Membranes

at Different States of Hydration: An IR and Raman Study. *Vib. Spectrosc.* **2001**, 26 (2), 215–225.

- (16) Weber, A. Z.; Kusoglu, A. Unexplained Transport Resistances for Low-Loaded Fuel-Cell Catalyst Layers. *J. Mater. Chem. A* **2014**, 2 (41), 17207.

Chapter 2

Literature Review

2.1 Introduction

As previously established, thin polymer membranes have wide applications in energy technologies and membrane-facilitated water treatment applications. A survey of the literature will reveal that there are host of well-established sensitive techniques that have been used to study thin films even down to the angstrom level. Many of these methods, while excellent for inorganic films, prove challenging when applied to organic polymers, which at times may be fragile, prone to contamination or difficult to handle under ultra-high vacuum.

Vibrational spectroscopy is a powerful technique to identify molecules and to study their structures and reactions at the molecular level. In terms of polymers used in fuel cells and RO membranes, several research groups have used a variety of vibrational spectroscopic methods ranging from non-linear techniques to static methods to probe both structure and function. Fayer¹ has published numerous articles using ultrafast infrared methods to study the structure and dynamics of water in fuel cell membranes.² Watanabe³ has developed an in-situ ATR method to study water transport and structural changes in membrane electrode assemblies (MEA) similar to those found in real fuel cells.⁴

The work of Fayer and Watanabe has provided the basis of studying bulk membranes and our understanding of these films and publications on them are ever increasing. The situation is somewhat different for films below 200 nm where we are still far from understanding the structure property relationships of thin ion-containing polymer films. One problem in studying these thin

films using vibrational spectroscopy has been sensitivity with the standard transmission FTIR or Raman scattering sampling methods simply not being sensitive enough. Osawa⁵ has done extensive work on surface enhanced infrared absorption (SEIRA) using a thin metal layers to enhance the signal in various experimental geometries.^{6,7} The use of metal layers in SEIRA is particularly convenient as the metal layer can be used as an electrode to facilitate in-situ spectroelectrochemical measurements. SEIRA however is still poorly understood and substrates are difficult to fabricate. As a result, only a handful of research groups have been successful in implementing it to study film properties. Milosevic discovered that under specific conditions ATR spectra can be enhanced even in the absence of a metal layer when a grazing angle ATR (GAATR) geometry is used.⁸ With GAATR as with SEIRA, spectral interpretation is complicated by the incomplete understanding of spectral enhancement and band distortions as a function of film thickness.

The following sections will survey the current research strategies employed to study thin films with an emphasis of vibrational methods and the state of understanding with respect to signal enhancements in FTIR. An overview the key challenges and outcomes in fuel cell, NAFION and RO membrane research will also be presented to highlight areas where signal enhanced FTIR can bridge gaps in understanding.

2.2 Current Approaches to Thin Film Research

2.2.1 Analytical methods and challenges

The problem of thin films analysis is often approached by using surface sensitive techniques such as X-ray photoelectron spectroscopy (XPS), Auger electron spectroscopy (AES), electron probe X-ray microanalysis (EPMA), secondary ion mass spectrometry (SIMS), spectroscopic ellipsometry (SE) and Rutherford back scattering (RBS). None of these techniques is intrinsically better than the rest for all studies but each has its own benefits and disadvantages. Typically, two or more of these techniques are combined to provide useful water transport and morphology information.

Kosoglu, et al. have studied water uptake and swelling for NAFION films on platinum, gold and carbon substrates by combining SE which gives changes in film thickness with QCM which gives mass gain.⁹ SE measurement requires fitting changes in wave amplitude and phase shift to optical models to characterize the thickness and complex refractive index of thin polymer films and this fitting procedure requires that the substrate is adequately optically characterized. SE and QCM measurement however cannot provide the molecular level detail about the changes in the film during swelling the vibrational methods can provide.

X-ray techniques are perhaps the most prevalent methods used to elucidate the morphological differences arising from surface interactions and processing conditions for fuel cell ionomer thin films. Grazing incidence small angle x-ray scattering (GISAX) has been used to study the morphology of thin NAFION films as a function of film thickness, substrate type and relative humidity.^{9,10} XPS has been used to study degradation of both fuel cell ionomers and RO membranes and has proven a popular choice in studying variations in RO membrane chemical composition and surface coatings. XPS measurement however cannot be carried out in situ to characterize changes

in the transport characteristics which are of importance in both fuel cell and RO thin films. Soles, et al. has used near-edge X-ray adsorption spectroscopy fine structure (NEXAFS) to assess the impact of surface structure on permeability and transport of water and solutes across the water-membrane interface in LBL films. Additionally, in-situ X-ray relectometry has been used to measure the swelling of LBL films and construct transport models.¹¹ NEXAFS can determine the orientation of aromatic rings in the polyamide polymer but is unable to distinguish between aromatic rings belonging to each of the monomers. XPS also does not allow nondestructive probing of chemical composition gradients in in films being limited only to less than 10 nm of the film.

RBS can probe a greater depth into the sample than XPS and determine the elemental composition and depth profile. RBS experiments on laboratory-made RO membranes have shown that the elemental composition of membrane active layers could be a function of layer depth throughout the entire cross-section.^{12,13} Tof-SIMS has been proposed to study surface coatings on RO membranes¹⁴ and degradation of both RO membranes and fuel cell ionomers, however the destructive nature of depth profiling and the difficulty of spectral interpretation has resulted in very few groups attempting this technique.

Vibrational spectroscopy and FTIR specifically can allow the study of in-situ water uptake and dynamics which permits researchers to conclude which functional groups in the polymer interact with water and the nature of the interactions. FTIR can also facilitate nondestructive depth profiling to analyze chemical heterogeneities in the sample. The ease of sample preparation, low cost of instrumentation, and the versatility and speed of measurements has made has vibrational methods a popular choice to study thin films for fuel cells and RO membranes as is outlined below.

2.2.2 Vibrational methods in fuel cell and RO thin film research

Surface vibrational spectroscopic techniques probe the structure and composition of interfaces at the molecular level in a typically nondestructive manner and with a versatility not easily replicated with other techniques. Vibrational sum frequency generation spectroscopy (VSFG) has been used to study thin perfluorosulfonate ionomer (PFSI) films used in fuel cells. VSFG was employed by Yagi, et al. to probe the PFSI/Pt interface.¹⁵ Yagi, et al. concluded that NAFION thin films thicker than 5 nm form either a macroscopically centrosymmetric orientation or dimer configuration. Noguchi, et al. used VSFG to study the humidity dependent structure of water on thin PFSI film surfaces and demonstrated water molecules adsorbed preferentially at sulfonate sites on the NAFION surface but at elevated RH ice like water was detected even at fluorocarbon sites.¹⁶

Moilanen, et al. employed ultrafast spectroscopy by studying the vibrational lifetime of the OD stretch of dilute HOD in H₂O, characterized the changes of the hydrogen bond network as a function of hydration or increased water content in NAFION films. They concluded that water occupies two distinctly different environments within the polymer; one in the solvation shell of the sulfonate group characterized by slow OD stretch relaxation, and another with fast relaxation associated with bulk water.^{2,17}

Smotkin, et al. has used ATR and PM-IRRAS to study the long term durability of ion exchange membranes used in fuel cells. Smotkin's research is particularly interesting as for the first time the ionomer binder in the catalyst layer was studied in operando using PM-IRRAS. The resulting spectra were interpreted on the basis of DFT calculations and observations from ATR measurements on bulk membranes leading to surprising conclusions about the adsorption of NAFION on metal surfaces.¹⁸

While there are many parallels in the properties of interest for fuel cell ionomers and water treatment membranes (e.g. water transport and degradation) there are very few vibrational studies on RO membranes analogous to those on fuel cell ionomers. The primary reason for this dearth in vibrational studies on RO membranes is the multilayer construction of TFC membranes. The recent development of layer by layer RO membranes promises to open vibrational spectroscopy as a viable option to study water transport, chemistry and structure in these membranes and will be addressed later in this chapter.

2.2.3. Signal enhanced FTIR methods

FTIR and Raman scattering are two complementary vibrational spectroscopic methods that are often used for surface film and interfacial analysis.¹⁹ In general, Raman spectroscopy is best at probing symmetric vibrations of non-polar groups while IR spectroscopy is best at obtaining high signal from the asymmetric vibrations of polar groups. However, sensitivity in thin films is a big challenge, due to the fact that the number of molecules under study is typically very small. This problem was first overcome in Raman spectroscopy in the 1960s by the discovery of the surface enhanced Raman scattering (SERS) effect, and subsequently by the discovery of the surface enhanced infrared absorption effect (SEIRA) for infrared spectroscopy. Much of what we know about SEIRA comes from research about the SERS effect. Common features shared by SERS and SEIRA techniques are that rough or nano-structure substrates are necessary and the signal intensity can be related to surface orientation of molecules due to surface selection rules. These common features result from the similarity in the mechanisms that contribute to SERS and SEIRA enhancement effects.

This research has led to the more widespread use of SEIRA in so-called Kretschmann and Otto ATR geometries, Figure 2-1.

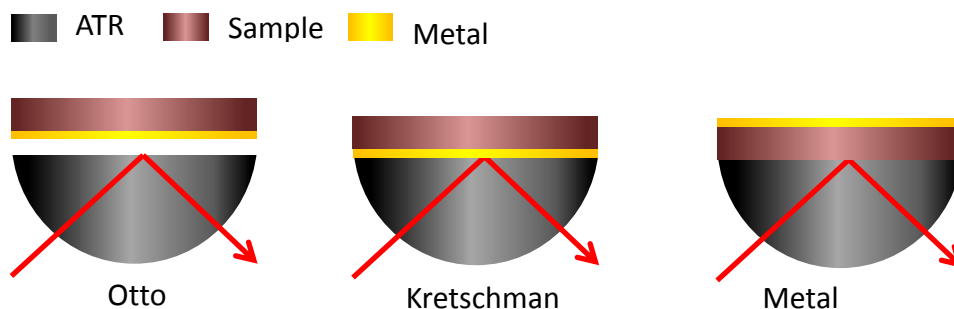


Figure 2-1. Schematic of three geometries used in SEIRA experiments.

In all these methods, the signal is enhanced up to 10 times by the presence of a metal layer.¹⁹ The improved signal in all these techniques results from electromagnetic field enhancements. SEIRA enhancement effects have the following characteristics;²⁰ SEIRA activity strongly depends on the morphology of the metal and the surface roughness.^{7,21} Band intensities depend on the polarization and angle of incidence,^{7,22} and the enhancement is significant for the first monolayer directly attached to the surface decaying sharply as distance from the surface increases and modes that have surface normal dipole moment components are preferentially enhanced giving rise to a surface selection rule.^{23,24} It is generally accepted that SEIRA enhancement arises from a long range electromagnetic (EM), effect and short range chemical effects. The enhancement can be described in terms four contributing effects, the resonance particle plasmon effect, the lightning rod effect, the image dipole effect and the chemical effect.^{19,23} These effects are discussed in turn below.

2.2.3.1 Resonance plasmon and lightning rod effects

Suzuki, et al. demonstrated that there is a direct relationship between absorbance and the electromagnetic field which resulted from collective electron resonance of metal island films and surface plasmon polaritons of continuous films.²⁵ These effects are now known as resonance plasmon effects in which coupling of the incident radiation field with local surface plasmons (LSP) of the roughened metal surface results in an amplification of the EM field. Atomic force microscopy experiments confirm that this roughened metallic film can be modelled as ellipsoidal metal islands on a substrate as shown in Figure 2-2. If the metal particle is smaller than the wavelength of light incident upon it, the particle will become polarized as a result of localized plasmon excitation. The dipole induced at the center of the island (P) film can be represented as:

$$P = \alpha VE \quad (1)$$

where α is the polarizability of the metal island, V is the volume of the metal island and E the amplitude of the incident electric field. This dipole generates an EM field around the island which is greater than the incident light alone and excites adsorbed molecules. The enhanced electric field is estimated to be 10 times greater than that of the incident light. The enhancement is short ranged due to the intensity of the local electric field decaying rapidly as the distance from the surface increases. The relation of field strength with distance from the metal island has been expressed as:

$$|E_{local}|^2 = \frac{4P^2}{l^6} \quad (2)$$

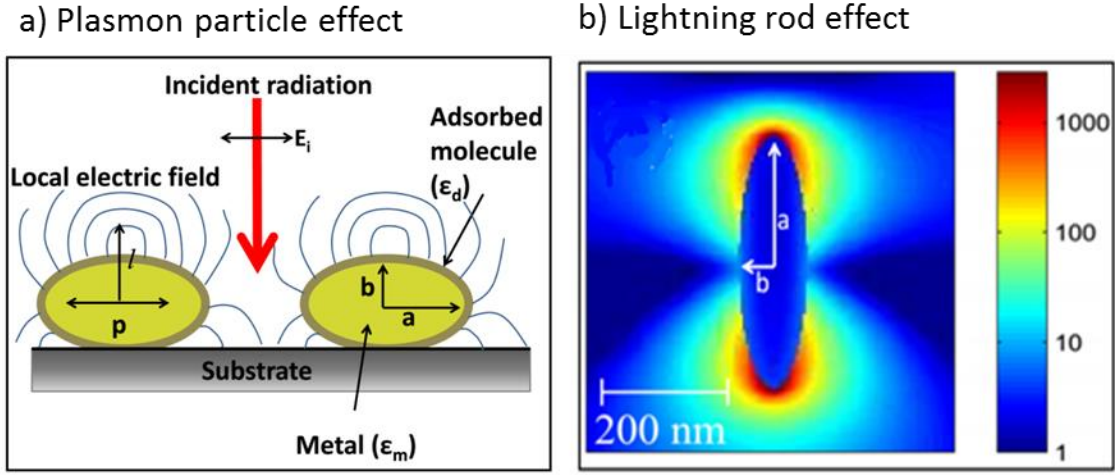


Figure 2-2. Model interaction of incident radiation with metal island substrate with dielectric constant ϵ_m coated with adsorbate molecules with dielectric constant ϵ_d and b) the resultant lightning rod effect on an ellipsoidal particle. The electric field intensifies along major axis resulting in electric field hot spots between metal islands.

where l is the distance from the center of the island. This explains the requirement for surface roughness and the spatial resolution of the enhancement, but does not explain the apparent dependence of the enhancement on the metal surface morphology. The influence of morphology on the enhancement can best be explained in terms of the lightning rod or antennae effect.

While E_{local} is symmetrically distributed on spherical surfaces, it is concentrated at the tip ends of prolate ellipsoids. The tip enhancement leads to increasing field enhancement colloids or islands with high aspect ratio (η). η is defined as a/b as shown in Figure 2-2. There is no relation to the incident wavelength and is not necessarily related to LSP generation because it is a morphology effect and not a resonance effect. Generally as η increases infrared absorbance also increase, and this is related to the field intensity at the tip, E_{tip} as follows:²⁶

$$E_{\text{tip}} = E_l + \frac{(1-A_a)(\epsilon_m-1)}{1+(\epsilon_m-1)A_a} \quad (3)$$

where E_l is the applied electric field along the major axis of the ellipsoid, ϵ_m is the dielectric constant of the metal island and A_a is the depolarization factor which is inversely proportional to η . It is reasonable to believe that plasmon resonance effects and lightning rod effects are coupled thereby amplifying the plasmon resonance effect. However, the relationship between these effects is still not fully understood. Experimental evidence suggests that resonance plasmon effects dominate for SERS which explains why only coinage metals are SERS active substrates. For SEIRAS, even non SERS active substrates provide significant enhancements and the roughness and texture of the surface is more important which suggest the lightning rod effect dominates.

2.2.3.2 Image dipole and chemical effects

The image dipole effect is perhaps the best known enhancement mechanism due to the surface selection rule first described by Greenler in 1960.²⁴ Greenler's surface selection rule simply put is that only surface normal dipoles are visible in reflection IR experiments.

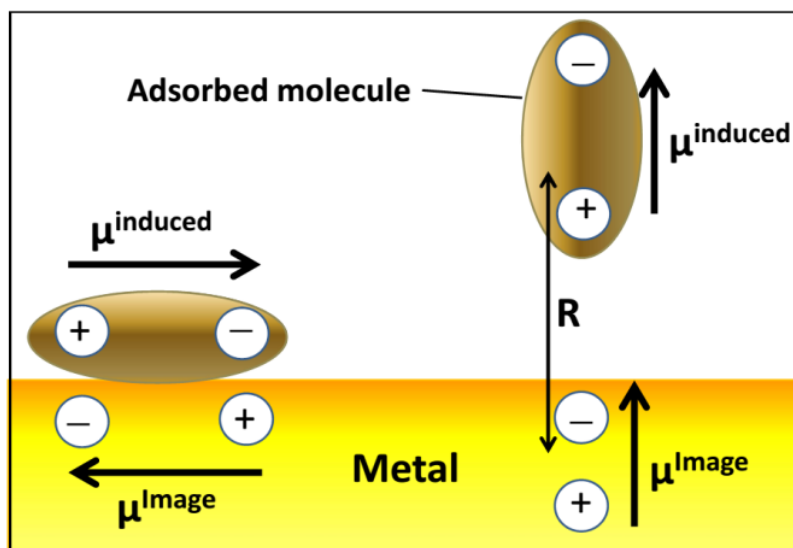


Figure 2-3. Image dipole effect, the surface parallel induced dipole is annihilated by the image dipole in the metal while the surface normal induced dipole is enhanced.

In the description of the image dipole effect the electrode is envisaged as a mirror and the molecule is taken as a point dipole. The electric field of the EM wave E induces an oscillating dipole in the adsorbate $\mu^{induced}$ which in turn induces an image dipole in the metal μ^{image} which has an electric field E_{image} associated with it. E_{image} is given by:

$$E_{image} = \gamma \frac{2\mu^{induced}}{R^3} \quad (4)$$

where γ is a constant dependent on the dielectric constants of the metal and adsorbate and R is the distance of the dipole from its image.²⁷

E_{image} adds constructively with E and enhances the overall field experienced by the molecule. This makes $\mu^{induced}$ larger as described in equation (5) leading to increased IR absorbance.

$$\mu^{induced} = \alpha(E + E_{image}) \quad (5)$$

Figure 2-3 shows this additive effect of μ^{image} on surface normal dipoles and how μ^{image} has the effect of cancelling out surface parallel dipoles. From this description it is clear that the image dipole effect is only important when dipoles are oriented surface normal, and this orientation of dipoles typically arises from chemical effects.

Generally, the chemical contribution to the SEIRA effect is much less than the EM contribution. One of the chemical origins of SEIRA is the orientation of molecules on a metal surface. Chemisorption on metal surfaces results in ordering of molecules on the surface. Molecules with ordered orientation give larger intensities than randomly ordered molecules for vibrations that give dipole changes normal to the surface due to the dipole being in line with the local electric field.

2.2.3.5 Electric field enhancements on non-metallic substrates

Due to its high refractive index and high surface reflectance, silicon substrates may seem amenable to grazing angle reflection spectroscopy. However, a grazing incident angle above 70° is near its Brewster's angle (73.7°) for silicon. As a result, the reflectance from silicon for p-polarized light at grazing angle is low. Additionally, the peak interpretation of thin films at grazing angle on silicon substrates can be complicated due to band distortions and peak shifts that are not yet fully understood. At grazing angles however, under conditions where the ATR crystal has a high refractive index, it is possible to obtain high quality spectra for thin films on silicon. This grazing angle ATR (GAATR) geometry only gives signal enhancement when a suitable substrate acts as an overlayer for the sample being analyzed and so we have termed it substrate over ATR (SO-ATR). The enhancement is believed to originate from the constructive interference of the evanescent wave within the sample film and is characterized a strong dependence on the thickness of the sample layer. The enhancement results in atypical unpolarized FTIR spectra where unexpected peak appearance cannot be simply explained as Reststrahlen bands²⁸ or spectral distortions.^{29,30}

Although the development of ATR dates back to the beginning of the widespread use of FTIR, GAATR has remained relatively unknown until the early 1990's when Milosevic and Berets began to explore the 100 fold enhancement in spectral intensity sometimes observed in this geometry. Only in the last 20 years have research articles been published utilizing GAATR somewhat regularly. We have also studied the enhancements observed in this geometry as a path to understanding the orientation of NAFION thin films on NAFION. A detailed description of the origin enhancement and its implications on spectral interpretation are presented in Chapter 3.

2.3 Current State Fuel Cell Ion Exchange Membrane Research

2.3.1 Proton exchange membranes

NAFION is a trademark perfluorinated sulfonic acid (PFSA) of Dupont and finds applications in electrochemical devices. The chemical structure of NAFION consists of a hydrophobic backbone with perfluorinated ether sidechains terminated by sulfonic acid groups as shown in Figure 2-4. The combination of an extremely hydrophobic Teflon-like backbone which provides structural integrity, with the very hydrophilic sulfonic acid, results in well-defined nanochannels within NAFION membranes when hydrated, Figure 2-4b.

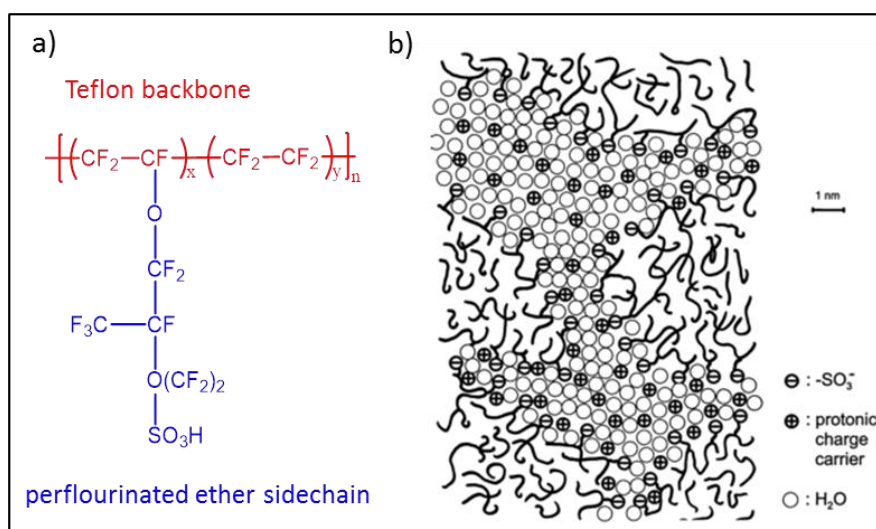


Figure 2-4. a) Repeat unit of NAFION and b) schematic representation of the phase separated morphology of NAFION with well-defined nano-channels.⁸⁹

The sulfonic acid groups provide protonic charge carriers via dissociation, and proton conductance is assisted by water dynamics through the percolating water-filled cavities. In a PEFC catalyst layer, NAFION acts as a binder in the anode and cathode layers where it forms a film 2-20 nm thick on the aggregates of Pt nanoparticles, Figure 2-5.³¹ At low pH, the performance is limited

by the cathode oxygen reduction reaction (ORR) which is at least six orders of magnitude slower than the anode hydrogen

oxidation reaction (HOR). Kocha, et al. demonstrated that the presence of NAFION as a binder on Pt/C cathode electrodes reduces the ORR catalytic activity 1.8 times.³²

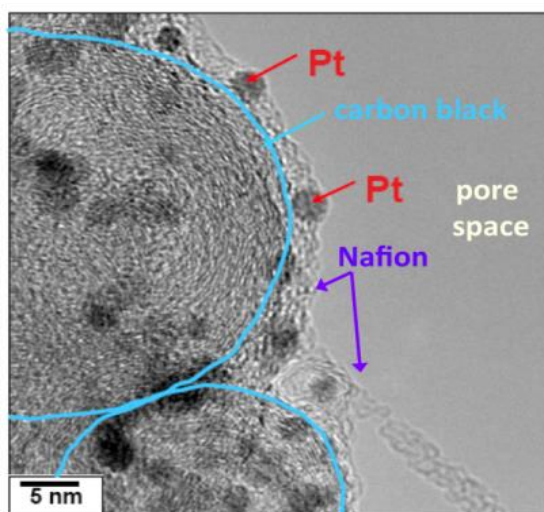


Figure 2-5. Catalyst layer carbon supported Pt nanoparticle coated with NAFION. ³¹

Jomori, et al., after conducting cyclic voltammetry experiments, proposed that the ionomer may adsorb on the surface and decrease the available catalytic surface area available or alternatively, conformational changes in the polymer layer may block incoming oxygen molecules thereby decreasing catalytic activity.³³

The nano-morphology of NAFION bulk membranes has been studied thoroughly using small-angle X-Ray scattering and a phase separated structure reported. However, the character of NAFION in the catalyst layer is still poorly understood with several models being proposed and periodically revised.^{34,35} The effect of confinement and substrate identity on water uptake proton conductivity and structure have been studied using X-ray specular reflection (XRR)³⁶ grazing incidence small x-ray scattering (GI-SAXS)^{9,37-39} and neutron reflectometry (NR).⁴⁰⁻⁴²

The difficulty in directly probing the ionomer structure and properties in the 5–20 μm thin catalyst layer with a porous composite structure resulted in studies of thin ionomer films on well-defined planar substrates such as SiO_2 or Au/Pt coated silicon wafers. These studies have suggested that the morphology of an ionomer on an electrode plays a significant role in the catalytic processes taking place in the MEA and thus influences the overall fuel cell efficiency. There is strong evidence that the morphology of NAFION is tied to its thickness and distinct changes in properties such as water uptake and conductivity.⁴³ In fluorescence experiments, Dishari and Hickner demonstrated that NAFION thin films at the SiO_2 interface had higher water uptake than thicker films⁴³ which is consistent with the quartz-crystal microbalance (QCM), ellipsometry, and grazing-incidence X-ray scattering observations of Kosoglu, et al. on films 4-300 nm thick.⁹

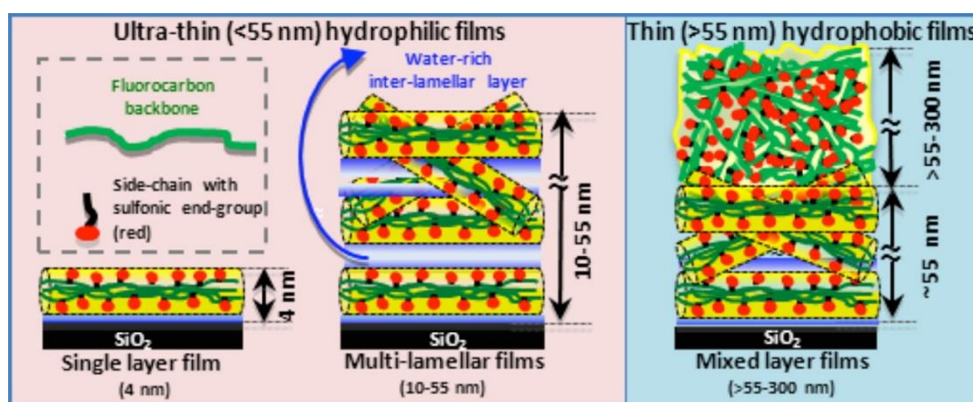


Figure 2-6. Proposed morphologies of NAFION thin films on silicon substrates at different thickness regimes ranging from highly oriented single layers below 4 nm to mixed morphology films above 55 nm.⁴⁵

The water uptake trends appear to be substrate dependent as Konganand, et al. in QCM observed a decrease in water uptake as film thickness decreased for films prepared on gold.⁴⁴ Eastman, et al. found that the swelling ratio, volumetric water fraction, and effective diffusivity of films are relatively constant for spin-coated films thicker than approximately 60 nm but gradually decreased with decreasing thickness.³⁶ Paul, et al. prepared a series of NAFION samples on SiO_2

substrates ranging from 4 nm to 300 nm and used surface wettability tests and AFM as a function of thickness to probe morphology changes.⁴⁵ They proposed the existence of three distinct morphologies depending on thickness regime; a single layer morphology at 4 nm and below, a multilamellar morphology between 10 – 55 nm, and a mixed morphology for thicknesses greater than 55 nm, Figure 2-6. This morphology change at 55 nm would explain observation that the proton conductivity of sub-55 nm NAFION thin films was found to be independent of thickness whereas that of the thicker films was thickness-dependent, approaching that of the membrane.⁴⁶ In a similar more recent study, Paul, et al. investigated thermally induced changes in surface wettability and proton conductivity of 4 nm-300 nm films on SiO₂ substrates. It was found that proton conductivity decreases significantly upon annealing with a stronger thickness dependence on conductivity for annealed films.⁴⁷

2.3.2 FTIR analysis of NAFION thin films

FTIR has routinely been used to study NAFION membranes in the micron thickness range to probe its water transport properties in its role as a separator membrane in fuel cells.^{2,48-50} The majority of these studies have been centered on the transport of water through bulk films. Extending this work to encompass thin films is complicated by changes in the appearance of the NAFION spectrum when the sampling geometry is changed, and the ambiguity in some of the peak assignments relevant to interpreting the spectra, Figure 2-7.

Kunimatsu, et al. conducted an ATR study of water in several micron thick NAFION NRE211 membrane combined with proton conductivity measurements during hydration/dehydration cycle.⁵¹ In this study, the authors suggested that there are two kinds of water in a NRE211 membrane with distinct $\delta(\text{HOH})$ frequencies; one at 1740 cm⁻¹ and the other at 1630

cm⁻¹.

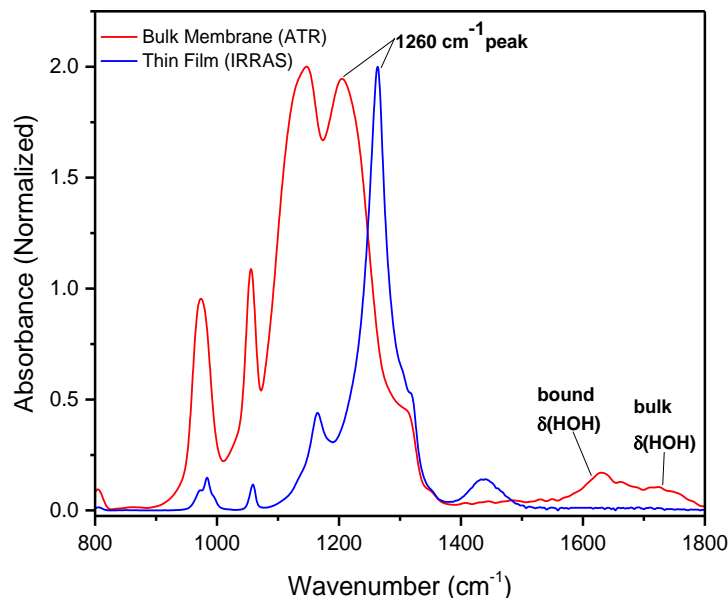


Figure 2-7. ATR spectrum of bulk NAFION membrane similar to that used in MEA hydration studies overlaid with the corresponding NAFION thin film spectrum on a gold substrate. The water peaks and 1260 cm⁻¹ peak discussed in the text are labelled.

The initial hydration of the dry membrane results in the dissociation of the SO₃H group with the resultant proton being hydrated to yield the $\delta(\text{HOH})$ band at 1740 cm⁻¹. As hydration continued, water associated with SO₃⁻ ions represented by the $\delta(\text{HOH})$ band at 1630 cm⁻¹ increased as does the associated proton conductivity. In Kunimatsu, et al.'s work as with the majority of NAFION articles published, the focus is on proton conductivity and hydration in an MEA and the only water peaks and the SO₃⁻ symmetric stretch is considered.⁵²⁻⁵⁴

While OH peaks can inform us about water transport and in part explain the differences between bulk and thin film physical properties, much more detailed information can be obtained from the fingerprint region of the polymer. Numerous experimental and theoretical research articles have been published attempting to explain the NAFION fingerprint region.^{49,52,55,56} Unfortunately,

absolute clarity about the exact contribution of individual vibrational modes to the overall spectrum has eluded researchers. The best illustration of this ambiguity is the 1260 cm^{-1} peak. In PM-IRRAS experiments, Davis, et al. assigned the 1260 cm^{-1} peak to $\nu(\text{CF}_2)$ ⁵⁷, while also in PM-IRRAS Kendrick, et al. assigned the same peak to the $\nu(\text{CF}_3) + \delta(\text{COC})$ vibration mode.¹⁸ Korzeniowski from transmission experiments⁴⁹ and Malevich from deconvoluted in situ IRRAS data, assigned the same 1260 cm^{-1} peak to SO_3^- .⁵⁸ Zeng, et al. in surface enhanced Raman experiments assigned this 1260 cm^{-1} peak to $\nu(\text{CF}_3)$ ⁵⁹ while Ono, et al. assigned it to $\nu(\text{CF}_2)$ and SO_3^- groups.⁶⁰

Until recently, however, very little research on thin films of NAFION has been published in the literature. Davis, et al. have used in situ, time resolved PM-IRRAS in an attempt to elucidate water transport mechanisms in 153 nm NAFION films.⁵⁷ Notably this study revealed that the effective diffusion coefficient of water in NAFION thin films is between 4 and 5 orders of magnitude lower than in bulk NAFION. As with the ATR work on bulk membranes, Davis, et al. focused on OD and OH peaks in the spectrum of NAFION exposed to humidified air and provided information that can be thought of as complimentary to bulk film studies.

Recently Ono and Nagao used p-polarized multiple-angle incidence resolution spectrometry (p-MAIRS) technique was used to investigate the in-plane (IP) and out-of-plane (OP) NAFION spectra on silicon and thin Pt surfaces.^{60,61} MAIRS is a relatively new technique developed by Hasegawa to evaluate molecular orientation of films based on band shifts that result from the splitting of transverse optical and longitudinal optical modes.⁶² Based on the increase of the intensity of the 1260 cm^{-1} OP peak that Ono and Nagao assigned to a mixture of CF_2 and SO_3^- , they concluded that the degree of orientation on the Pt-deposited surface depends on the thickness. This conclusion is consistent with the observations of Kendrick, et al. based on in operando PM-IRRAS of catalyst layer NAFION coated Pt which showed strong ordering of NAFION thin films on Pt.¹⁸ Based on the assignment of the 1260 cm^{-1} peak to mechanically coupled modes dominated by the CF_3 asymmetric stretch, Kendrick, et al. concluded that NAFION adsorbs on Pt surfaces via

both the SO_3 and CF_3 . While these two studies provide strong evidence for ordering of NAFION thin films they also exemplify the conflict of opinion with regards to the orientation of NAFION on the electrode surface.

2.3.3 Perspective on ion exchange membrane research beyond NAFION

One promising alternative to NAFION based fuel cells are fuel cells based on sulfonated block copolymers because the combination of ionic and nonionic blocks provides the potential for highly ordered morphologies where transport properties can be tailored in a reliable fashion.⁶³ One notable example of this research is the work of Bae, et al. who synthesized a series of sulfonated poly(arylene ether sulfone)s (SPEs) block copolymers and measured the proton conductivity as a function of hydration at elevated temperatures.⁶⁴ Bae, et al. demonstrated that at high hydration where acidity difference is less important, block copolymers display higher conductivity than NAFION. Block copolymer micro domain size, and orientation have been shown to significantly improve proton conductivity compared to random copolymer analogs but are yet to outperform NAFION at low humidity.⁶³

Yeh, et al. used periodic density functional theory (DFT) methods to study the adsorption of sulfate and bisulfate molecules on Pt (111) surfaces as a model process for interfacial chemistry related to NAFION sulfonic group adsorption on Pt electrocatalysts.⁶⁵ Yeh, et al. determined that there is a linear correlation between the sulfonate proton affinity and the equilibrium potential of the sulfonate anion. This insight shows that the charge density on the sulfonate group influences its adsorption, which may be related to how different polymers perform in fuel cell electrodes.

Another approach to improving NAFION-based fuel cells is the use of anion exchange membrane (AEM) based fuel cells. The Hickner group has done extensive work studying the synthesis, performance and stability of novel AEM materials. AEM fuel cells promise to solve one

critical shortfall of PEM fuel cells; the need for expensive catalysts. The oxygen reduction reaction is more facile in alkaline conditions where AEMFCs operate compared to the acidic environment where PEMFCs operate and more possibilities exist for cathode catalysts thus eliminating the need for noble metal catalysts to achieve similar performance to PEMFCs. One major drawback of AEMs however is degradation of cationic groups at low hydration due to nucleophilic attack. Poly(phenylene oxide) (PPO)-based AEMS with quaternary ammonium ionic groups provide the best stability and performance to date. The performance however is yet to exceed that of NAFION at low hydration without suffering excessive alkaline degradation. The precise degradation mechanism for these membranes remains unknown and hence research is ongoing to understand the degradation mechanisms and improve stability.

Pan, et al. designed a series of semi-interpenetrating network AEMs which contained both a rigid and a flexible component.⁶⁶ These membranes displayed improved mechanical strength and flexibility over conventional QAPPO membranes in addition to high conductivities and improved chemical stability. Zhu, et al. have reported that a polymer motif with multiple cations per side chain site can boost both the conductivity and stability of poly(2,6-dimethyl-1,4-phenylene oxide)-based AEMs.⁶⁷ Other strategies such as moving the cationic group further from the backbone⁶⁸ and reducing backbone functionalization⁶⁹ have been suggested but a breakthrough in improving stability after prolonged exposure to alkaline conditions is yet to be realized.

2.4 Probing Microstructure in Reverse Osmosis Membranes

2.4.1 Current state of polyamide RO membrane research

Thin film composite (TFC) reverse osmosis membranes with aromatic polyamide active layers dominate the RO market due to the reasonable tolerance to impurities, enhanced durability

and easy cleaning characteristics of these membranes. The TFC design also allows the distinct layers to be finely tuned to achieve various mechanical, transport and filtration properties. The typical synthesis of the active layer is via interfacial polymerization where highly porous polysulfone is coated with m-phenylenediamine (MPD) and then reacted with trimesoyl chloride (TMC).^{70–72} The two monomers can react forming linear chains.

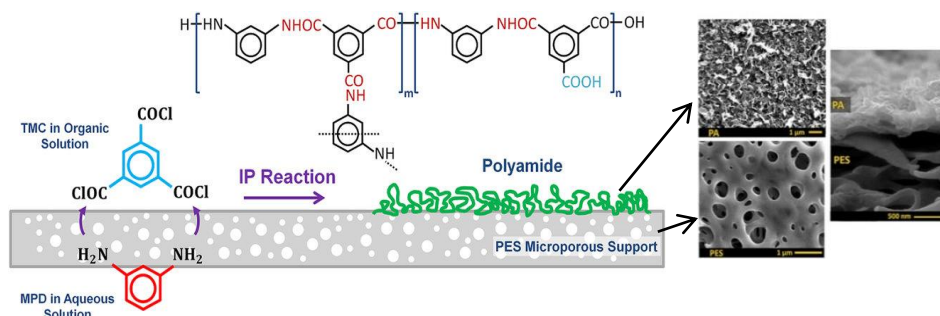


Figure 2-8. Schematic for typical interfacial polymerization synthesis of aromatic polyamide (PA) on polysulfone (PES) support to form dense PA film.⁷²

The two remaining unreacted acyl chlorides of the TMC monomer can either undergo hydrolysis and form carboxylic acid or can react with additional MPD monomers and form a highly cross-linked structure, Figure 2-8. Manufacturers of these films aim to control surface roughness, thickness, crosslink density, monomer ratio and unreacted end group concentration. The biggest challenge in studying these parameters is that they are often intricately interconnected making it difficult to delineate their individual contributions to transport.

Although interfacial polymerization is very efficient, the fast polymerization and reaction conditions produce rough films with significant chemical heterogeneity. Freger analyzed the structural changes during interfacial polymerization and demonstrated that there exists a direct correlation between the thickness of the film and surface roughness.⁷³ In the same study, Freger demonstrated the process of interfacial polymerization proceeds in three distinct kinetic phases

which have implications on the structure of the resultant film. The conclusions drawn by Freger implies that being able to control the kinetics of film growth can lead to controlling film structure.

Using XPS and Rutherford backscattering spectrometry (RBS) Coronell, et al. probed the surface and volume average properties of commercial RO membranes and observed heterogeneity in the concentration and pKa distribution of carboxylic groups as well as the degree of polymer cross-linking.¹³ By using RBS, Coronell, et al. were able quantify the ratio of carboxylic acid groups (R-COOH) to ionized groups (R-COO⁻) by neutralizing the charged species with Ag⁺ ions and analyzing the resulting RBS spectra for the Ag⁺. XPS⁷⁴ and streaming potential⁷⁵ measurements indicated that polyamide TFC membranes possess a significant negative charge which originates from up to 11% of the acyl groups on TMC not being converted to amide.⁷⁶ This observation is in contrast to ATR data that indicates that the concentration of unreacted acyl groups is negligible. Based on TEM images and theoretical models, Freger has suggested that the PA layer in RO and NF membranes prepared by interfacial polymerization possess a double layer structure in which the outermost layer is negatively charged and is separated from the porous support by a dense positively charged layer.⁷⁶

Positron annihilation lifetime spectroscopy (PALS) has been applied by Kim, et al. to explain the water flux in TFC membranes.⁷⁷ Kim, et al. were the first to experimentally demonstrate that the PA membranes are composed of network pores of radius 2.1-2.4 Å and aggregate pores of

radius 3.5-4.4 Å, Figure 2-9.⁷⁷ Kim, et al. concluded that for interfacially polymerized films as the degree of cross-linking increases the number of network pores increases resulting in an increase of water flux. The mechanism of water transport in these proposed pores however, remains unexplored.

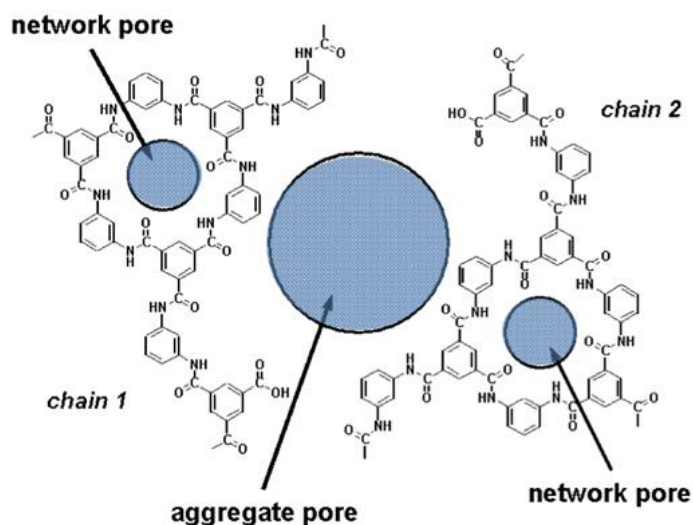


Figure 2-9. Network and aggregate pores proposed by Kim et al. Network pores are formed within highly crosslinked chains while aggregate pores are formed between loosely crosslinked chains.⁷⁷

Puffr and Sebenda studied the mechanism of water transport in amorphous aliphatic polyamide (Nylon) membranes. In this study, the infrared absorbance of these membranes as a function of relative humidity was recorded and the authors of this work concluded that water binds to the amide groups, first forming a double hydrogen bond between carbonyl group (termed firmly bound water) and then forming bridging hydrogen bonds between amide C=O and N-H groups (termed loosely bound water).⁷⁸ Based on a similar study on Nylon 6-6 by Lim, et al., three sites for water binding were identified; a strongly bound water site, a loosely bound water site, and a site for capillary condensed water which is only indirectly related to the C=O and N-H groups.⁷⁹ While the aforementioned work on aliphatic polyamide systems may provide the basis for understanding transport in aromatic systems, not enough work has been done on the aromatic polyamide systems to draw any meaningful conclusions.

Leckie, et al. has published a series of papers that comprehensively characterized the physiochemical properties of commercial RO and NF membranes using XPS, TEM, ATR and streaming potential measurements.⁸⁰⁻⁸² while the work of the Leckie group provided useful insights

about membrane chemistry and structure, the fabrication of many commercial membranes involves proprietary steps such as the application of a surface coating which strongly affects membrane properties.

While peaks were assigned by Tang and Leckie to the ATR spectrum of aromatic PA membranes, these assignments were limited to the Amide I and II regions and were heavily convoluted with bands from the underlying polysulfone layer or surface coating. Even when delaminated uncoated films are analyzed there has to date been no complete peak assignment of the aromatic polyamide fingerprint region resulting in some ambiguity and misinterpretation of spectral changes. Kang, et al. in a study of the chlorine degradation assigned the peak at 1610 cm^{-1} to hydrogen C=O of the amide group.⁸³ Based on the disappearance of this peak, they concluded that the hydrogen bonds between C=O and N-H were completely destroyed during chlorine attack which proceeded by chlorine replacing the hydrogen in N-H groups to form N-Cl.⁸³ In a similar chlorine degradation study, Anthony, et al. assigned the 1610 cm^{-1} peak to aromatic ring C=C vibrations.⁸⁴ Based on the disappearance of this peak they concluded that chlorine attack was via ring insertion in the ortho or para position.⁸⁴

Jin and Su used ATR to study the effects of polymerization conditions on hydrophilic groups in aromatic polyamide thin films using the 1720 cm^{-1} shoulder assigned to unreacted carboxylic groups.⁸⁵ This band overlaps with the Amide I band which is predominantly the amide C=O and is sensitive to hydrogen bonding. It is possible that a systematic study of this spectral region along with the amide II region can provide insights about the state of water in polyamide films but as yet no papers have been published primarily due the difficulty in accurately deconvoluting overlapping bands.

Characterization of the polyamide layer in TFC membranes is greatly complicated by contributions from the underlying layers. One approach to solve this problem is to analyze delaminated films where the non-woven fabric is physically removed and the polysulfone support

dissolved in a suitable solvent to leave the isolated polyamide layer. It can be argued that the process of isolating the polyamide layer alters the physical properties of the film making correlations to properties in the TFC membrane difficult. Another approach is to fabricate the membrane on a substrate suitable for the characterization technique to be used, which has led to the development of molecular layer by layer membranes⁸⁶

2.4.2 molecular Layer by Layer synthesized polyamide RO membranes

Johnson, et al. developed a molecular layer by layer (mLbL) deposition process to synthesize crosslinked polyamide films on planar nonporous substrates.⁸⁶

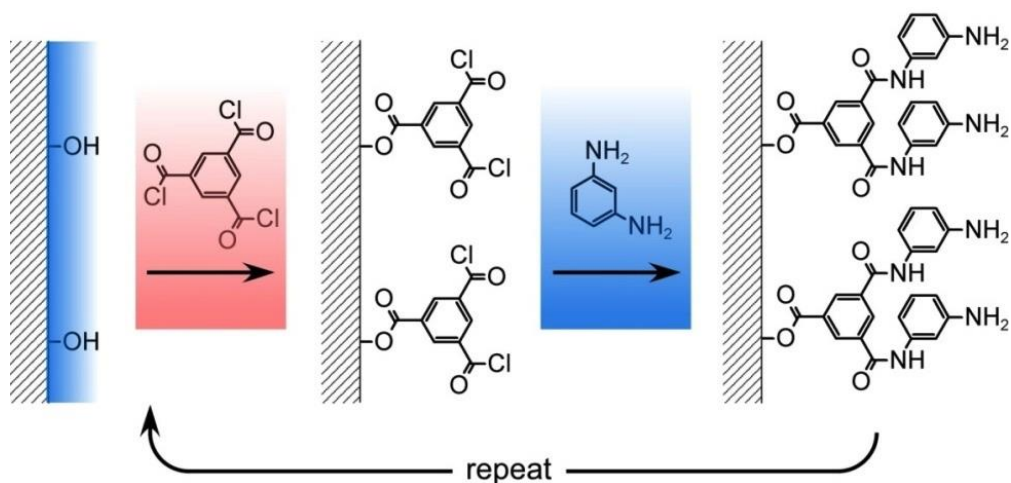


Figure 2-10. Schematic representation of the mLbL synthesis process on silicon substrates, using TMC and MPD as the monomers.⁸⁶

In this process TMC is dissolved in toluene and spin cast on a silicon substrate. Excess monomer is washed of using acetone before the subsequent spin casting of a solution of MPD in toluene to complete one polymerization cycle, Figure 2-10. Typically the terms cycle and layer are used interchangeably to refer to one complete reaction of TMC with MPD monomers. Johnson, et al. demonstrated that this process produces conformal coatings at linear growth rate of ~ 0.9 nm per

cycle. The surface chemistry of the surface can be controlled based on which reaction step was performed last, leading to amine or carboxylic acid rich surfaces. The reaction between the MPD and TMC is so fast that it is difficult to control the diffusion of the monomers, and thus interfacial polymerization fabricated PA layer are characterized by high depth heterogeneity and rough ridge-and-valley structures. Consistent with the implications of Freger's conclusions,⁷³ the ability to control film growth in mLbL films results in films 70 times smoother than interfacial polymerized films. Figure 2-11.

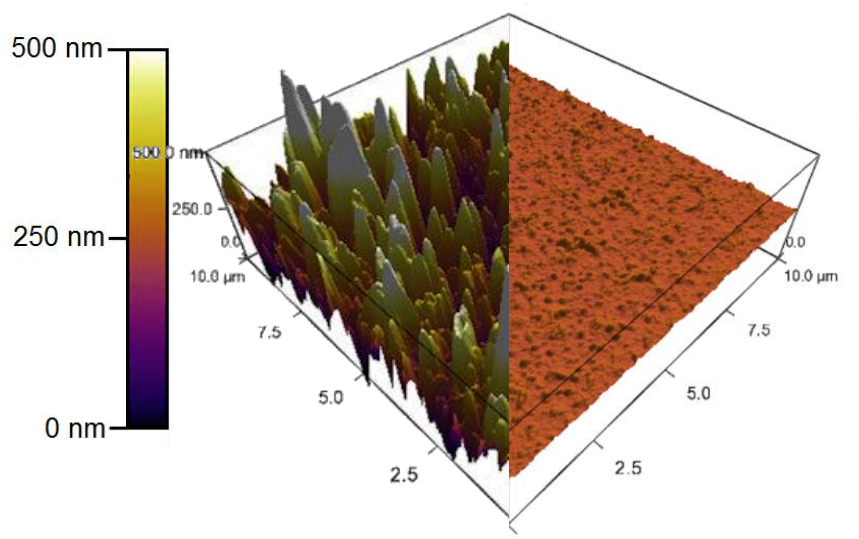


Figure 2-11. Comparison of AFM height images of 30 cycle mLbL polyamide (Right) and commercial polyamide (Left) plotted using the same height scale.⁸⁶

Chan, et al. studied the swelling of mLbL films using X-ray reflectivity and showed that the swelling behavior of these ultrathin films is consistent with 1-dimensional swelling, with the maximum swelling ratio highly sensitive to the specific diamine chemistry.¹¹ Chan, et al. were able to show that simply selecting ortho-phenylene diamine over meta-phenylene diamine reduces the swelling ratio and the crosslink density.

Wei, et al. demonstrated that in interfacial polymerized films the ratio of TMC to MPD has a significant influence on membrane performance as TFC membranes prepared with higher MPD

concentrations or lower TMC concentrations had lower water permeability but better salt rejection.⁸⁷ Layer by layer assembled film have been shown to have improved biofouling resistance which is as a result of the improved surface roughness. Ishigami, et al. used QCM to study foulant adsorption on LbL assembled films and found that BSA adsorbed only weakly on 6 layer films due to the increased smoothness of the film.⁸⁸

Gu, et al. demonstrated that in composite membranes fabricated via mLbL, the water flux gradually decreases and the salt rejection gradually increases with increasing cycle number. At a cycle number of 10, the mLbL membrane exhibited a salt rejection similar to interfacially polymerized membranes and a water flux approximately 82% higher than the interfacially polymerized analog.

Solvent based mLbL synthesis of RO membranes is relatively new and very little work has been published characterizing these films. The improved homogeneity and control of membrane chemistry combined with the absence of a porous support makes mLbL PA membranes an ideal model to study structure property relationships in aromatic polyamide RO membranes. It is apparent that mLbL films display superior water flux, salt rejection and antifouling properties and there is keen interest in transferring these properties to commercial TFC membranes. We have conducted the first FTIR study of mLbL films in order to explain the growth of the initial layers, the orientation and chemical differences as a function of layer number which will be presented in subsequent chapters.

2.5 Conclusion

There are parallels in the questions researchers seek to answer in studying both fuel cell ionomers and RO membranes, namely, "how is water transported through these films?", and "what is their orientation on different substrates and how do variations in orientation and chemistry affect

the transport of water through these films?” While we have made great strides in answering these questions for bulk membranes, little of this knowledge can be transferred to thin films due to confinement effects and the influence of underlying layers. Numerous characterization techniques exist to probe the transport, structure and chemistry of these materials, key among them being X-ray techniques, neutron scattering and optical spectroscopy. Among these methods, vibrational spectroscopy and FTIR, in particular, has been demonstrated to be a powerful tool that can answer most of the outstanding research questions either as a stand-alone technique or in conjunction with other methods. For FTIR to be successfully applied in thin film research, there is a need for the signal to be enhanced and for the mechanism of the enhancement to be fully understood in order to rationalize changes in spectral features associated with the enhancement.

The literature surveyed in this chapter represents a fraction of what is published, but demonstrates that a wealth of knowledge exists pertaining to signal enhancement on metal substrate but currently much less is known about signal enhanced FTIR on silicon substrates. Being able to collect high quality thin film spectra on silicon would allow easier comparison with the findings of alternative methods such as TEM as well as a better understanding of existing bulk film FTIR data.

In the ensuing chapters, the mechanism of FTIR signal enhancement on silicon substrates shall be presented demonstrating how this enhancement can be used in SO-ATR geometry to probe the orientation of thin films. The fingerprint region of aromatic polyamide systems which has until now been poorly understood will be analyzed in detail and SO-ATR will be applied to these aromatic polyamide films and NAFION to understand the orientation of these film on planar non-porous substrates.

2.6 References

- (1) Fayer, M. D. Fayer group publications <https://web.stanford.edu/group/fayer/> (accessed Apr 24, 2016).
- (2) Moilanen, D. E.; Piletic, I. R.; Fayer, M. D. Tracking Water's Response to Structural Changes in NAFION Membranes. *J. Phys. Chem. A* **2006**, *110* (29), 9084–9088.
- (3) University of Yamanshi Fuel Cell Nanomaterials Center-Researcher profile <http://fc-nano.yamanashi.ac.jp/english/profile/00/MWatanabe.html> (accessed Apr 24, 2016).
- (4) Kanimatsu, K.; Yoda, T.; Tryk, D. A.; Uchida, H.; Watanabe, M. In Situ ATR-FTIR Study of Oxygen Reduction at the Pt/NAFION Interface. *Phys. Chem. Chem. Phys.* **2010**, *12* (3), 621–629.
- (5) Hokkaido University Catalysis Research Center <http://www.cat.hokudai.ac.jp/index.eng.html> (accessed Apr 24, 2016).
- (6) Ishino, Y.; Ishida, H. Grazing Angle Metal-Overlayer Infrared ATR Spectroscopy. *Appl. Spectrosc.* **1988**, *42* (7), 1296–1302.
- (7) Osawa, M. Dynamic Processes in Electrochemical Reactions Studied by Surface-Enhanced Infrared Absorption Spectroscopy (SEIRAS). *Bull. Chem. Soc. Jpn.* **1997**, *70* (12), 2861–2880.
- (8) Milosevic, M. Internal Reflection and ATR Spectroscopy. *Appl. Spectrosc. Rev.* **2004**, *39* (3), 365–384.
- (9) Kusoglu, A.; Kushner, D.; Paul, D. K.; Karan, K.; Hickner, M. A.; Weber, A. Z. Impact of Substrate and Processing on Confinement of NAFION Thin Films. *Adv. Funct. Mater.* **2014**, *24* (30), 4763–4774.
- (10) Modestino, M. A.; Kusoglu, A.; Hexemer, A.; Weber, A. Z.; Segalman, R. A. Controlling NAFION Structure and Properties via Wetting Interactions. *Macromolecules* **2012**, *45* (11), 4681–4688.
- (11) Chan, E. P.; Young, A. P.; Lee, J.-H.; Stafford, C. M. Swelling of Ultrathin Molecular Layer-by-Layer Polyamide Water Desalination Membranes. *J. Polym. Sci. Part B Polym. Phys.* **2013**, *51* (22), 1647–1655.
- (12) Mi, B.; Coronell, O.; Mariñas, B. J.; Watanabe, F.; Cahill, D. G.; Petrov, I. Physico-Chemical Characterization of NF/RO Membrane Active Layers by Rutherford Backscattering Spectrometry. *J. Memb. Sci.* **2006**, *282* (1–2), 71–81.
- (13) Coronell, O.; Mariñas, B. J.; Cahill, D. G. Depth Heterogeneity of Fully Aromatic Polyamide Active Layers in Reverse Osmosis and Nanofiltration Membranes. *Environ. Sci. Technol.* **2011**, *45* (10), 4513–4520.

- (14) Guicheney, M.; Watts, J. F.; Abel, M.-L.; Audenaert, M. Mechanism of Delamination of a Polyamide Coating Modified with an Aminosilane. *Surf. Interface Anal.* **2006**, *38* (4), 168–171.
- (15) Yagi, I.; Inokuma, K.; Kimijima, K.; Notsu, H. Molecular Structure of Buried Perfluorosulfonated Ionomer/Pt Interface Probed by Vibrational Sum Frequency Generation Spectroscopy. *J. Phys. Chem. C* **2014**, *118* (45), 26182–26190.
- (16) Noguchi, H.; Taneda, K.; Minowa, H.; Naohara, H.; Uosaki, K. Humidity-Dependent Structure of Surface Water on Perfluorosulfonated Ionomer Thin Film Studied by Sum Frequency Generation Spectroscopy. *J. Phys. Chem. C* **2010**, *114* (9), 3958–3961.
- (17) Moilanen, D. E.; Piletic, I. R.; Fayer, M. D. Water Dynamics in NAFION Fuel Cell Membranes: The Effects of Confinement and Structural Changes on the Hydrogen Bond Network. *J. Phys. Chem. C* **2007**, *111* (25), 8884–8891.
- (18) Kendrick, I.; Kumari, D.; Yakaboski, A.; Dimakis, N.; Smotkin, E. S. Elucidating the Ionomer-Electrified Metal Interface. *J. Am. Chem. Soc.* **2010**, *132* (49), 17611–17616.
- (19) Zimudzi, T. J. FTIR Studies of Thin Ionomer Films. *pennsylvania State Univ.* **2014**.
- (20) Sur, U. U. K.; Chowdhury, J. Surface-Enhanced Raman Scattering: Overview of a Versatile Technique Used in Electrochemistry and Nanoscience. *Curr. Sci.* **2013**, *105* (7), 923–939.
- (21) Miyake, H.; Ye, S.; Osawa, M. Electroless Deposition of Gold Thin Films on Silicon for Surface-Enhanced Infrared Spectroelectrochemistry. *Electrochem. commun.* **2002**, *4* (12), 973–977.
- (22) Le Ru, E. C.; Meyer, S. A.; Artur, C.; Etchegoin, P. G.; Grand, J.; Lang, P.; Maurel, F. Experimental Demonstration of Surface Selection Rules for SERS on Flat Metallic Surfaces. *Chem. Commun.* **2011**, *47* (13), 3903–3905.
- (23) Le Ru, E. C.; Etchegoin, P. G. Chapter 4 - SERS Enhancement Factors and Related Topics. In *Principles of Surface-Enhanced Raman Spectroscopy*; Ru, E. C. Le, Etchegoin, P. G., Eds.; Elsevier: Amsterdam, 2009; pp 185–264.
- (24) Greenler, R. G. Infrared Study of Adsorbed Molecules on Metal Surfaces by Reflection Techniques. *J. Chem. Phys.* **1966**, *44* (1), 310–315.
- (25) Suzuki, Y.; Osawa, M.; Hatta, A.; Suëtaka, W. Mechanism of Absorption Enhancement in Infrared ATR Spectra Observed in the Kretschmann Configuration. *Appl. Surf. Sci.* **1988**, *33–34* (0), 875–881.
- (26) Liao, P. F.; Wokaun, A. Lightning Rod Effect in Surface Enhanced Raman Scattering. *J. Chem. Phys.* **1982**, *76* (1), 751–752.
- (27) King, F. W.; Van Duyne, R. P.; Schatz, G. C. Theory of Raman Scattering by Molecules Adsorbed on Electrode Surfaces. *J. Chem. Phys.* **1978**, *69* (10), 4472–4481.

- (28) Salisbury, J. .; Wald, A. . The Role of Volume Scattering in Reducing Spectral Contrast of Reststrahlen Bands in Spectra of Powdered Minerals. *Icarus* **1992**, 96 (1).
- (29) Optical Distortions such as the Reststrahlen Effect, Where the Sample Becomes a Strong Reflector near an Absorption Band and Christiansen Effect Where the Sample Exhibits Anomalous Dispersion near an Absorption Band Are Often Observed in Inorganic Films B.
- (30) Allara, D. L.; Baca, A.; Pryde, C. A.; Laboratories, B.; Hill, M. Distortions of Band Shapes in External Reflection Infrared Spectra. **1978**, 11 (6), 4–9.
- (31) More, K. L. *VII.I.2 Microstructural Characterization of Polymer Electrolyte Membrane Fuel Cell (PEMFC) Membrane Electrode Assemblies (MEAs)*.
- (32) Kocha, S. S.; Zack, J. W. J.; Alia, S. M. S.; Neyerlin, K. C.; Pivovar, B. S. Influence of Ink Composition on the Electrochemical Properties of Pt/C Electrocatalysts. *ECS Trans.* **2013**, 50 (2), 1475–1485.
- (33) Jomori, S.; Komatsubara, K.; Nonoyama, N.; Kato, M.; Yoshida, T. An Experimental Study of the Effects of Operational History on Activity Changes in a PEMFC. *J. Electrochem. Soc.* **2013**, 160 (9), F1067–F1073.
- (34) Kreuer, K. D. On the Development of Proton Conducting Polymer Membranes for Hydrogen and Methanol Fuel Cells. *J. Memb. Sci.* **2001**, 185, 29–39.
- (35) Paddison, S.; Gasteiger, H. PEM Fuel Cells, Materials and Design Development Challenges. In *Fuel Cells*; Kreuer, K.-D., Ed.; Springer New York, 2013; pp 341–367.
- (36) Eastman, S. A.; Kim, S.; Page, K. A.; Rowe, B. W.; Kang, S.; Soles, C. L.; Yager, K. G. Effect of Confinement on Structure, Water Solubility, and Water Transport in NAFION Thin Films. *Macromolecules* **2012**, 45 (19), 7920–7930.
- (37) Bass, M.; Berman, A.; Singh, A.; Konovalov, O.; Freger, V. Surface-Induced Micelle Orientation in NAFION Films. *Macromolecules* **2011**, 44 (8), 2893–2899.
- (38) Bass, M.; Berman, A.; Singh, A.; Konovalov, O.; Freger, V. Surface Structure of NAFION in Vapor and Liquid. *J. Phys. Chem. B* **2010**, 114 (11), 3784–3790.
- (39) Modestino, M. A.; Paul, D. K.; Dishari, S.; Petrina, S. A.; Allen, F. I.; Hickner, M. A.; Karan, K.; Segalman, R. A.; Weber, A. Z. Self-Assembly and Transport Limitations in Confined NAFION Films. *Macromolecules* **2013**, 46 (3), 867–873.
- (40) Dura, J. A.; Murthi, V. S.; Hartman, M.; Satija, S. K.; Majkrzak, C. F. Multilamellar Interface Structures in NAFION. *Macromolecules* **2009**, 42 (13), 4769–4774.
- (41) Ogata, Y.; Kawaguchi, D.; Yamada, N. L.; Tanaka, K. Multistep Thickening of NAFION Thin Films in Water. *ACS Macro Lett.* **2013**, 2 (10), 856–859.
- (42) Wood, D. L.; Chlistunoff, J.; Majewski, J.; Borup, R. L. NAFION Structural Phenomena at

- Platinum and Carbon Interfaces. *J. Am. Chem. Soc.* **2009**, *131* (50), 18096–18104.
- (43) Dishari, S. K.; Hickner, M. A. Antiplasticization and Water Uptake of NAFION Thin Films. *ACS Macro Lett.* **2012**, *1* (2), 291–295.
 - (44) Kongkanand, A. Interfacial Water Transport Measurements in NAFION Thin Films Using a Quartz-Crystal Microbalance. *J. Phys. Chem. C* **2011**, *115* (22), 11318–11325.
 - (45) Paul, D. D. K.; Karan, K.; Docoslis, A.; Giorgi, J. B.; Pearce, J. Characteristics of Self-Assembled Ultrathin NAFION Films. *Macromolecules* **2013**, *46* (9), 3461–3475.
 - (46) Paul, D. K.; McCreery, R.; Karan, K. Proton Transport Property in Supported NAFION Nanothin Films by Electrochemical Impedance Spectroscopy. *J. Electrochem. Soc.* **2014**, *161* (14), F1395–F1402.
 - (47) Paul, D. K.; Shim, H. K. (Key); Giorgi, J. B.; Karan, K. Thickness Dependence of Thermally Induced Changes in Surface and Bulk Properties of NAFION Nanofilms. *J. Polym. Sci. Part B Polym. Phys.* **2016**, n/a – n/a.
 - (48) Falk, M. An Infrared Study of Water in Perfluorosulfonate (NAFION) Membranes. *Can. J. Chem.* **1980**, *58*, 1495–1501.
 - (49) Korzeniewski, C.; Snow, D. E.; Basnayake, R. Transmission Infrared Spectroscopy as a Probe of NAFION Film Structure: Analysis of Spectral Regions Fundamental to Understanding Hydration Effects. *Appl. Spectrosc.* **2006**, *60* (6), 599–604.
 - (50) Paddison, S. J.; Elliott, J. a. Molecular Modeling of the Short-Side-Chain Perfluorosulfonic Acid Membrane. *J. Phys. Chem. A* **2005**, *109* (33), 7583–7593.
 - (51) Kunimatsu, K.; Bae, B.; Miyatake, K.; Uchida, H.; Watanabe, M. ATR-FTIR Study of Water in NAFION Membrane Combined with Proton Conductivity Measurements during Hydration/dehydration Cycle. *J. Phys. Chem. B* **2011**, *115* (15), 4315–4321.
 - (52) Kendrick, I.; Yakaboski, A.; Kingston, E.; Doan, J.; Dimakis, N.; Smotkin, E. S. Theoretical and Experimental Infrared Spectra of Hydrated and Dehydrated NAFION. *J. Polym. Sci. Part B Polym. Phys.* **2013**, *51* (18), 1329–1334.
 - (53) Hanawa, H.; Kunimatsu, K. In Situ ATR-FTIR Analysis of the Structure of NAFION–Pt/C and NAFION–Pt3Co/C Interfaces in Fuel Cell. *J. Phys. ...* **2012**.
 - (54) Kunimatsu, K.; Yoda, T.; Tryk, D. a; Uchida, H.; Watanabe, M. In Situ ATR-FTIR Study of Oxygen Reduction at the Pt/NAFION Interface. *Phys. Chem. Chem. Phys.* **2010**, *12* (3), 621–629.
 - (55) Danilczuk, M.; Lin, L.; Schlick, S.; Hamrock, S. J.; Schaberg, M. S. Understanding the Fingerprint Region in the Infra-Red Spectra of Perfluorinated Ionomer Membranes and Corresponding Model Compounds: Experiments and Theoretical Calculations. *J. Power Sources* **2011**, *196* (20), 8216–8224.

- (56) Warren, D. S.; McQuillan, J. Infrared Spectroscopic and DFT Vibrational Mode Study of Perfluoro(2-Ethoxyethane) Sulfonic Acid (PES), a Model NAFION Side-Chain Molecule. *J. Phys. Chem. B* **2008**, *112* (34), 10535–10543.
- (57) Davis, E. M.; Stafford, C. M.; Page, K. A. Elucidating Water Transport Mechanisms in NAFION Thin Films. *ACS Macro Lett.* **2014**, *3* (10), 1029–1035.
- (58) Malevich, D.; Zamlynny, V.; Sun, S.-G.; Lipkowski, J. In Situ Infrared Reflection Absorption Spectroscopy Studies of the Interaction of NAFION with the Pt Electrode Surface. *Zeitschrift für Phys. Chemie/International J. Res. Phys. Chem. Chem. Phys.* **2003**, *217* (5/2003), 513.
- (59) Zeng, J.; Jean, D.; Ji, C.; Zou, S. In Situ Surface-Enhanced Raman Spectroscopic Studies of NAFION Adsorption on Au and Pt Electrodes. *Langmuir* **2011**, *28* (1), 957–964.
- (60) Ono, Y.; Nagao, Y. Interfacial Structure and Proton Conductivity of NAFION at the Pt-Deposited Surface. *Langmuir* **2016**, *32* (1), 352–358.
- (61) Nagao, Y. Highly Oriented Sulfonic Acid Groups in a NAFION Thin Film on Si Substrate. *J. Phys. Chem. C* **2013**, *117* (7), 3294–3297.
- (62) Griffiths, P. R.; de Haseth, J. a. *Fourier Transform Infrared Spectrometry*; John Wiley & Sons, Inc.: Hoboken, NJ, USA, 2007.
- (63) Elabd, Y. A.; Hickner, M. A. Block Copolymers for Fuel Cells. *Macromolecules* **2010**, *44* (1), 1–11.
- (64) Bae, B.; Miyatake, K.; Watanabe, M. Synthesis and Properties of Sulfonated Block Copolymers Having Fluorenyl Groups for Fuel-Cell Applications. *ACS Appl. Mater. Interfaces* **2009**, *1* (6), 1279–1286.
- (65) Yeh, K.-Y.; Restaino, N. a.; Esopi, M. R.; Maranas, J. K.; Janik, M. J. The Adsorption of Bisulfate and Sulfate Anions over a Pt(111) Electrode: A First Principle Study of Adsorption Configurations, Vibrational Frequencies and Linear Sweep Voltammogram Simulations. *Catal. Today* **2013**, *202* (0), 20–35.
- (66) Pan, J.; Zhu, L.; Han, J.; Hickner, M. A. Mechanically Tough and Chemically Stable Anion Exchange Membranes from Rigid-Flexible Semi-Interpenetrating Networks. *Chem. Mater.* **2015**, *27* (19), 6689–6698.
- (67) Zhu, L.; Pan, J.; Wang, Y.; Han, J.; Zhuang, L.; Hickner, M. A. Multication Side Chain Anion Exchange Membranes. *Macromolecules* **2016**, *49* (3), 815–824.
- (68) Nunez, S. A.; Capparelli, C.; Hickner, M. A. N-Alkyl Interstitial Spacers and Terminal Pendants Influence the Alkaline Stability of Tetraalkylammonium Cations for Anion Exchange Membrane Fuel Cells. *Chem. Mater.* **2016**.
- (69) Ran, J.; Wu, L.; Wei, B.; Chen, Y.; Xu, T. Simultaneous Enhancements of Conductivity and

- Stability for Anion Exchange Membranes (AEMs) through Precise Structure Design. *Sci. Rep.* **2014**, *4*, 6486.
- (70) CADOTTE, J. E. Evolution of Composite Reverse Osmosis Membranes. In *Materials Science of Synthetic Membranes*; ACS Symposium Series; American Chemical Society, 1985; Vol. 269, pp 12–273.
 - (71) Petersen, R. J. Composite Reverse Osmosis and Nanofiltration Membranes. *J. Memb. Sci.* **1993**, *83* (1), 81–150.
 - (72) Khorshidi, B.; Thundat, T.; Fleck, B. A.; Sadrzadeh, M. A Novel Approach Toward Fabrication of High Performance Thin Film Composite Polyamide Membranes. *Sci. Rep.* **2016**, *6*, 22069.
 - (73) Freger, V. Kinetics of Film Formation by Interfacial Polycondensation. *Langmuir* **2005**, *21* (5), 1884–1894.
 - (74) Arthur, S. D. Structure-Property Relationship in a Thin Film Composite Reverse Osmosis Membrane. *J. Memb. Sci.* **1989**, *46* (2), 243–260.
 - (75) Bowen, W. R.; Doneva, T. A.; Stoton, J. A. G. The Use of Atomic Force Microscopy to Quantify Membrane Surface Electrical Properties. *Colloids Surfaces A Physicochem. Eng. Asp.* **2002**, *201* (1–3), 73–83.
 - (76) Freger, V. Nanoscale Heterogeneity of Polyamide Membranes Formed by Interfacial Polymerization. *Langmuir* **2003**, *19* (11), 4791–4797.
 - (77) Kim, S. H.; Kwak, S. Y.; Suzuki, T. Positron Annihilation Spectroscopic Evidence to Demonstrate the Flux-Enhancement Mechanism in Morphology-Controlled Thin-Film-Composite (TFC) Membrane. *Environ. Sci. Technol.* **2005**, *39* (6), 1764–1770.
 - (78) Puffr, R.; Šebenda, J. On the Structure and Properties of Polyamides. XXVII. The Mechanism of Water Sorption in Polyamides. *J. Polym. Sci. Part C Polym. Symp.* **1967**, *16* (1), 79–93.
 - (79) Lim, L.; Britt, I. J.; Tung, M. A. Sorption and Transport of Water Vapor in Nylon 6, 6 Film. *J. Appl. Polym. Sci.* **1998**, *71* (2), 197–206.
 - (80) Tang, C. Y.; Kwon, Y. N.; Leckie, J. O. Probing the Nano- and Micro-Scales of Reverse Osmosis Membranes-A Comprehensive Characterization of Physiochemical Properties of Uncoated and Coated Membranes by XPS, TEM, ATR-FTIR, and Streaming Potential Measurements. *J. Memb. Sci.* **2007**, *287* (1), 146–156.
 - (81) Tang, C. Y.; Kwon, Y.-N.; Leckie, J. O. Effect of Membrane Chemistry and Coating Layer on Physiochemical Properties of Thin Film Composite Polyamide RO and NF Membranes: I. FTIR and XPS Characterization of Polyamide and Coating Layer Chemistry. *Desalination* **2009**, *242* (1–3), 149–167.

- (82) Pacheco, F. A.; Pinnau, I.; Reinhard, M.; Leckie, J. O. Characterization of Isolated Polyamide Thin Films of RO and NF Membranes Using Novel TEM Techniques. *J. Memb. Sci.* **2010**, 358 (1–2), 51–59.
- (83) Kang, G.-D.; Gao, C.-J.; Chen, W.-D.; Jie, X.-M.; Cao, Y.-M.; Yuan, Q. Study on Hypochlorite Degradation of Aromatic Polyamide Reverse Osmosis Membrane. *J. Memb. Sci.* **2007**, 300 (1–2), 165–171.
- (84) Antony, A.; Fudianto, R.; Cox, S.; Leslie, G. Assessing the Oxidative Degradation of Polyamide Reverse Osmosis membrane—Accelerated Ageing with Hypochlorite Exposure. *J. Memb. Sci.* **2010**, 347 (1–2), 159–164.
- (85) Jin, Y.; Su, Z. Effects of Polymerization Conditions on Hydrophilic Groups in Aromatic Polyamide Thin Films. *J. Memb. Sci.* **2009**, 330 (1–2), 175–179.
- (86) Johnson, P. M.; Yoon, J.; Kelly, J. Y.; Howarter, J. a.; Stafford, C. M. Molecular Layer-by-Layer Deposition of Highly Crosslinked Polyamide Films. *J. Polym. Sci. Part B Polym. Phys.* **2012**, 50 (3), 168–173.
- (87) Wei, J.; Liu, X.; Qiu, C.; Wang, R.; Tang, C. Y. Influence of Monomer Concentrations on the Performance of Polyamide-Based Thin Film Composite Forward Osmosis Membranes. *J. Memb. Sci.* **2011**, 381 (1–2), 110–117.
- (88) Ishigami, T.; Amano, K.; Fujii, A.; Ohmukai, Y.; Kamio, E.; Maruyama, T.; Matsuyama, H. Fouling Reduction of Reverse Osmosis Membrane by Surface Modification via Layer-by-Layer Assembly. *Sep. Purif. Technol.* **2012**, 99, 1–7.
- (89) Devanathan, R. Recent Developments in Proton Exchange Membranes for Fuel Cells. *Energy Environ. Sci.* **2008**, 1 (1), 101–119.

Chapter 3

Experimental Techniques: Theory And Applications

3.1 Introduction

This chapter introduces the methods used to prepare spin cast samples on gold and silicon substrates for FTIR analysis as well as the sampling geometries we used to characterize NAFION and polyamide thin films. Transmission, ATR and RAIRS are mature characterization geometries that are well discussed in literature.^{1,2} Hence only a brief summary of the experimental parameters shall be presented here. SO-ATR on the other hand is still poorly understood and we shall present the theoretical basis for the use of this method in determining molecular orientation. While ATR has been used to determine orientation by changing polarizations and calculating the dichroic ratio^{3,4} we required a method that would be equally capable of orientation of very thin films on gold, platinum or silicon substrates.

3.2 Materials and Sample Preparation

3.2.1 NAFION thin films

Thin film samples were prepared by dilution of a 20 weight % NAFION solution (DE2020, Ion Power, Inc., New Castle, DE) with isopropyl alcohol to achieve the desired polymer concentrations for thin film formation by spin coating. Double polished undoped silicon wafers (Silicon Valley Microelectronics, Inc., Santa Clara, CA) with native oxide, a resistivity above 10,000 ohm-cm and a thickness of 300 μm . These wafers were cleaved into 2 cm \times 2 cm pieces,

rinsed with methanol, dried under flowing air, and UV-ozone treated for 60 min. Gold substrates were prepared on silicon wafers using thermal evaporation with chromium as an adhesion layer. A bake out process for contaminant removal was used for chromium for 30 min and gold for 60 min prior to deposition. The thermal evaporation process took place at a base pressure of 7×10^{-7} torr at a rate of 3 Å/sec until a thickness of 20 nm and 50 nm was achieved for chromium and gold, respectively. The spin-coating speed was held constant at 3000 rpm (Headway Research, 1-PM101D-R, Garland, TX) and the weight percentage of NAFION in solution was varied to yield the desired polymer film thicknesses.

After spin casting the samples were dried in a vacuum oven at 40 °C overnight. All samples were analyzed in the as cast form with no annealing. For bulk membrane measurements, commercial NAFION 117 membranes (IEC = 0.91 meq/g) were used (Sigma-Aldrich, St. Louis, MO).

Thickness values for NAFION films were measured using a J.A. Woollam Alpha-SE spectroscopic ellipsometer (Lincoln, NE). The wave amplitude (Ψ) and phase shift (Δ) was measured at 188 wavelengths over a spectral range of 360-900 nm (1.377-3.44 eV) at 65°, 70°, and 75° for 30 seconds at each angle. The samples were modeled as a stacked multilayer system with silicon as the substrate and an oxide layer where the thickness was fit using measurements of the bare substrate prior to thin film deposition. The polymer thin film was then modeled as a uniform Cauchy layer with no surface roughness where the thickness and optical parameters B and C in the two term Cauchy equation below were allowed to fit.

$$n(\lambda) = A + \frac{B}{\lambda^2} + \frac{C}{\lambda^4} \quad (3-1)$$

3.2.2. Polyamide thin film composite membranes

Commercial thin film composite membranes with different chemical compositions and properties were obtained courtesy of Dow Water & Process Solutions. The supported active layers of the membranes were removed from the nonwoven fabric such that just the poly(sulfone) and polyamide layer remained. The polyamide layer was transferred to a silicon substrate or calcium fluoride window as follows. The membrane was placed polyamide side down on the substrate or window which had been previously wetted by a drop of ethanol to promote adhesion. The substrate supported membrane was then washed with sufficient dimethylformamide (DMF) to remove the poly(sulfone) layer. To remove the DMF, the sample was washed with water followed by methanol and then allowed to dry at 50 °C under vacuum for 20 h.

mLbL samples on gold and silicon were prepared at NIST in an in-house developed multi deposition unassisted spin assembly (MDUSA) spin coater under a constant dry nitrogen purge. A 1% wt/vol solution of each monomer in was prepared using H₂O-free toluene. The silicon and gold substrates were prepared as described above for the preparation of NAFION samples. In the spin coating process, the TMC solution was spin coated on substrate first followed by a brief rest step before the substrate was spun dry. This was followed by a rinse with H₂O-free acetone. This constituted a half layer (or half cycle). Following the rinse step The MPD solution was coated on top of the TMC half layer followed by a rest step to allow the monomers to react. The sample was again spun dry before a rinse with acetone to complete the first cycle. The process was then repeated for each subsequent cycle.⁵ Research is still ongoing to understand and optimize rinse times, rinse solvents, rest times and initial monomer concentrations. The thickness of each sample prepared was measured using SE as described above for NAFION samples.

3.3 Fourier Transform Infrared Spectroscopy (FTIR) Sampling Methods

All experiments were carried out on a Bruker vertex 70 spectrometer equipped with a wide band mercury cadmium telluride (MCT) detector which provided a wide spectral window with a detectivity of $5 \times 10^9 \text{ cm} \cdot \text{Hz}^{1/2} \cdot \text{W}^{-1}$. The spectrometer and external optics were purged with CO_2 -free, dry air or nitrogen gas. Measurements were carried out at an optical velocity on the order of $3.9 \text{ cm} \cdot \text{s}^{-1}$ and spectra were converted to absorbance and processed using Opus 6.0 software. Unless otherwise stated, a Norton-Beer medium apodization function was applied to allow quantitative measurements if needed as it provides the best linearity of absorbance versus concentration.^{1,6} A Mertz phase correction function was applied along with a zero filling factor of 8. A ZnSe wire grid polarizer was used to set the polarization of the incident beam to s or p-polarized.

Transmission spectra were recorded for pressed disk samples of dispersions of the pure material in KBr. 100 scans were averaged at a resolution of 4 cm^{-1} and an aperture setting (j-stop value) of 0.5mm. The corresponding spectral intensities are reported as $-\log(T/T_0)$, where T and T_0 are the transmitted peak power through KBr disks with and without the polymer added, respectively.

Reflectance absorbance infrared spectroscopy (RAIRS) experiments were carried out on a Veemax variable angle Accessory (Pike technologies) with a 2 cm sooted specular mask. The accessory was aligned and optimized using a pristine gold mirror before each experiment. An incidence angle of between 65° and 80° was selected depending on sample thickness and signal requirements. In general, when a comparison was required between SO-ATR and RAIRS an incident angle of 65° was selected and when data analysis was based solely on RAIRS data an incident angle closer to 80° was selected. 500 to 1000 scans were averaged with p-polarized light and the instrument resolution set to 4 cm^{-1} with an aperture setting of 5 mm. Reflection spectral

intensities are reported as $-\log(R/R_0)$, where R is the power reflectivity of the IR beam and R_0 is the reflectivity of a bare gold reference sample.

Brewster angle experiments were carried out using a rotating transmission sample holder (Harrick Scientific, City) at an incident angle of 74° which is the Brewster angle for silicon. Samples for Brewster angle experiments were prepared on optically pure undoped double side polished silicon substrates. 100 to 400 scans were averaged with unpolarized, s and p-polarized light and the instrument resolution set to 5 cm^{-1} with an aperture setting of 6 mm.

ATR experiments were carried out on a Harrick Scientific variGATR accessory with a germanium hemisphere at 65° incident angle. A digital read-out force meter was employed for measurement of the force applied to achieve contact between the ATR crystal and the sample. The force applied was replicated within 5 N for all experiments to minimize effects of variable physical contact.⁷ When varying the incident angle beyond $60 - 65^\circ$ was required, a VeeMax variable angle accessory modified to accept 2 cm diameter hemispherical ATR element was used. 100 to 400 scans were averaged with unpolarized, s and p-polarized light and the instrument resolution set to 4 cm^{-1} with an aperture setting of 5 mm. As the film thickness was typically less than the penetration depth no ATR correction algorithms were required.⁸ SO-ATR experiments were carried out on a variGATR accessory using the same experimental parameters as ATR. The sampling geometry and theoretical aspects related to it are described below.

3.4 SO-ATR Sampling Geometry

In SO-ATR, the experimental geometry consists of a germanium hemisphere, sample, and a high refractive index overlayer with the infrared beam at an incident angle of $60^\circ - 65^\circ$, Figure 3-1. An evanescent wave propagates through the sample and can be divided into x, y and z components

(Figure 3-1), with the y component constituting s-polarized electric field and the sum of x and z components constituting the p-polarized electric field.

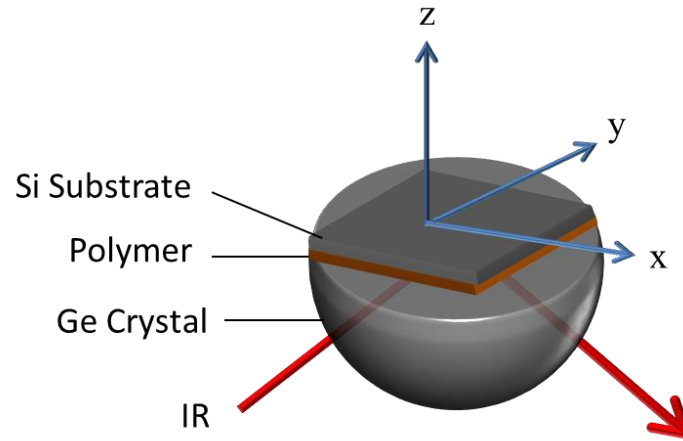


Figure 3-1. the experimental geometry of an SO-ATR experiment the evanescent wave propagating through the sample can be envisaged as comprising of some components in x y and z directions labelled.

In an ATR experiment, the observed signal is in the form of reflectance. At a given wavelength, the reflectivity of a three-layer system consisting of a prism (layer 1), sample (layer 2) and substrate over layer (layer 3) with the geometry shown in Figure 3-1, can be calculated using the Fresnel equations. Where θ is the incident angle, n_i is the refractive index of layer i , d_i the thickness of layer i , and the Fresnel coefficients for reflectance and transmittance between layers i and j are r_{ij} and t_{ij} , respectively.

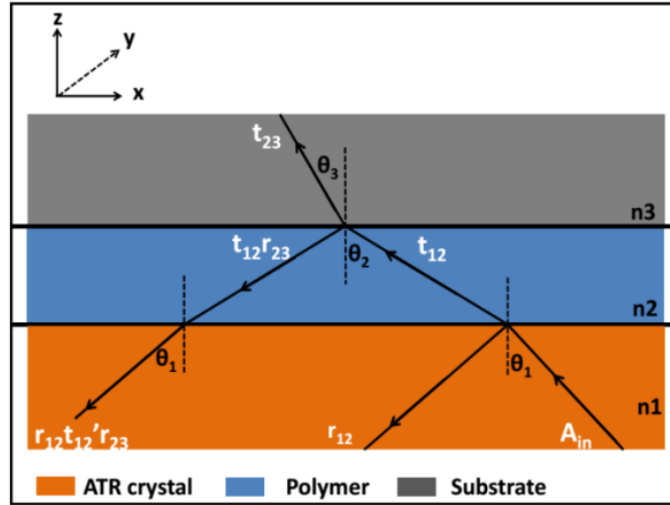


Figure 3-2. Three-layer optical system of the SO-ATR geometry showing reflection and transmission of an incident beam through the three-layer system, only one of the multiple internal reflections within the film is shown.

To calculate the reflectivity in the three layer system used for the ATR experiment, the Fresnel coefficients for the reflection must be calculated.⁹ In the calculation of the Fresnel coefficients the dielectric constant (ϵ) is taken to be the square of the complex refractive index (n). The p and s Fresnel coefficients for the crystal sample interface are given by equations (3-2) and (3-3), respectively:¹⁰

$$r_{12}^p = \frac{\epsilon_2 \xi_1 - \epsilon_1 \xi_2}{\epsilon_2 \xi_1 + \epsilon_1 \xi_2} \quad (3-2)$$

$$r_{12}^s = \frac{\xi_1 - \xi_2}{\xi_1 + \xi_2} \quad (3-3)$$

$$\text{where, } \xi_j = n_j \cos \theta_j = \sqrt{\varepsilon_j - \varepsilon_1 \sin^2 \theta} \quad (3-4)$$

and r^x is the Fresnel coefficient at polarization x , ε is the dielectric constant, θ is incident angle, and n_j is the refractive index of layer j . Similarly, for the sample/substrate interface, the Fresnel reflection coefficients for p and s-polarization are:

$$r_{23}^p = \frac{\varepsilon_3 \xi_2 - \varepsilon_2 \xi_3}{\varepsilon_3 \xi_2 + \varepsilon_2 \xi_3} \quad (3-5)$$

$$r_{23}^s = \frac{\xi_2 - \xi_3}{\xi_2 + \xi_3} \quad (3-6)$$

As the wave traverses the sample film it changes phase (β) which can be expressed as:¹¹

$$\beta = \frac{2\pi}{\lambda} n_2 d_2 \cos \theta_2 \quad (3-7a)$$

$$= 2\pi \tilde{\nu} d_2 \xi_2 \quad (3-7b)$$

where $\tilde{\nu}$ is the wavenumber of the incident light and d_2 is the thickness of the sample film. Below the critical angle, the electromagnetic wave refracts into the sample film and propagates to the sample substrate interface as shown in Figure 3-2. The resulting electric field is an infinite sum of all the partially reflected waves and can be expressed as a Taylor series to give the total reflected field amplitude (ρ) as follows:

$$\rho = r_{12}^\sigma + t_{12}^\sigma t_{12}'^\sigma r_{23}^\sigma e^{-2i\beta} - t_{12}^\sigma t_{12}'^\sigma r_{12}^\sigma r_{23}^\sigma e^{-4i\beta} + \dots \quad (3-8a)$$

$$= r_{12}^\sigma + \frac{t_{12}^\sigma t_{12}'^\sigma r_{23}^\sigma e^{-2i\beta}}{1 + r_{12}^\sigma r_{23}^\sigma e^{-2i\beta}} \quad (3-8b)$$

From conservation of energy, the sum of reflection and transmission coefficients is 1 hence:¹¹

$$t_{12}t'_{12} = 1 - r_{12}^2 \quad (3-9)$$

So equation (3-8) becomes:

$$\rho = \frac{r_{12}^\sigma + r_{23}^\sigma e^{-2i\beta}}{1 + r_{12}^\sigma r_{23}^\sigma e^{-2i\beta}} \quad (3-10)$$

The square of the absolute value of ρ gives the reflectance.¹² Hence:

$$absorbance = |\rho|^2 \quad (3-11)$$

For thin films above the critical angle, each term in equation 8a remains meaningful. However, as the higher terms become more significant, the phase shifts are negligible and constructive interference occurs for all electric field components perpendicular to the interface. This constructive interference greatly enhances the electric field and hence the absorbance. Solving equations 10 and 11 for absorbance for a range of film thicknesses demonstrates that films with thicknesses of less than 50 nm have a much higher absorbance than thicker films. P-polarized Fresnel coefficients were calculated from equations 1 and 4 and the parameters in Table 3-1 were used to perform the calculation of absorbance in the SO-ATR geometry from equations 3-10 and 3-11 yielding Figure 3-3.

Table 3-1. Modeling parameters used to simulate optical absorbance of NAFION in grazing angle SO-ATR.

Parameter	value
Crystal refractive index	4
Sample refractive index	$1.36 + 0.001 i$
Substrate refractive index	3.45
Incident angle	65
Wavenumber (cm^{-1})	1050

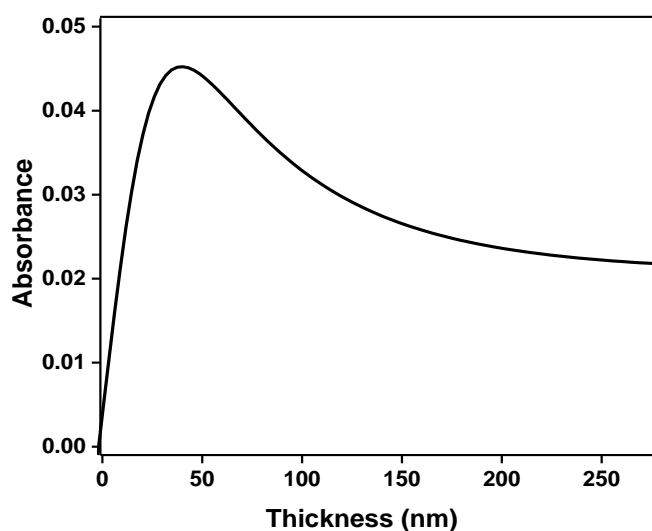


Figure 3-3. Optical absorbance at 1050 cm^{-1} as a function of thickness for a NAFION film on a silicon substrate based on parameters in Table 2.

The origin of this increased sensitivity for thin films and its implications in understanding the polarization during FTIR measurements is best explained by considering the electric fields within the sample. When light strikes the interface between the surface of the ATR crystal and the sample, the evanescent wave propagates in three directions, assigned x, y and z coordinates. At the crystal-sample interface, the electric field amplitude in the three directions is given by the following relationships:¹³

$$E_{y0} = \frac{2\cos\theta}{(1-n_{21}^2)^{\frac{1}{2}}} \quad (3-12a)$$

$$E_{x0} = 2 \frac{(\sin^2\theta - n_{21}^2)^{\frac{1}{2}} \cos\theta}{(1-n_{21}^2)^{\frac{1}{2}}[(1+n_{21}^2)^{\frac{1}{2}} \sin^2\theta - n_{21}^2]^{\frac{1}{2}}} \quad (3-12b)$$

$$E_{z0} = \frac{2\sin\theta \cos\theta}{(1-n_{21}^2)^{\frac{1}{2}}[(1+n_{21}^2)^{\frac{1}{2}} \sin^2\theta - n_{21}^2]^{\frac{1}{2}}} \quad (3-12c)$$

$$\text{where, } n_{21} = \frac{n_2}{n_1} \quad (3-13)$$

The electric fields inside the sample film, E_x , E_y , and E_z , can be expressed in terms of the incident electric fields film E_{x0} , E_{y0} , and E_{z0} .

$$E_x = \frac{(1-\rho r_{12})e^{2\pi i \tilde{\nu} z \beta} - (\rho - r_{12})e^{-2\pi i \tilde{\nu} z \beta}}{n_1 t_{21}} \beta E_{x0} \quad (3-14a)$$

$$E_y = \frac{(1-\rho r_{12})e^{2\pi i \tilde{\nu} z \beta} + (\rho - r_{12})e^{-2\pi i \tilde{\nu} z \beta}}{t_{21}} E_{y0} \quad (3-14b)$$

$$E_z = \frac{(1-\rho r_{12})e^{2\pi i \tilde{\nu} z \beta} - (\rho - r_{12})e^{-2\pi i \tilde{\nu} z \beta}}{n_2 t_{21}} n_1 E_{z0} \sin\theta \quad (3-14c)$$

Since p-polarization is obtained in the x and z directions and s-polarization in the y direction, the p and s electric fields can be computed as follows:

$$E_{\perp} = (|E_{x0}|^2 + |E_{z0}|^2)^{1/2} \quad (3-15a)$$

$$E_{\parallel} = E_{y0} \quad (3-15b)$$

These electric field amplitudes rapidly decay within the thin film polymer sample. The strength of the electric field along a particular direction can be described by p factors which are defined as the

absolute value of the ratio of the electric field strength in the film to the incident electric field strength:¹⁴

$$P_x = \left| \frac{E_x}{E_{x0}} \right| \quad (3-16a)$$

$$P_y = \left| \frac{E_y}{E_{y0}} \right| \quad (3-16b)$$

$$P_z = \left| \frac{E_z}{E_{z0}} \right| \quad (3-16c)$$

As with the case with the electric fields given in equations 14-15, the P-factors for s and p-polarizations can be given as:

$$P_s = P_y \text{ and } P_p = (P_z + P_x)/2 \quad (3-17)$$

The electric field amplitudes P_s and P_p were calculated for the effective angle range in grazing angle ATR experiments ($60^\circ - 65^\circ$) for a 50 nm thick film without a substrate overlayer and with a silicon substrate overlayer. The intensity of the electric field in any direction is proportional to the square of the p-factor. The absorption of light is proportional to the intensity of radiation and hence proportional to the p-factor. Only the molecular dipole vector components parallel to the electric field direction are excited. The p-factor plots in Figure 3-4 show that the strength of p-polarized light is marginally greater than that of s-polarized light for an unconfined film. However, when an overlayer is applied above the 50 nm film to form the SO-ATR geometry, the intensity of the p-polarized component of the wave is almost 10 times higher than for s-polarized light.

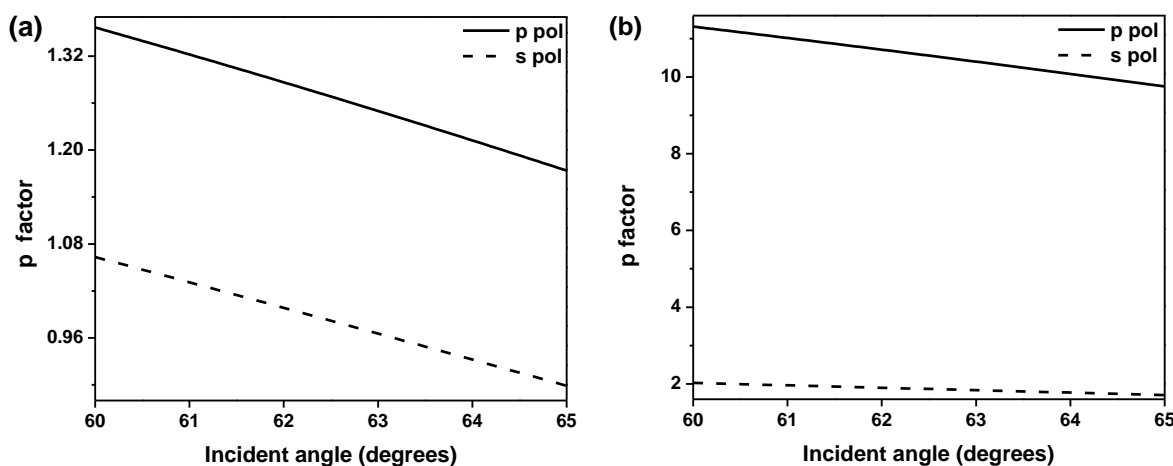


Figure 3-4. P-factors calculated from Equations 16-17 for a 50 nm NAFION film in (a) grazing angle ATR and (b) SO-ATR geometry. P-polarization is represented by the solid lines and s-polarization by the dashed lines. Note the different scales.

We can conclude from a simple optical model that the sampling details of the FTIR experiments will drastically influence the adsorption peaks in the spectrum and any preferential alignment at the interface will be greatly accentuated in SO-ATR geometry.

3.5 Spectral Simulation and Determination of Optical Constants

The first robust methods to simulate IR spectra were developed by Ishino and Ishida for uniaxially oriented organic films on non-metallic substrates.¹⁵ The work of Ishino and Ishida was based on a formal consideration of optical resonances in terms of transverse optical(TO) and

longitudinal optical (LO) modes and employed calculations based Drudes formula which employs a specific isotropic/uniaxial/isotropic 3 phase model.

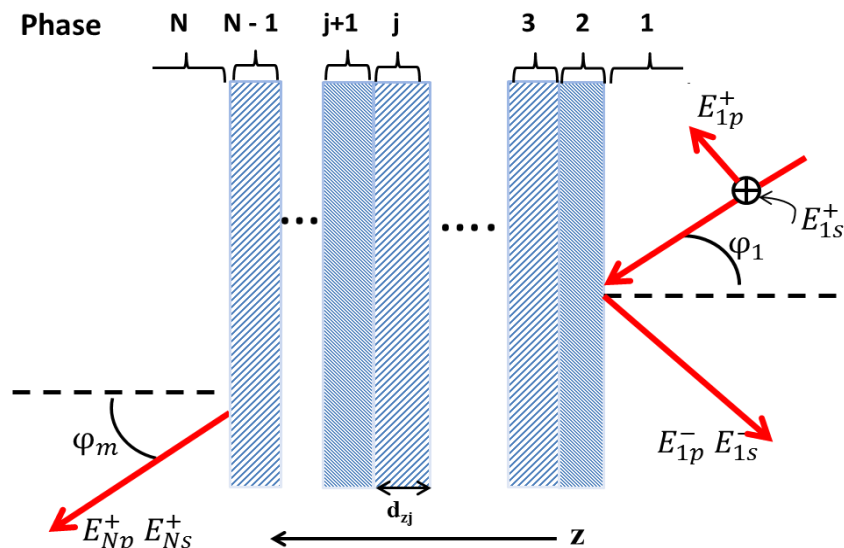


Figure 3-5. Parallel slab model for a multiphase, parallel-layer sample consisting of a total of N phases. Light approaches the sample from infinite phase 1 at an angle of incidence ϕ_1 . The directions of the electric field for s (out of plane) and p (in plane) polarizations are shown for incoming and outgoing propagation directions, designated by + and - superscripts, respectively.

Allara et al. on the other hand developed a more general procedure based on Greenler's¹⁶ and Hansen's⁹ multilayer reflectivity calculations.¹⁷⁻¹⁹ Experimental FTIR results are highly dependent on the experimental conditions such as polarization of the incident radiation, the experimental geometry, and the incident angle. Optical constants however are independent of the experimental method used, as they are a direct consequence of the interaction of radiation and matter.^{20,21} The exact relationship between optical constants and spectroscopic observables allows optical constants to provide insight into the molecular structure of a material making them ideal for characterizing materials and cross-referencing results obtained under different experimental conditions.

There are three approaches that have been used to extract optical constants from experimental measurements, namely, the Kramers-Kronig analysis,²² Harmonic oscillator parameterization^{23–25} and the two measurement method.^{26–29} While variations of the two latter methods have their advantages we have found the Kramers-Kronig analysis using an algorithm developed by the Allara group^{30,31} to be convenient and have determined optical constants from bulk KBr spectra as follows. In this analysis a multilayer thin film structure is modelled consisting of N semi-infinite, parallel slabs of definite thickness and homogeneous optical response.^{32,33} The incident beam is modelled as an infinite homogeneous, monochromatic plane wave of fixed frequency, ν , with the incidence of light on the sample defined in terms of an angle ϕ_1 in the plane of incidence θ and the azimuth of this plane from the chosen coordinate axes (in this case the XY plane) as shown in Figure 3-5. It is assumed that the x and y components of the propagation wave vector k is constant throughout the layered structure. The optical function of each phase is given by:³⁴

$$\hat{n}_j = n_j + ik_j \quad (3-18)$$

where n_j represents the real refractive index and k_j is the absorption coefficient for phase j . As shown in Figure 3-5, the incident complex electric field is given by E_1^+ the reflected field by E_1^- and the transmitted field by E_m^+ .

$$\begin{bmatrix} E_1^- \\ E_1^+ \end{bmatrix} \equiv E_1 = [R_{1,2} \prod_{j=3}^m P_{j-1} R_{j-1,j}] \begin{bmatrix} 0 \\ E_m^+ \end{bmatrix} \quad (3-19)$$

The matrix operator P is independent of polarization and defined as;

$$P_j \equiv \begin{bmatrix} e^{-ik_{zj}d_{zj}} & 0 \\ 0 & e^{ik_{zj}d_{zj}} \end{bmatrix} \quad (3-20)$$

where d_{zj} is the thickness of layer j and k_{zj} is the wave vector z projection. R is the matrix operator transforming the phase and direction of the complex electric field upon interaction with the interface for s and p-polarization and is given by:

$$R_{j-1,j}^s \equiv \frac{1}{2\alpha_{j-1}} \begin{bmatrix} (\alpha_{j-1} + \alpha_j) & (\alpha_{j-1} - \alpha_j) \\ (\alpha_{j-1} - \alpha_j) & (\alpha_{j-1} + \alpha_j) \end{bmatrix} \quad (3-21)$$

$$R_{j-1,j}^p \equiv \frac{1}{2\beta_{j-1}} \begin{bmatrix} (\beta_j + \beta_{j-1}) & (\beta_j - \beta_{j-1}) \\ (\beta_j - \beta_{j-1}) & (\beta_j + \beta_{j-1}) \end{bmatrix} \quad (3-22)$$

$$\text{Where } \alpha_j = \hat{n}_j \cos \varphi_j \quad (3-23)$$

$$\text{And } \beta_j = \hat{n}_j \cos \varphi_{j-1} \quad (3-24)$$

In a typical unpolarized transmission FTIR experiment, the transmissivity (T) is measured with the incident beam normal to the sample surface. In this case the p-polarized transmissivity is equal to the s-polarized transmissivity and is related to the complex transmission Fresnel coefficient (t) by:

$$T = \frac{n_m}{n_1} t t^* \quad (3-25)$$

where t^* is the complex conjugate of t , and t is given by:

$$t = \left(\frac{E_m^+}{E_1^+} \right) \quad (3-26)$$

The sample was ground into a fine powder using a wig-l-bug vibrating mill (Patterson Dental, Saint Paul, MN) in the case of aromatic polyamide films and in a cryo mill (Spex 6770, Metuchen, NJ) in the case of NAFION. The resulting sample was diluted with KBr to yield a final sample concentration of approximately 1% by weight in KBr which was further mixed and ground

for a minimum of 300 seconds in a wig-l-bug vibrating mill. The 300 second mixing step was performed to ensure sample homogeneity and minimize grinding effects that have that result in fluctuations in absorbance values and poor baselines.³⁵ The sample mixture was pressed into several 7 mm diameter pellets at a pressure of 2 tons in a hydraulic press and the transmission spectrum was collected soon after pellet preparation. IR spectra of blank KBr pellets of similar thickness were collected at humidity conditions identical to sample pellets. After collection of spectra the thickness of each pellet (d_z) was measured using a micrometer (Mitutoyo, Mason OH). For this transmission experiment we can write:

$$\frac{T}{T_0} = e^{-4\pi k' d_z \bar{\nu}} \quad (3-27)$$

where T is the transmissivity of the sample pellet and T_0 the transmissivity of the reference pellet. The absorbtion index k' is defined as kC/C_0 where k refers to the absorbtion index of the pure material and C and C_0 are the molar concentrations of the material in KBr and pure material phase, respectively. Using equation (3-26) gives estimated values of $k(\nu)$ which were used to calculate $n(\nu)$ values using the Kramers-Kronig transform:³⁶

$$n(\bar{\nu}_i) = n_\infty + \frac{1}{\pi} \int_{\bar{\nu}_2}^{\bar{\nu}_1} \frac{k(\bar{\nu}) \bar{\nu} d\bar{\nu}}{(\bar{\nu}^2 - \bar{\nu}_i^2)} \quad (3-28)$$

where $\bar{\nu}_i$ refers to the i th point in the frequency set. The initial set of $n(\bar{\nu})$ values is then used in a more rigorous calculation of a theoretical transmission spectrum. The $n(\bar{\nu})$ values are refined based on the differences between the simulated and experimental transmission spectra in an iterative process until convergence is achieved.

3.6 Determination of Orientation from Simulated and Experimental Spectra

The mathematical formulation of the selection rule for the activity of any excitation in the mid-IR spectrum is:²⁰

$$A \propto E^2 \langle j|\rho|i \rangle^2 \cos^2 \theta \quad (3-29)$$

where E is the electric field vector $\langle j|\rho|i \rangle$ is the transition dipole moment of a normal mode and θ is the angle between vectors E and the dynamic dipole moment.² From equation (3-28) it is apparent that the maximum absorption is observed when E is parallel to the dynamic dipole. As discussed previously for SO-ATR, E is greatly amplified resulting higher absorbance values, additionally E is surface normal hence maximum absorbance is observed when the dynamic dipole is surface normal. As the spectrum of an isotropic sample arises from the dynamic dipoles oriented equally in all directions it can be shown by integrating the cosine square function over all angles that transition dipole moment is aligned along the z axis gives an intensity for that mode 3 times that for random orientation, equation (3-29).³⁰ This argument is equally true for RAIRS where at grazing angles the electric field is essentially surface normal.

$$\frac{A_{\text{sample}}}{3A_{\text{isotropic}}} = \cos^2 \theta \quad (3-30)$$

From equation 3-29 it is clear that in SO-ATR and RAIRS it is possible to calculate the angle θ between the surface normal (which is parallel to the electric field) and dynamic dipole provided a measurement of an isotropic sample of the same chemical composition, thickness and on the same substrate can be obtained.³⁷ In our calculations the entry phase was defined as air with an infinite thickness for RAIRS calculations and as the ATR element for SO-ATR and ATR experiments. The optical constants for ATR crystal materials, Si, Au and the native oxide layer on silicon substrates were obtained from literature and previous experiments.³⁸⁻⁴⁰ For this analysis to be successful,

however, it must be applied to what are termed diagnostic modes which are vibrational modes with clearly resolvable peaks and clearly definable transition dipole moment direction.

It is often impossible to experimentally completely eliminate substrate effects and obtain an isotropic sample spectrum. To circumvent this problem, we used the bulk isotropic material to obtain optical constants from which the isotropic spectrum under experimental conditions was calculated. Comparing the absorbance of diagnostic modes in the RAIRS or SO-ATR spectrum to the model isotropic film gives the orientation of the functional group with respect to the surface normal, Figure 3-6.

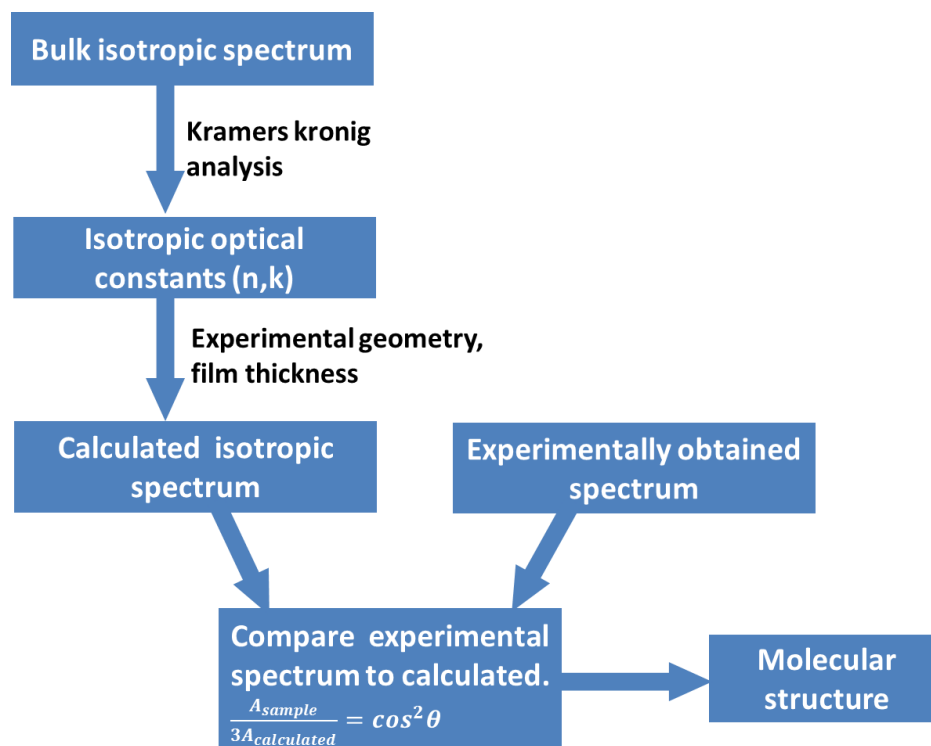


Figure 3-6. Flow chart depicting the determination of molecular ordering from experimental and calculated spectra. The simulated spectrum is calculated as parallel-layer multilayer system where the optical properties and thickness of each layer is defined by the experimental geometry and sample thickness.

3.7 References

- (1) Griffiths, P. R.; de Haseth, J. a. *Fourier Transform Infrared Spectrometry*; John Wiley & Sons, Inc.: Hoboken, NJ, USA, 2007.
- (2) Tolstoy, V. P.; Chernyshova, I. V; Skryshevsky, V. A. *Handbook of Infrared Spectroscopy of Ultrathin Films*; Wiley Interscience: New Jersey, 2003.
- (3) Everall, N. J.; Bibby, A. Improvements in the Use of Attenuated Total Reflection Fourier Transform Infrared Dichroism for Measuring Surface Orientation in Polymers. *Appl. Spectrosc.* **1997**, 51 (8), 1083.
- (4) Anariba, F.; Viswanathan, U.; Bocian, D. F.; McCreery, R. L. Determination of the Structure and Orientation of Organic Molecules Tethered to Flat Graphitic Carbon by ATR-FT-IR and Raman Spectroscopy. *Anal. Chem.* **2006**, 78 (9), 3104.
- (5) Johnson, P. M.; Yoon, J.; Kelly, J. Y.; Howarter, J. a.; Stafford, C. M. Molecular Layer-by-Layer Deposition of Highly Crosslinked Polyamide Films. *J. Polym. Sci. Part B Polym. Phys.* **2012**, 50 (3), 168.
- (6) Herres, W.; Gronholz, J. Understanding FT-IR Data Processing. Part 1: Data Acquisition and Fourier Transformation. *Instruments Comput.* **1984**.
- (7) Chen, J.; Gardella, J. A. Quantitative ATR FT-IR Analysis of Surface Segregation of Polymer Blends of Polystyrene/Poly(dimethylsilox an E)-Co-P Olystyrene. **1998**, 52 (3), 361.
- (8) Huang, J. B.; Urban, M. W. Evaluation and Analysis of Attenuated Total Reflectance FT-IR Spectra Using Kramers-Kronig Transforms. *Appl. Spectrosc.* **1992**, 46 (11), 1666.
- (9) Hansen, W. N. Electric Fields Produced by the Propagation of Plane Coherent

- Electromagnetic Radiation in a Stratified Medium. *J. Opt. Soc. Am.* **1968**, 58 (3), 380.
- (10) Osawa, M.; Kuramitsu, M.; Hatta, A.; Suëtaka, W.; Seki, H. Electromagnetic Effect in Enhanced Infrared Absorption of Adsorbed Molecules on Thin Metal Films. *Surf. Sci.* **1986**, 175 (3), L787.
 - (11) Heavens, O. S. *Optical Properties of Thin Films*; Dover publications, inc: New York, 1965.
 - (12) Milosevic, M.; Milosevic, V.; Berets, S. L. Grazing Angle Attenuated Total Reflection Spectroscopy: Fields at the Interface and Source of the Enhancement. *Appl. Spectrosc.* **2007**, 61 (5), 530.
 - (13) Harrick, N. J. *Internal Reflection Spectroscopy*; John Wiley & Sons: New York, 1967.
 - (14) Ishino, Y.; Ishida, H. Grazing Angle Metal-Overlayer Infrared ATR Spectroscopy. *Appl. Spectrosc.* **1988**, 42 (7), 1296.
 - (15) Ishino, Y.; Ishida, H. Spectral Simulation of Uniaxially Oriented Monolayers in the Infrared. *Langmuir* **1988**, 4 (6), 1341.
 - (16) Greenler, R. G. Infrared Study of Adsorbed Molecules on Metal Surfaces by Reflection Techniques. *J. Chem. Phys.* **1966**, 44 (1), 310.
 - (17) Allara, D. L.; Baca, A.; Pryde, C. A.; Laboratories, B.; Hill, M. Distortions of Band Shapes in External Reflection Infrared Spectra. **1978**, 11 (6), 4.
 - (18) Holmes, D. A.; Feucht, D. L. Polarization State of Thin-Film Reflection*. *J. Opt. Soc. Am.* **1965**, 55 (5), 577.
 - (19) Holmes, D. A.; Feucht, D. L. Electromagnetic Wave Propagation in Birefringent Multilayers*. *J. Opt. Soc. Am.* **1966**, 56 (12), 1763.
 - (20) Chalmers, J.; Griffiths, P. *Handbook of Vibrational Spectroscopy*; 2001.

- (21) Berreman, D. Optics in Stratified and Anisotropic Media: 4×4 -Matrix Formulation. *JOSA* **1972**, 62 (4).
- (22) Allara, D. L.; Nuzzo, R. G. Spontaneously Organized Molecular Assemblies. 2. Quantitative Infrared Spectroscopic Determination of Equilibrium Structures of Solution-Adsorbed N-Alkanoic Acids on an Oxidized Aluminum Surface. *Langmuir* **1985**, 1 (1), 52.
- (23) Verleur, H. W. Determination of Optical Constants from Reflectance or Transmittance Measurements on Bulk Crystals or Thin Films. *J. Opt. Soc. Am.* **1968**, 58 (10), 1356.
- (24) Ribbegård, G. K.; Jones, R. N. The Measurement of the Optical Constants of Thin Solid Films in the Infrared. *Appl. Spectrosc.* **1980**, 34 (6), 638.
- (25) Siqueiros, J. M.; Machorro, R.; Regalado, L. E. Determination of the Optical Constants of MgF₂ and ZnS from Spectrophotometric Measurements and the Classical Oscillator Method. *Appl. Opt.* **1988**, 27 (12), 2549.
- (26) Graf, R. T.; Koenig, J. L.; Ishida, H. Fourier Transform Infrared Ellipsometry of Thin Polymer Films. *Anal. Chem.* **1986**, 58 (1), 64.
- (27) Hansen, W. N. Expanded Formulas for Attenuated Total Reflection and the Derivation of Absorption Rules for Single and Multiple ATR Spectrometer Cells. *Spectrochim. Acta* **1965**, 21 (4), 815.
- (28) Fahrenfort, J.; Visser, W. M. On the Determination of Optical Constants in the Infrared by Attenuated Total Reflection. *Spectrochim. Acta* **1962**, 18 (9), 1103.
- (29) Hansen, W. N. On the Determination of Optical Constants by a Two-Angle Internal Reflection Method. *Spectrochim. Acta* **1965**, 21 (1), 209.
- (30) Parikh, A. N.; Allara, D. L. Quantitative Determination of Molecular Structure in Multilayered Thin Films of Biaxial and Lower Symmetry from Photon Spectroscopies. I.

- Reflection Infrared Vibrational Spectroscopy. *J. Chem. Phys.* **1992**, 96 (2), 927.
- (31) Parikh, A. N. Structural Characterization of Molecular Assemblies of Short Alkyl Chains at Planar Surfaces, Pennsylvania State University, 1994.
- (32) Yeh, P. Optical Waves in Layered Media. Wiley: Hoboken, NJ 2005, p x, 406 p.
- (33) Yeh, P. Electromagnetic Propagation in Birefringent Layered Media. *J. Opt. Soc. Am.* **1979**, 69 (5), 742.
- (34) Born, M.; Wolf, E. *Principles of Optics: Electromagnetic Theory of Propagation, Interference and Diffraction of Light*, 7th ed.; Cambridge University Press, 1999.
- (35) Arnold, R.; Terfort, A.; Woll, C. INTERFACES: ADSORPTION, REACTIONS, FILMS, ASSEMBLIES, FORCES-Determination of Molecular Orientation in Self-Assembled Monolayers Using IR Absorption Intensities: The Importance of. *Langmuir* **2001**, 17 (16), 4980.
- (36) Ohta, K.; Ishida, H. Comparison Among Several Numerical Integration Methods for Kramers-Kronig Transformation. *Appl. Spectrosc.* **1988**, 42 (6), 952.
- (37) Iida, K.; Imamura, Y.; Liao, C.; Nakamura, S.; Sawa, G. Evaluation of Molecular Orientation in Aromatic Polyimide Films by FT-IR Reflection Absorption Spectroscopy. *Polym. J.* **1996**.
- (38) Humlíček, J.; Lukeš, F.; Schmidt, E. Silicon—Germanium Alloys (SixGe1-X) A2 - Palik, Edward D. BT - Handbook of Optical Constants of Solids; Academic Press: Burlington, 1997; pp 607–636.
- (39) Lynch, D. W.; Hunter, W. R. Comments on the Optical Constants of Metals and an Introduction to the Data for Several Metals A2 - Palik, Edward D. BT - Handbook of Optical Constants of Solids; Academic Press: Burlington, 1997; pp 275–367.

- (40) Palik, E. D. Chapter 1 - Introductory Remarks BT - Handbook of Optical Constants of Solids; Academic Press: Burlington, 1997; pp 3–19.

Chapter 4

FTIR Analysis of Alignment in NAFION Thin Films at SiO₂ and Au Interfaces

This Chapter has been summarized in: Zimudzi, T. J.; Hickner, M. A. Signal Enhanced FTIR Analysis of Alignment in NAFION Thin Films at SiO₂ and Au Interfaces. ACS Macro Lett. 2016, 5 (1), 83.

4.1 Introduction

Ion-containing polymers like NAFION play an important role in applications including water purification, electrochemical cells, in sensors, and as solid-phase superacid catalysts in the production of chemicals.¹⁻³ These materials receive particular attention in the field of energy storage and conversion in devices such as solar-fuel generators,⁴ batteries,⁵ and fuel cells⁶ where a thin ionomer film is responsible for the transport of ions to and from active electro-catalytic sites. In fuel cells, the ion-conducting polymer in the catalytic layer provides mechanical strength, can influence transport in the porous electrode and binding of catalyst particles, and may play a significant role in determining the catalytic activity of the catalyst.⁷

NAFION-free platinum on carbon catalyst (Pt/C) electrodes have been found to show oxygen reduction reaction (ORR) catalytic activities that are higher by a factor of ~1.8 than Pt/C electrodes with NAFION incorporation in rotating disk experiments.⁷ It is thought that the specific adsorption of ionic groups on the Pt surface affects electro-catalytic kinetics by competing for active sites, changing the potential distribution in the interfacial region, and altering the electronic structure of the surface. Tripkovic, et al.⁸ studied the adsorption and electro-oxidation of carbon monoxide (CO)

on Pt(111) electrode surfaces by cyclic voltammetry and infrared reflection-absorption spectroscopy (IRRAS) in the presence of H_2SO_4 . The absorbance of the $\nu(\text{CO})$ band at 2060 cm^{-1} from adsorbed CO was found to increase linearly with potential only below 0.3 V (RHE) as opposed to previous reports⁹ which show a linear trend in absorbance of the $\nu(\text{CO})$ band up to 0.45 V. In Tripkovic, et al.'s study, a blueshift in $\nu(\text{CO})$ peak position was observed between 0.35 V and 0.5 V which was attributed to adsorption of inactive HSO_4^- resulting in repulsive CO/HSO_4^- interactions.⁸

Other spectroelectrochemical studies of sulfate (SO_4^{2-}) and bisulfate (HSO_4^-) adsorption have shown a potential-dependent band of symmetric vibrations between 1150 cm^{-1} and 1220 cm^{-1} due to sulfate anions of C_{v3} symmetry adsorbed via the three oxygen atoms. Hydrated sulfate adsorbs first at low potentials followed by bisulfate at slightly higher potentials. Faguy, et al.^{10,11} studying Pt(111) electrodes in HSO_4^- solutions ascribed the band at 1250 cm^{-1} to the asymmetric stretching mode of the bisulfate anion, adsorbed on threefold sites through the unprotonated oxygen atoms. This observation has been confirmed by computational studies.¹² The work involving adsorption of sulfate and bisulfate species from liquid electrolyte may inform studies of solid polymer electrolytes at catalytic interfaces, although the solid polymer/catalyst interface may be more complicated due to restricted functional group mobility and polymer chain exclusion effects.

A number of methods have been used to study ionomer/surface interactions in model systems including vibrational techniques such as surface enhanced Raman and Fourier transform infrared (FTIR) spectroscopies. Yet the specific nature of interactions between the ionic groups in NAFION and surfaces remains unclear and the chain conformations at the surface have been probed in just a few studies through scattering and spectroscopic techniques.¹³⁻¹⁵ NAFION is thought to interact with metallic surfaces anchored by the oxygen atoms of the $-\text{SO}_3^-$ group.¹⁶ The interaction of the $-\text{SO}_3^-$ with metallic surfaces appears to be similar to that of sulfate groups¹⁷ although there may be differences in adsorption potential due to acidity effects.¹² Polarization modulation-infrared

reflection absorption spectroscopy (PM-IRRAS) has been used by Kendrick, et al.¹⁶ to study the interface between NAFION and a Pt black catalyst in a membrane electrode assembly under operational conditions. The change in the 1260 cm^{-1} peak intensity led these authors to the conclusion that $\nu_{\text{as}}(\text{CF}_3)$ mode is mechanically coupled to the sulfonate pure mode ($\nu_{\text{as}}(\text{SO}_3^-)$) and $-\text{CF}_3$ groups on the sidechain coadsorb with the sulfonate groups.^{16,18} Kendrick's observations make it reasonable to believe that the adsorption of NAFION on surfaces may involve reordering of the hydrophobic backbone, which can sterically block catalytically active sites in addition to effects of the adsorbed sulfonate groups. IRRAS experiments have been carried out using a flat polycrystalline Pt electrode coated with a thin film of NAFION assembled into a thin layer spectroelectrochemical cell. In this study, Malevich, et al.¹⁹ showed that the doubly degenerate $\nu_{\text{as}}(\text{SO}_3^-)$ band at 1250 cm^{-1} dominated the potential modulated spectrum of NAFION on Pt electrodes. This spectral feature at 1250 cm^{-1} combined with the observations that $\nu_{\text{s}}(\text{SO}_3^-)$ at 1060 cm^{-1} and a band at 1400 cm^{-1} attributed to protonated $-\text{SO}_3\text{H}$ groups changed significantly with potential indicated that only the $-\text{SO}_3^-$ group participated in the adsorption process.¹⁹ NAFION adopts a multilamellar structure on silicon oxide surfaces and the morphology of NAFION films can vary with film thickness and processing conditions.^{20,21} On native silicon oxide surfaces, NAFION is most likely to interact with the surface by hydrogen bonding between surface silanol groups and sulfonate groups of NAFION, but chemical evidence of this bond has not been unambiguously established.

The ease of sample preparation by spin-coating or surface adsorption from NAFION solutions and speed of analysis has made FTIR a popular method for analyzing thin films. Several ATR sampling geometries have been successfully employed to study thin ionomer films, each with their own characteristics that must be considered in interpreting the data.^{22,23} Experiments at grazing incident angles with high refractive index ATR crystals in a crystal/sample/substrate geometry yield sensitivity significantly greater than in external reflection and transmission geometries.²⁴ To

understand the origin of the increased sensitivity in an ATR experiment it is necessary to consider the origin of the absorbance. The selection rule for the IR activity of any excitation can be represented mathematically as:

$$A \propto E^2 |j\langle\rho\rangle i|^2 \cos^2 \varphi \quad (4-1)$$

where E is the electric field vector, $|j\langle\rho\rangle i|$ is the transition dipole moment of the moiety being probed, and φ is the angle between the electric field vector and the dipole moment. An excitation is active if a change in the transition dipole moment occurs during bond vibration and the maximum absorbance is observed when E is parallel to the dipole. The relationship between polarization and molecular orientation in ATR-FTIR is well established and is based on the change in the angle φ as the polarization is changed, with $\varphi = 0$ for p-polarized light and $\varphi = 90$ for s-polarization.²⁵ A less explored aspect of polarization is its effect on the resulting strength of the electric field in specific geometries and hence the observed absorbance. Optical modeling can help one understand the nature of the electric field and models based on Fresnel equations have been used to calculate reflectance spectra and estimate the strength of the electric field by Greenler in external reflection and Milosevic in grazing angle ATR geometries.^{24,26,27} Greenler was able to demonstrate that the absorption factor varies linearly with film thickness in external reflection and that at grazing angles of around 88° the absorption factor can be up to 5000 times higher than at 0° . Milosevic demonstrated how substrate overlayer ATR on a Ge crystal at grazing angles can lead to an enhancement in absorbance of up to 13 times for thin films on silicon substrates. In the work reported here, an optical model similar to that established by Milosevic was employed to demonstrate the increase in electric field strength and p-polarization for a system comprising a Ge ATR crystal, a spin-coated NAFION thin film and Au or native oxide Si film substrate as the ATR overlayer. The results of these calculations were then used to explain the peak shifts observed at

1220 cm^{-1} and 1150 cm^{-1} in SO-ATR and to develop a detailed picture of NAFION adsorption to native oxide Si and Au surfaces.

4.2 Experimental Methods

4.2.1 FTIR sampling

Spectra were collected in SO-ATR, ATR, and Brewster angle geometries as described in Chapter 3. For ATR and SO-ATR experiments a surface pressure of 850 psi was maintained over the 20 mm diameter ATR hemispherical crystal for all experiments. The ATR crystal was cleaned with 2-butanone between measurements and a new reference spectrum was collected after cleaning. The incidence angle was set at 65° and a KRS-5 wire grid polarizer was set at 0° and 90° for s and p-polarized light at the crystal surface, respectively. The spectra were signal averaged over 100 scans at 4 cm^{-1} resolution with a 5 mm aperture size and a nitrogen purge at ambient temperature. For specular reflectance experiments the incident angle was maintained at 70° to the substrate. A zinc selenide (ZnSe) wire grid polarizer was set at 90° and 0° for s and p-polarized light, respectively. The spectra were signal averaged from 800 scans at 4 cm^{-1} resolution with a 5 mm aperture size and a CO_2 -free dry air purge at ambient temperature.

4.2.2 Thin film preparation

A 20 weight % NAFION solution (DE2020, Ion Power, Inc., New Castle, DE) was diluted with isopropyl alcohol to achieve the desired polymer concentrations for thin film formation by spin coating. Double polished undoped silicon wafers (Silicon Valley Microelectronics, Inc., Santa Clara, CA) with native oxide were cleaved into $2\text{ cm} \times 2\text{ cm}$ pieces, rinsed with methanol, dried

under flowing air, and UV-ozone treated for 60 min. Gold substrates were prepared on silicon wafers using thermal evaporation with chromium as an adhesion layer. The spin-coating speed was held constant at 3000 rpm (Headway Research, 1-PM101D-R, Garland, TX) and the weight percent of NAFION in solution was varied to yield the desired polymer film thicknesses, Table 4-1. We selected a thickness range of 5 to 250 nm as this the thickness range we and other researchers have observed anomalous physical behavior in NAFION thin films due to confinement effects.

Table 4-1. Weight percent NAFION solutions for spin coating and resulting film thickness by ellipsometric measurements.

Weight % NAFION solution	film thickness on silicon (nm)	weight % NAFION solution	film thickness on gold (nm)
2	256	2	230
0.75	100	1.5	200
0.5	58	0.5	73
0.25	25	0.2	18
0.2	12	0.15	7
0.1	5.6	0.1	5

4.3 Results and Discussion

4.3.1 Peak deconvolution and peak assignments

The broad envelope between 1100 cm^{-1} and 1300 cm^{-1} in the FTIR spectrum of NAFION has been extensively analyzed and deconvoluted and bands in this area have been assigned in a number of literature references. This region of the NAFION infrared spectrum has long been the focus of both theoretical and experimental research, however it is difficult to assign calculated vibrational frequencies to experimental spectra because of the large number of calculated modes in model compounds.²⁸ The interpretation of this spectral range is rendered difficult by the overlap of various vibrational modes of $-\text{CF}_2$, $-\text{SO}_3^-$ and $-\text{CF}_3$ functional groups.^{16,28-35} The situation is further complicated when one considers the addition of a substrate which may interact with NAFION thus ordering the polymer molecules and enhancing the absorbance of surface perpendicular dipoles due to increased p-polarization of the radiation as discussed above for certain sampling geometries.^{32,36} Chemical interactions between NAFION and the surface may also result in changes of the functional group bond energies which results in shifts of peak positions for the affected modes. Table 4-2 shows peak assignments relevant for the ensuing discussion based on density functional theory and experimental peak assignments for which there is the most consensus in literature.

Table 4-2. Peak assignment for predominant peaks in the NAFION ATR spectrum.

position (cm ⁻¹)	Assignment	reference
970	$\nu_s(\text{C-O-C})^a$	17, 33, 34, 35, 38
983	$\nu_s(\text{C-O-C})^b$	17, 33, 34, 38
992	$\nu_{as}(\text{C-O-C})^a$	35, 39
1056	$\nu_s(\text{SO}_3^-)$	17, 34, 35, 38
1124	$\nu_s(\text{CF}_2)$	33
1135	$\nu_{as}(\text{SO}_3^-) + \nu_s(\text{CF}_2)$	20, 33, 35, 39
1176	$\nu_{as}(\text{CF}_2)$	17, 33, 35
1191	$\nu_{as}(\text{CF}_3) + \nu_s(\text{CF}_2)$	17, 35
1204	$\nu_{as}(\text{SO}_3^-)$, $\nu_{as}(\text{CF}_2)$, $\nu_{as}(\text{CF}_3)$	33, 35
1232	$\nu_s(\text{CF}_3)$, $\nu_{as}(\text{CF}_2)$	35
1242	$\nu_{as}(\text{CF}_2)$	35, 39
1254	$\nu_{as}(\text{CF}_3) + \nu_{as}(\text{C-O-C})$	17, 33

a: ether closest to sulfonate group, b: ether closest to backbone.

4.3.2 Effect of polarization on the ATR spectrum of NAFION

It is well-established that changing the polarization of the incident light changes the absorption intensity for surface oriented molecules where a similar effect is not observed for randomly oriented molecules.^{23,26} The increase in p-polarization for thin NAFION films in SO-ATR, will increase absorption intensity for surface normal vibrational modes provided the molecules are ordered at the film-substrate interface. As the thickness of the film decreases, the z component of the evanescent wave becomes enhanced over the other directions resulting in higher signal than IRRAS or transmission experiments for transition dipoles with vector components in the z direction. Due to the increased contribution of the z component to the overall electric field, the evanescent wave increases in p-polarized character. This enhancement effect is confirmed by experimental absorbance measurements shown in Figure 4-1 which follow the trend predicted by calculations outlined in section 3.4 of chapter 3. The effect is similar on both silicon (Figure 4-1a)

and gold (Figure 4-1b) substrates but the absorbance values on gold substrates are slightly greater than the values for samples on silicon possibly due to plasmon resonance of the metallic substrate. There is a deviation of experimental absorbance values from the predicted values, Figure 4-2. This deviation could be a result of the complexity of the absorbing system and the contribution of alternative enhancement effects such as the surface plasmon effect on metallic substrates and a phonon resonance effect on silicon substrates.³⁷

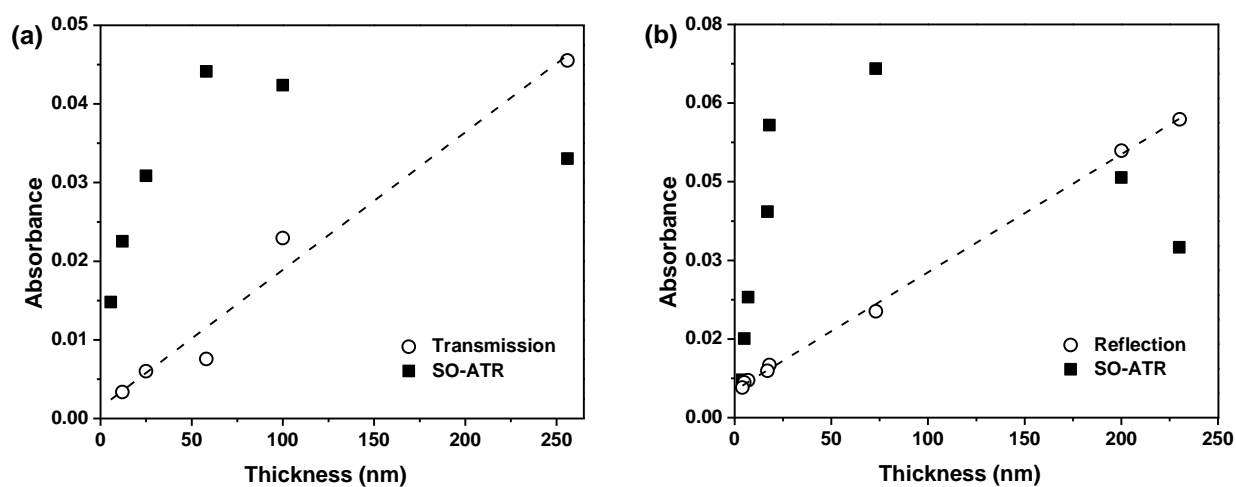


Figure 4-1. Experimental SO-ATR absorbance at 1050 cm^{-1} overlaid with a) transmission for silicon samples and b) reflection for gold samples.

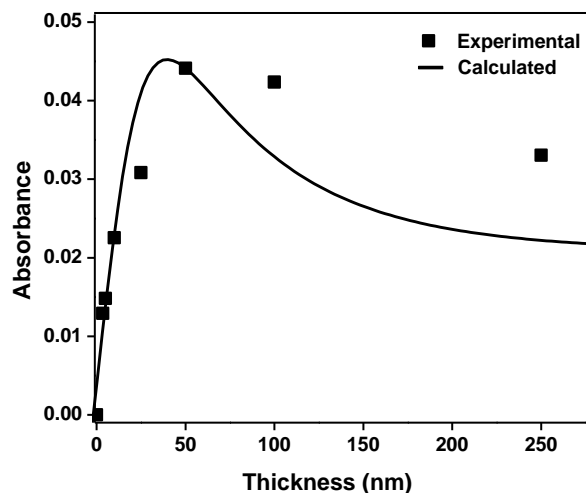


Figure 4-2. Experimental values for NAFION absorption at 1050 cm^{-1} on a native oxide silicon substrate overlayed with predicted values.

4.3.3 Orientation of NAFION on planar substrates

The change in the polarization character of the evanescent wave can be monitored by observing the change in peak position of the broad envelope between 1203 cm^{-1} and 1257 cm^{-1} , shown in Figure 4-3. This envelope is composed of primarily --CF_2 symmetric and asymmetric stretches, --CF_3 asymmetric stretches and --SO_3^- asymmetric stretch bands. The position of the peak between 1203 cm^{-1} and 1257 cm^{-1} depends on which vibrational modes are in plane or out of plane with respect to the incident electric field. As the chain aligns parallel to the surface, the backbone $\nu_{\text{as}}(\text{CF}_2)$ band will be enhanced in p-polarized light. As a result of this intensity enhancement the spectral region between 1203 and 1257 cm^{-1} becomes dominated by the higher frequency $\nu_{\text{as}}(\text{CF}_2)$ bands at 1232 and 1242 cm^{-1} resulting in absorbance maximum close to 1257 cm^{-1} . With s-polarized incident light in SO-ATR, there is an enhancement of lower frequency $\nu_{\text{s}}(\text{CF}_2)$ bands at 1124 cm^{-1} and 1191 cm^{-1} resulting in an absorbance maximum close to 1220 cm^{-1} . As the thickness of the polymer layer decreases the intensity of the s-polarized electric field of the evanescent wave

changes only slightly. However, as the thickness of the polymer film decreases, the intensity of the p-polarized electric field increases dramatically. As a result, there is an increase of surface normal mode intensities and an apparent shift in the region of maximum absorbance to higher frequencies in the 1200 cm^{-1} to 1250 cm^{-1} region as the thickness of the polymer layer decreases.

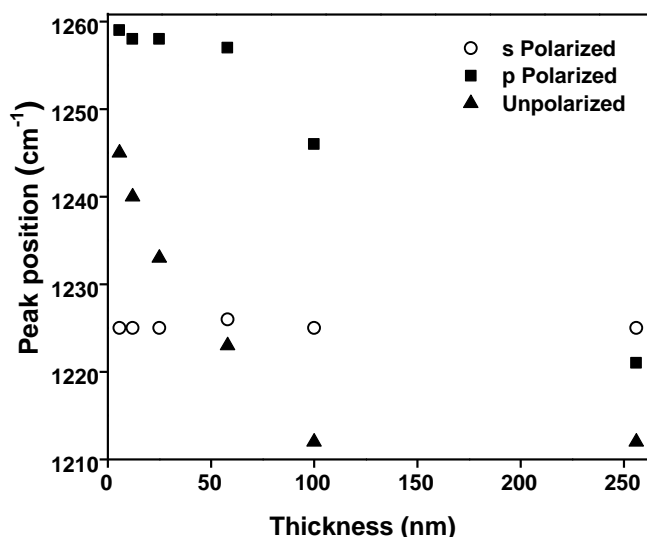


Figure 4-3. Position of $\text{CF}_2/\text{SO}_3^-$ peak maximum as a function of film thickness for grazing angle ATR with s-polarized, p-polarized, and unpolarized light.

In addition to the strength of the evanescent wave, the peak maxima changes observed in Figure 4-3 are also a result of surface orientation of NAFION molecules being observed under p-polarized IR conditions. Some literature discusses threshold thickness (40-70 nm) of the physical properties in NAFION thin films. Paul et al. have suggested that at approximately 55 nm thin NAFION films while still distinct from bulk membranes exhibit more bulk like properties. A glance at figure 4-3 shows that above 50 nm the unpolarized peak position corresponds to bulk isotropic films which could be interpreted as evidence for a morphological transition at this thickness as reported in the literature. While the morphological change is a likely factor in the peak position the changes in contribution of the x component in the unpolarized beam cannot be ruled out.

In free-standing membranes there is effectively a random orientation of molecules throughout the ATR penetration depth and there was no peak shift when polarization was changed for the ATR spectrum of bulk films as shown in Figure 4-4.

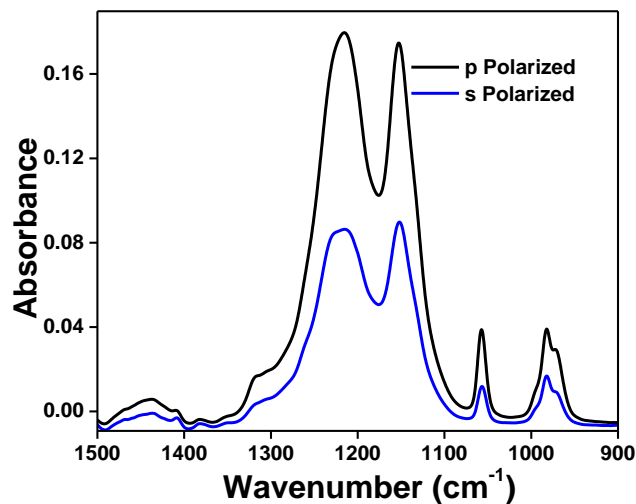


Figure 4-4. S and p-polarized ATR spectra of bulk NAFION film in grazing angle ATR geometry.

As a result, the spectra for both s and p-polarization differ only in intensity due to the lower s component intensity. In a thick film, on the order of 100 nm or more, ordered molecules may be confined to the interface between the substrate and the film. These surface-ordered molecules however compose far less of the film than the randomly oriented molecules in the bulk of the sample that is probed in SO-ATR geometry resulting in little increase of high frequency band intensity. As a result, the region of maximum absorbance shifts to higher frequencies by only slightly ($\sim 3 \text{ cm}^{-1}$) at 1220 cm^{-1} for a 250 nm thick sample, Figure 4-5.

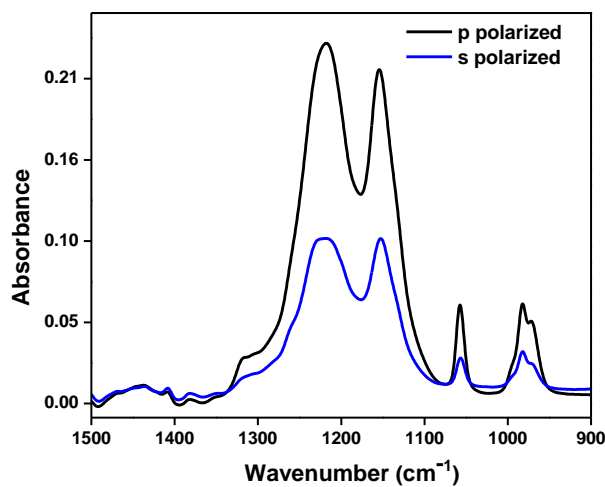


Figure 4-5. NAFION film, 250 nm thick, on silicon substrate s-polarized and p-polarized in SO-ATR geometry.

When a thick film is confined to a substrate in SO-ATR, the peak positions do not change and the peak shapes are similar to those observed in bulk film ATR for s and p-polarization, Figure 4-5. However the ratio of p to s intensity increases significantly in the SO-ATR spectrum, Figure 4-5, compared to the ATR spectrum, Figure 4-4, which is consistent with enhancement of the p-polarized component of the evanescent wave over the s component. In SO-ATR where the NAFION film is spun cast onto a substrate before the experiment, ordering occurs at the polymer substrate interface, but the bulk of the film remains randomly oriented resulting in similar spectra for spun cast thick films in the SO-ATR geometry and for a traditional ATR experiment of a bulk membrane. The strength of the evanescent wave decays exponentially as the distance from the crystal/polymer interface increases.³² When the polymer is thicker than 100 nm, unordered molecules close to the crystal/NAFION interface experience a stronger electric field than the ordered molecules at the polymer/substrate interface, hence ordering at substrate surface is not apparent from the SO-ATR spectrum. This lack of sensitivity for surface molecules in thick films is evidenced by the similarity of the peak shapes of p-polarized spectra of isotropic bulk

membranes, Figure 4-4, to these thick films, Figure 4-5, even when the films are thinner than the penetration depth.

As the thickness of the film decreases, the relative amount of surface ordered molecules increases resulting in an increase in the molecules contributing surface normal $\nu_{as}(\text{CF}_2)$ and $\nu_s(\text{SO}_3^-)$ dipoles. As a result, the peak maxima shift closer to frequencies characteristic to these bands under p-polarization, and remain close to the bulk film peak position under s-polarization. This shift in peak position represents a change of from 1225 cm^{-1} to 1256 cm^{-1} for a 50 nm sample as displayed in Figure 4-6. The peak shift between s and p-polarized spectra of a sample with thickness less than the penetration depth also confirms that the observed shifts are not a result of energy changes of functional groups but rather the orientation of those functional groups on the surface.

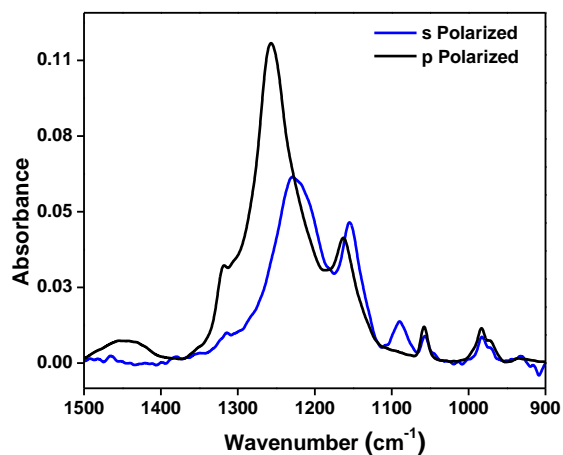


Figure 4-6. NAFION film, 50 nm thick, on silicon substrate s-polarized and p-polarized in SO-ATR geometry.

Figure 4-6 demonstrates that when the thickness decreases of a film confined to the substrate, the p-polarized spectrum exhibits an increase in absorbance relative to the s-polarized spectrum. A noticeable shift is observed in the peak between 1220 cm^{-1} and 1260 cm^{-1} which contains overlapping $-\text{CF}_2$, $-\text{CF}_3$ and $-\text{SO}_3^-$ symmetric and asymmetric stretch bands. A similar shift is

observed in the peak at 1150 cm^{-1} which contains overlapping for the $-\text{CF}_2$ symmetric and asymmetric stretch bands. These changes in peak shape indicate that the observed absorbance maximum of a peak being a result of a change in contributions of individual vibrational modes to the overall peak as discussed above rather than a change in bond strengths. The new peak at around 1100 cm^{-1} is an artifact from the Si-O-Si vibration of the silicon substrate native oxide layer which is in the plane of the silicon wafer and hence appreciable under s-polarization.

The effect of film thickness on the resulting spectra from increased polarization is more apparent when unpolarized spectra for thin and thick films are compared, as displayed in Figure 4-7. Thin films with thicknesses of less than 25 nm have peak positions similar to p-polarized spectra while thick films have peak positions similar to s-polarized spectra or spectra of unconfined isotropic films. The unpolarized peak shapes for thin films also resemble p-polarized spectra. The changing magnitude of the peak shift may be a result of the increased intensity of the electric field experienced by ordered molecules at the NAFION/substrate interface.

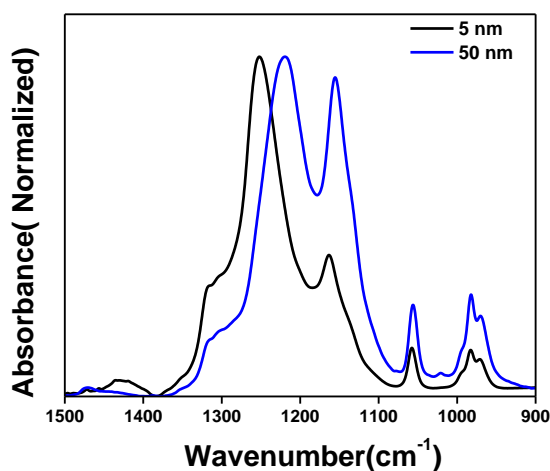


Figure 4-7. Unpolarized SO-ATR spectra of 5 nm and 50 nm thick NAFION on a silicon substrate.

The hypothesis that thin ordered films experience mostly p-polarized radiation in unpolarized SO-ATR experiments was confirmed by performing reflection and transmission experiments on thin films with thicknesses less than 25 nm thick under p-polarization. The peak shapes and positions observed in both reflection and transmission are consistent with the spectra observed in SO-ATR geometry, Figure 4-8. The peaks of the unpolarized SO-ATR spectrum on a gold substrate in Figure 4-8b appear broader than p-polarized reflection spectra because the absence of a polarizer in SO-ATR results in a higher proportion of the s-polarized component of the electric field.

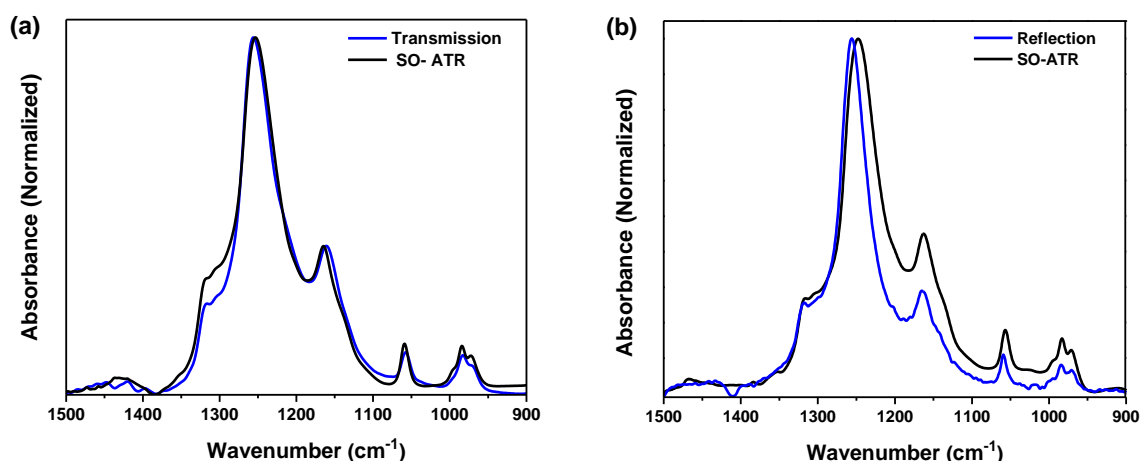


Figure 4-8. SO-ATR spectra compared to a) transmission for a 10 nm film on a silicon substrate and b) reflection for a 5 nm film on a gold substrate.

The precise vibrational modes that are enhanced under p-polarization are key to understanding which functional groups interact with the substrate. Bands corresponding to the asymmetric C-F stretches of the $-\text{CF}_2$ and $-\text{CF}_3$ groups are enhanced. These bands appear in the 1100 cm^{-1} to 1260 cm^{-1} range and are at higher the corresponding symmetric stretch bands. It is interesting to note that peaks below 1100 cm^{-1} such as the $\nu_s(\text{SO}_3^-)$ band at 1056 cm^{-1} do not shift with changing polarization. NAFION adsorbs on silicon oxide via the sulfonate groups resulting in ordering of the backbone in such a manner that the backbone $\nu_{\text{as}}(\text{CF}_2)$ stretch is predominantly aligned to the p-polarized electric field as displayed in Figure 4-9.

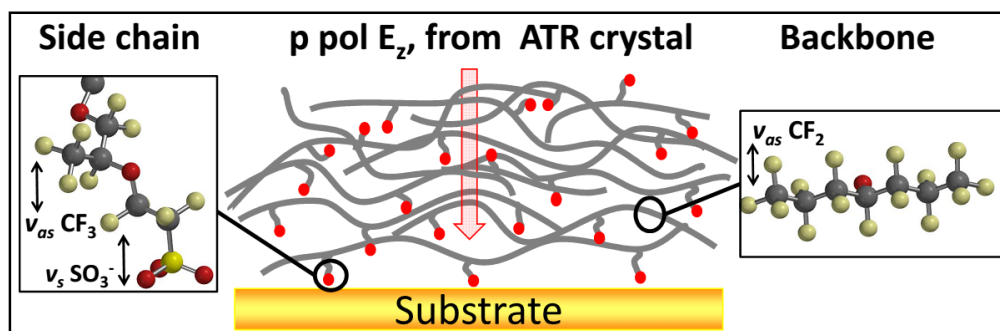


Figure 4-9. Ordered conformation of NAFION on surface for thin films where the backbone $\nu_{as}(\text{CF}_2)$, side chain $\nu_s(\text{SO}_3^-)$ and $\nu_{as}(\text{CF}_3)$ dipole changes are in the plane of the p-polarized z component of the evanescent wave.

In SO-ATR, the increased absorbance of the 1220 cm^{-1} band as p-polarization increases suggests $-\text{CF}_2$ groups become locked in a conformation where the $\nu_{as}(\text{CF}_2)$ dipole is in the plane of the p-polarized electric field which is consistent with the observations of Kendrick, et al. in PM-IRRAS experiments. Computational studies on optimized structures of the NAFION sidechain and model perfluorosulfonic compounds puts the $-\text{CF}_3$ groups with the C3 axis parallel to the surface when the side chain $-\text{SO}_3^-$ groups are in the geometry required for adsorption.^{28,38} This orientation is limited only to polymer chains in close proximity to the surface, with a decrease in order as the film thickness increases. It is most likely that the $-\text{CF}_3$ group is oriented with the C3 axis parallel to the surface as this puts the asymmetric stretch perpendicular to the surface which explains the dominance of the $-\text{CF}_3$ band at 1256 cm^{-1} . This proposed orientation of $-\text{CF}_3$ groups can be rationalized by considering a model molecule with C_{3v} symmetry such as the $-\text{SO}_3^-$ and $-\text{CF}_3$ groups in NAFION. For a C_{3v} molecule oriented on a surface as shown in Figure 4-10, the dipole changes for the symmetric stretch are in the z plane perpendicular to the substrate resulting in strong absorbance in p-polarized light. On the other hand, the asymmetric stretch dipole changes are in the x and y planes resulting in strong s-polarized absorbance. As the strong absorbance at 1256 cm^{-1}

¹ suggests an enhancement of the $\nu_{\text{as}}(\text{CF}_3)$ band it is reasonable to conclude that the $-\text{CF}_3$ group is oriented with its C3 axis perpendicular to the surface and plays no part in adsorption to the surface.

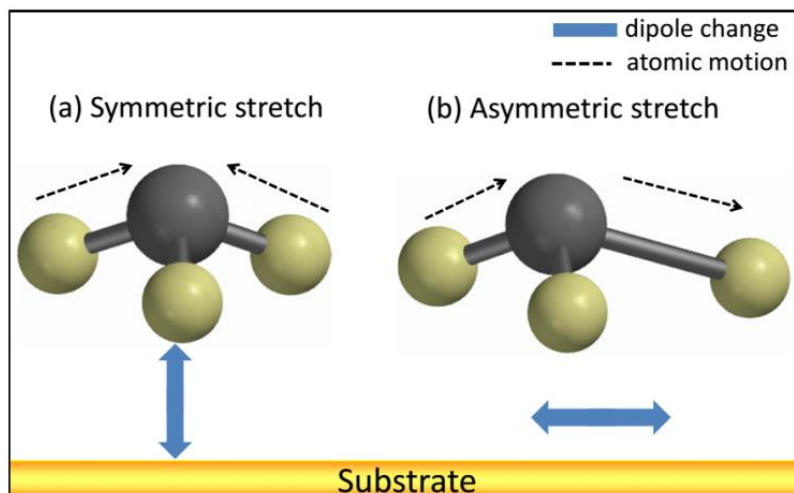


Figure 4-10. Orientation of dipole changes relative to the surface for a molecule with C_{3v} symmetry undergoing a) a symmetric stretch and b) an asymmetric stretch.

4.4 Conclusions

In determining the orientation of ionomer thin films on substrates such as silicon and gold, the thickness of the film and the SO-ATR geometry significantly influences the polarization of the evanescent wave. As the film thickness decreases, the z component of wave which contributes to p-polarization of the radiation is enhanced resulting p-polarization enhancement. This change in polarization results in spectral changes due to enhanced absorbances of oriented dipoles normal to the substrate. NAFION is oriented at the substrate-polymer film interface resulting in higher absorbance values with p-polarized light. NAFION is likely to associate with surfaces via the $-\text{SO}_3^-$ groups causing a reduction in backbone motion and alignment of the backbone parallel to the surface with backbone $\nu_{\text{as}}(\text{CF}_2)$ dipole changes perpendicular to the surface. Side chain ordering results in $\nu_{\text{as}}(\text{CF}_3)$ dipole changes being aligned perpendicular to the surface. The overall changes in absorbance maximum of the 1220 cm^{-1} and 1140 cm^{-1} peaks results from increased absorbance

of the $-\text{CF}_2$, and $-\text{CF}_3$ asymmetric stretch bands and a decreased absorbance of the $-\text{CF}_2$ and $-\text{CF}_3$ symmetric stretch bands. The enhancement of high frequency bands is most pronounced for very thin films where the evanescent wave is the most intense and most p-polarized in character.

4.5 Supplementary Information

Figure 4-11 below is analogous to figure 3-4 in chapter 3 and shows the relative y and z-component electric field strength. The p factors are calculated from equations 3-11 to 3-15 using parameters in table 3-1. The x-component field strength is typically very close to that of the y component and is not shown for clarity. As shown the z-component is significantly enhanced for SO-ATR but not in ATR.

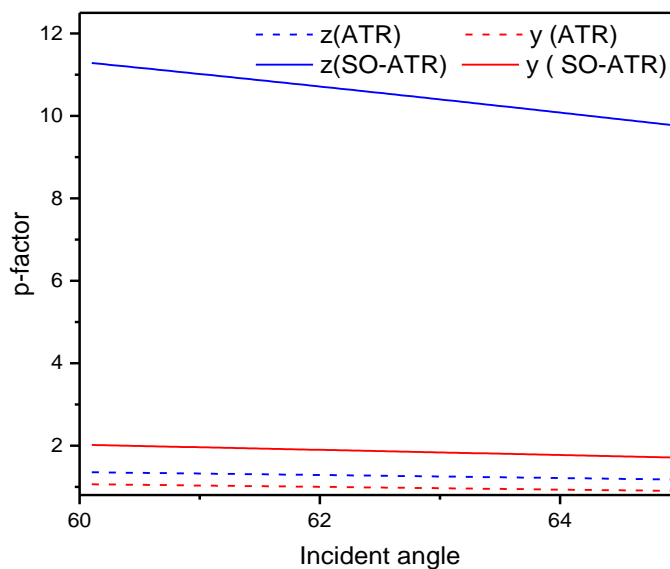


Figure 4-11. P-factors calculated for a 50 nm NAFION film in SO-ATR (solid lines) and ATR geometry (dashed lines).

Figure 4-12 shows conventional ATR Spectrum of a several hundred nanometer thick film directly spin cast on to a Silicon hemisphere. The penetration depth under different polarizations was calculated using Harrick expressions.³⁹ Figure 4-12 shows that there are subtle differences between s and p polarized spectra as a function of penetration depth but these differences are not sufficient to draw any conclusions about the ordering of NAFION on Silicon.

$$d_{\perp} = \frac{n_1^2 n_2 \cos \theta}{(n_1^2 - n_2^2)} \cdot \frac{\lambda}{\pi \sqrt{n_1^2 \sin^2 \theta - n_2^2}} \quad (4-2)$$

$$d_{\parallel} = \frac{n_1^2 n_2 \cos \theta}{(n_1^2 - n_2^2)} \cdot \frac{\lambda}{\pi \sqrt{n_1^2 \sin^2 \theta - n_2^2}} \cdot \frac{2n_1^2 \sin^2 \theta - n_2^2}{(n_1^2 - n_2^2) \sin^2 \theta - n_2^2} \quad (4-3)$$

Where n_1 is the crystal refractive index and n_2 is the sample refractive index and θ is the incident angle. The penetration depth at each polarization is given in table 4-3, where d_e is the effective penetration depth and is the average of the penetration depth in s and p polarizations.

Table 4-3. Penetration depth for ATR calculated at 1250 cm^{-1} under s and p-polarization in ATR on a silicon hemisphere

Incident angle	30	60	80
$d_{\perp} \text{ (nm)}$	350	79	23
$d_{\parallel} \text{ (nm)}$	2380	225	64
$d_e \text{ (nm)}$	1365	152	44

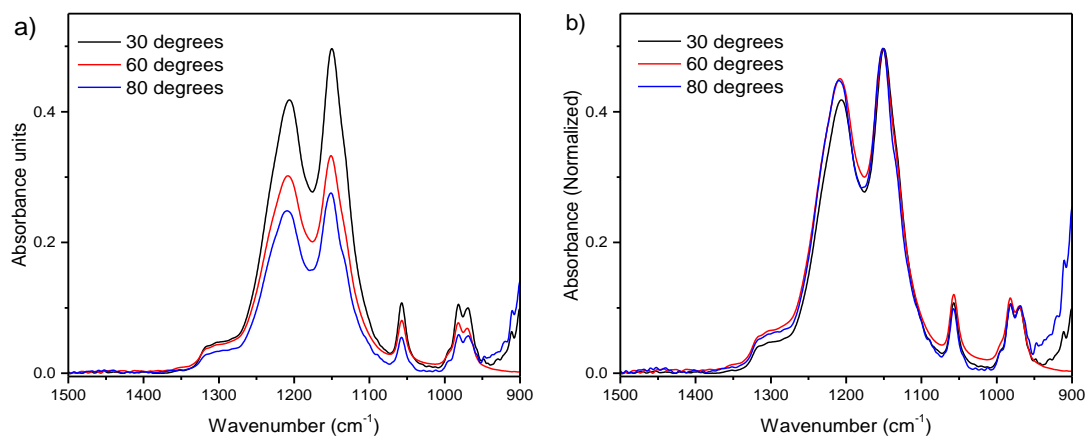


Figure 4-12. p polarized ATR spectra of a 500 nm NAFION film spin cast directly onto a hemispherical silicon ATR crystal.

While we observed peak shifts when NAFION was directly cast onto a silicon hemisphere, these shifts were not as pronounced as observed in SO-ATR. As shown in figure 4-13 these peak shifts were slight and more pronounced when a 50 nm film was probed.

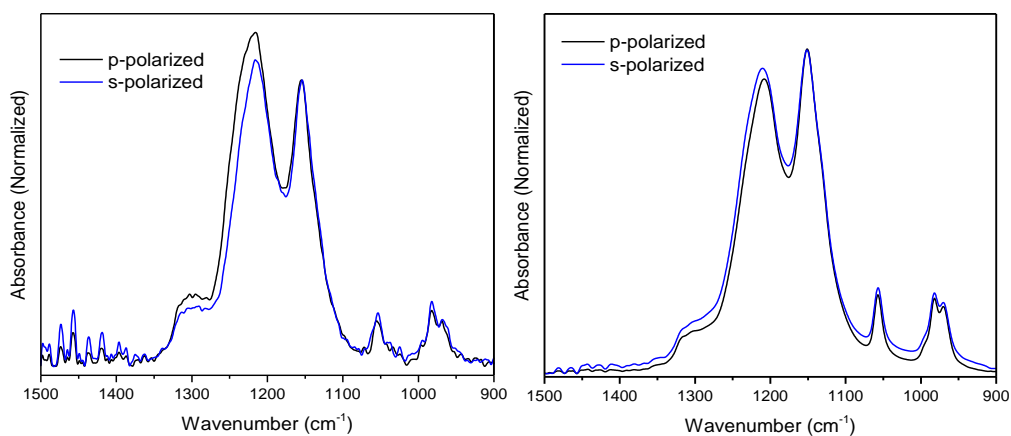


Figure 4-13. s and p-polarized spectra of a) a 50 nm and b) a 500 nm NAFION film spin cast directly onto a silicon hemisphere. All spectra were collected at 65° incident angle.

A comparison the p-polarized of a 500 nm and a 50 nm thick films results a shift similar to that observed in SO-ATR and displayed in figure 4-7 in the results and discussion section. The shift in this case is much subtler with the peak position in this case shifting from 1211 cm^{-1} to 1217 cm^{-1} . For a 50 nm film in SO-ATR this peak is observed at 1256 cm^{-1} .

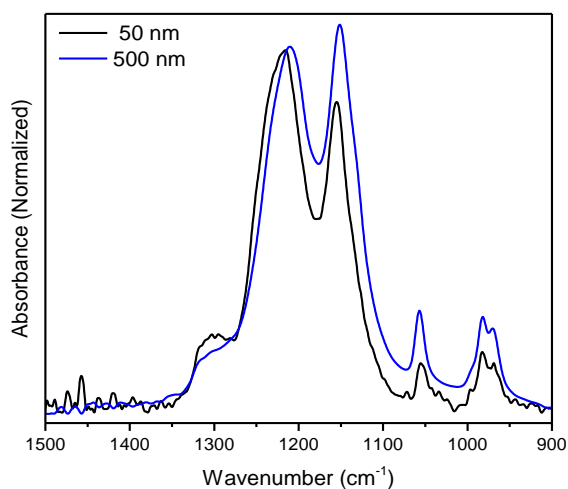


Figure 4-14. P-Polarized spectra of 500nm and 50 nm thick films overlaid.

4.6 References

- (1) Yamato, T.; Hideshima, C.; Prakash, G. K. S.; Olah, G. A. Solid Superacid-Catalyzed Organic Synthesis. 4. Perfluorinated Resinsulfonic Acid (NAFION-H) Catalyzed Friedel-Crafts Benzylolation of Benzene and Substituted Benzenes. *J. Org. Chem.* **1991**, *56* (6), 2089.
- (2) van der Wal, P. D.; de Rooij, N. F.; Koudelka-Hep, M. Extremely Stable NAFION Based Carbon Monoxide Sensor. *Sensors Actuators B Chem.* **1996**, *35* (1–3), 119.
- (3) Hickner, M. A. Ion-Containing Polymers: New Energy & Clean Water. *Mater. Today* **2010**, *13* (5), 34.
- (4) Modestino, M. A.; Walczak, K. A.; Berger, A.; Evans, C. M.; Haussener, S.; Koval, C.; Newman, J. S.; Ager, J. W.; Segalman, R. A. Robust Production of Purified H₂ in a Stable, Self-Regulating, and Continuously Operating Solar Fuel Generator. *Energy Environ. Sci.* **2014**, *7* (1), 297.
- (5) Xi, J.; Wu, Z.; Qiu, X.; Chen, L. NAFION/SiO₂ Hybrid Membrane for Vanadium Redox Flow Battery. *J. Power Sources* **2007**, *166* (2), 531.
- (6) Smitha, B.; Sridhar, S.; Khan, A. A. Solid Polymer Electrolyte Membranes for Fuel Cell Applications—a Review. *J. Memb. Sci.* **2005**, *259* (1–2), 10.
- (7) Kocha, S. S.; Zack, J. W. J.; Alia, S. M. S.; Neyerlin, K. C.; Pivovar, B. S. Influence of Ink Composition on the Electrochemical Properties of Pt/C Electrocatalysts. *ECS Trans.* **2013**, *50* (2), 1475.
- (8) Tripkovic, D. V.; Strmcnik, D.; van der Vliet, D.; Stamenkovic, V.; Markovic, N. M. The

Role of Anions in Surface Electrochemistry. *Faraday Discuss.* **2008**, *140* (0), 25.

- (9) Villegas, I.; Weaver, M. J. Carbon Monoxide Adlayer Structures on Platinum (111) Electrodes: A Synergy between In-situ Scanning Tunneling Microscopy and Infrared Spectroscopy. *J. Chem. Phys.* **1994**, *101* (2), 1648.
- (10) Faguy, P. W.; Marinković, N. S.; Adžić, R. R.; Marinković, N. S.; Adair, R. R. Infrared Spectroscopic Analysis of Anions Adsorbed from Bisulfate-Containing Solutions on Pt(111) Electrodes. *J. Electroanal. Chem.* **1996**, *407* (1–2), 209.
- (11) Faguy, P. W.; Marinković, N. S.; Adžić, R. R. An in Situ Infrared Study on the Effect of pH on Anion Adsorption at Pt(111) Electrodes from Acid Sulfate Solutions. *Langmuir* **1996**, *12* (2), 243.
- (12) Yeh, K.-Y.; Restaino, N. a.; Esopi, M. R.; Maranas, J. K.; Janik, M. J. The Adsorption of Bisulfate and Sulfate Anions over a Pt(111) Electrode: A First Principle Study of Adsorption Configurations, Vibrational Frequencies and Linear Sweep Voltammogram Simulations. *Catal. Today* **2013**, *202* (0), 20.
- (13) Bass, M.; Berman, A.; Singh, A.; Konovalov, O.; Freger, V. Surface-Induced Micelle Orientation in NAFION Films. *Macromolecules* **2011**, *44* (8), 2893.
- (14) Modestino, M. A.; Paul, D. K.; Dishari, S.; Petrina, S. A.; Allen, F. I.; Hickner, M. A.; Karan, K.; Segalman, R. A.; Weber, A. Z. Self-Assembly and Transport Limitations in Confined NAFION Films. *Macromolecules* **2013**, *46* (3), 867.
- (15) Eastman, S. A.; Kim, S.; Page, K. A.; Rowe, B. W.; Kang, S.; Soles, C. L.; Yager, K. G. Effect of Confinement on Structure, Water Solubility, and Water Transport in NAFION

Thin Films. *Macromolecules* **2012**, *45* (19), 7920.

- (16) Kendrick, I.; Kumari, D.; Yakaboski, A.; Dimakis, N.; Smotkin, E. S. Elucidating the Ionomer-Electrified Metal Interface. *J. Am. Chem. Soc.* **2010**, *132* (49), 17611.
- (17) Masuda, T.; Ikeda, K.; Uosaki, K. Potential-Dependent Adsorption/Desorption Behavior of Perfluorosulfonated Ionomer on a Gold Electrode Surface Studied by Cyclic Voltammetry, Electrochemical Quartz Microbalance, and Electrochemical Atomic Force Microscopy. *Langmuir* **2013**, *29* (7), 2420.
- (18) Masuda, T.; Fukumitsu, H.; Kondo, T.; Naohara, H.; Tamura, K.; Sakata, O.; Uosaki, K. Structure of Pt(111)/Ionomer Membrane Interface and Its Bias-Induced Change in Membrane Electrode Assembly. *J. Phys. Chem. C* **2013**, *117* (23), 12168.
- (19) Malevich, D.; Zamlynny, V.; Sun, S.-G.; Lipkowski, J. In Situ Infrared Reflection Absorption Spectroscopy Studies of the Interaction of NAFION with the Pt Electrode Surface. *Zeitschrift für Phys. Chemie/International J. Res. Phys. Chem. Chem. Phys.* **2003**, *217* (5/2003), 513.
- (20) Dishari, S. K.; Hickner, M. A. Antiplasticization and Water Uptake of NAFION Thin Films. *ACS Macro Lett.* **2012**, *1* (2), 291.
- (21) Paul, D. D. K.; Karan, K.; Docoslis, A.; Giorgi, J. B.; Pearce, J. Characteristics of Self-Assembled Ultrathin NAFION Films. *Macromolecules* **2013**, *46* (9), 3461.
- (22) Andanson, J.-M.; Baiker, A. Exploring Catalytic Solid/liquid Interfaces by in Situ Attenuated Total Reflection Infrared Spectroscopy. *Chem. Soc. Rev.* **2010**, *39* (12), 4571.

- (23) Tolstoy, V. P.; Chernyshova, I. V.; Skryshevsky, V. A. *Handbook of Infrared Spectroscopy of Ultrathin Films*; Wiley Interscience: New Jersey, 2003.
- (24) Milosevic, M.; Berets, S. L.; Corporation, H. S. Applications of the Theory of Optical Spectroscopy to Numerical Simulations. *Appl. Spectrosc.* **1993**, 47 (5), 566.
- (25) Everall, N. J.; Bibby, A. Improvements in the Use of Attenuated Total Reflection Fourier Transform Infrared Dichroism for Measuring Surface Orientation in Polymers. *Appl. Spectrosc.* **1997**, 51 (8), 1083.
- (26) Greenler, R. G. Infrared Study of Adsorbed Molecules on Metal Surfaces by Reflection Techniques. *J. Chem. Phys.* **1966**, 44 (1), 310.
- (27) Milosevic, M.; Milosevic, V.; Berets, S. L. Grazing Angle Attenuated Total Reflection Spectroscopy: Fields at the Interface and Source of the Enhancement. *Appl. Spectrosc.* **2007**, 61 (5), 530.
- (28) Danilczuk, M.; Lin, L.; Schlick, S.; Hamrock, S. J.; Schaberg, M. S. Understanding the Fingerprint Region in the Infra-Red Spectra of Perfluorinated Ionomer Membranes and Corresponding Model Compounds: Experiments and Theoretical Calculations. *J. Power Sources* **2011**, 196 (20), 8216.
- (29) Warren, D. S.; McQuillan, J. Infrared Spectroscopic and DFT Vibrational Mode Study of Perfluoro(2-Ethoxyethane) Sulfonic Acid (PES), a Model NAFION Side-Chain Molecule. *J. Phys. Chem. B* **2008**, 112 (34), 10535.
- (30) Schmatko, T.; Colombari, P.; Gruber, A.; Régis, A. Nanostructure of NAFION Membranes at Different States of Hydration: An IR and Raman Study. *Vib. Spectrosc.* **2001**, 26 (2), 215.

- (31) Korzeniewski, C.; Snow, D. E.; Basnayake, R. Transmission Infrared Spectroscopy as a Probe of NAFION Film Structure: Analysis of Spectral Regions Fundamental to Understanding Hydration Effects. *Appl. Spectrosc.* **2006**, *60* (6), 599.
- (32) Zeng, J.; Jean, D.; Ji, C.; Zou, S. In Situ Surface-Enhanced Raman Spectroscopic Studies of NAFION Adsorption on Au and Pt Electrodes. *Langmuir* **2011**, *28* (1), 957.
- (33) Albinsson, B.; Michl, J. Anti, Ortho, and Gauche Conformers of Perfluoro-N-Butane: Matrix-Isolation IR Spectra and Calculations. *J. Phys. Chem.* **1996**, *100* (9), 3418.
- (34) Yamaguchi, M.; Ohira, A. Vibrational Analysis of Side Chain Model Compounds of Perfluorinated Alkyl Sulfonic Acid Ionomers. *J. Phys. Chem. A* **2012**, *116* (44), 10850.
- (35) Di Noto, V.; Piga, M.; Lavina, S.; Negro, E.; Yoshida, K.; Ito, R.; Furukawa, T. Structure, Properties and Proton Conductivity of Nanocomposite Membranes. *Electrochim. Acta* **2010**, *55* (4), 1431.
- (36) Nagao, Y. Highly Oriented Sulfonic Acid Groups in a NAFION Thin Film on Si Substrate. *J. Phys. Chem. C* **2013**, *117* (7), 3294.
- (37) Aroca, R. *Surface-Enhanced Vibrational Spectroscopy*; John Wiley & Sons, Ltd: Chichester, UK, 2006.
- (38) Clark, J. K.; Paddison, S. J. Side Chain Flexibility in Perfluorosulfonic Acid Ionomers: An Ab Initio Study. *J. Phys. Chem. A* **2013**, *117* (40), 10534.
- (39) Harrick, N. J. *Internal Reflection Spectroscopy*; John Wiley & Sons: New York, 1967.

Chapter 5

Understanding The Fingerprint Region in The Infra-Red Spectra Of Aromatic Polyamides

5.1 Introduction

Aromatic polyamide systems have generated much interest due to their use in water treatment applications.^{1,2} In commercially available nano filtration (NF) and reverse osmosis (RO) membranes the polyamide (PA) layer is the active layer of a composite that is also comprised of a polysulfone porous support on a polyester fabric backing.^{3,4} Currently these thin film composite RO membranes are based on a PA thin-film made by interfacial polymerization of an aromatic polyamine such as m-phenylenediamine (MPD) with aromatic polyacyl halides such as trimesoyl chloride (TMC).^{5,6} Detailed information on the nanostructure of PA active layer is required to achieve a better understanding of salt rejection and water transport in RO and NF films. Xie et al demonstrated that the performance of these membranes is highly sensitive to preparation conditions such as monomer concentration or support membrane wetting protocol.⁷ As a result, there is wide variability between salt rejection and flux values reported in literature. It is with this in mind that Johnson et al developed a molecular layer by layer deposition protocol for the synthesis of aromatic polyamide films supported on planar substrates.⁸ mLbL films the film chemistry and kinetics of polymerization to be precisely controlled which directly relates to a more homogenous structure.^{9,10}

Studies on aliphatic polyamide systems such as nylons have demonstrated that FTIR can provide crucial information about structural changes¹¹, chemical composition¹² and orientation^{13,14} provided that appropriate peaks are identified and the vibrational modes that contribute to those peaks are understood.^{12,14} The use of vibrational spectroscopy in the analysis of these membranes has proved

particularly useful in analyzing parameters such as the degradation of these membranes, the hydrogen bonding during film hydration and the effect of altering film coatings.¹⁵⁻¹⁷ Tang et al used ATR-FTIR and X-ray photoelectric spectroscopy to characterize 17 commercial thin film composite polyamide membranes and assigned several peaks for both fully aromatic and partially aromatic systems.¹⁸ Tang et al assigned the 1663 cm^{-1} peak to the $\nu(\text{C}=\text{O})$ dominated Amide I vibration. They also proposed that the 1609 cm^{-1} peak in a TMC-MPD system was either the N-H deformation or the C=C ring vibration based on the peaks disappearance of the peak when aromatic MPD is replaced by piperazinamide. Kang et al used ATR to study the degradation of aromatic polyamide membranes by hypochlorite attack under different PH conditions.¹⁹ In this study the peak at 1610 cm^{-1} was assigned to hydrogen-bonded carbonyl of the amide I vibration in contrast to the assignment of the same peak to either aromatic C=C or amide N-H by Tang et al. Based on this assignment Kang attributed the disappearance of this peak to a reduction in hydrogen bonding and large shift of the peak position resulting in it merging with other peaks in the fingerprint region. In a similar study of hypochlorite degradation Kwon and Leckie¹⁵ attributed the disappearance of the same peak to direct chlorination of the aromatic rings. The contradicting interpretations of this peaks behavior upon hypochlorite attack demonstrated the importance of understanding the fingerprint region in elucidating the degradation and hydrogen bonding in these crosslinked membranes.

The physical phenomena that control the structure and dynamics of water confined in a polyamide RO and NF membranes are not yet fully understood despite years of research in this field.⁵ FTIR has been successfully used to characterize the water-polymer interactions in a range of polymer systems²⁰⁻²² and can be used to address the dearth of information in RO membrane water dynamics. The usefulness of FTIR in studying water dynamics is contingent on understanding how and which vibrational modes are affected by hydrogen bonding. In the case of aromatic polyamides some researchers have chosen the amide I vibrations and amide II peaks to

probe hydrogen bonding.²³ The use of the amide I peak is complicated by the overlap of free acid C=O bands in this region, furthermore, possible overlap of the amide II band with aromatic ring modes is often overlooked.

The infrared spectrum of aromatic polyamides is unsurprisingly dominated by the various vibrational modes of substituted benzene rings. The tangential carbon-carbon stretching vibrations known as vibrations 8 and 19 in the Varsanyi nomenclature²⁴ are prominent in the 1000 cm⁻¹ to 1800 cm⁻¹ frequency range where amide vibrations occur. The changes in the spectral features of aromatic rings upon changing the identity, number and position of substitution have been studied for decades and are well understood.^{25,26} Recently Mahalakshmi and Balachandran studied the molecular structure, conformational stability, geometry optimization and vibrational frequencies of TMC and determined that the benzene ring possess six ring vibrations in the frequency ranges 1460 cm⁻¹ to 1660 cm⁻¹ and 1070 cm⁻¹ to 1150 cm⁻¹.²⁷

Peak assignments of bands related to amide linkages and aromatic rings in the poly(amide) system should be straightforward given the wealth of literature on the vibrational modes of these functional groups. However, the situation is complicated by significant band overlap in the fingerprint region from 1000 cm⁻¹ to 1800 cm⁻¹ and hence deconvolution of the spectra to quantify the composition of the material is not trivial.

In this Study we report the FTIR peak assignments for this system on the basis of an extensive literature search, density functional theory (DFT) calculations, and experiments using reflection-absorption infrared spectroscopy (RAIRS), attenuated total reflectance (ATR) and transmission. We used mLbL synthesized membranes as a model system as they provide an additive free relatively reproducible sample set of controllable thickness. We draw comparisons with interfacially polymerized films and demonstrate how specific peaks can be used in RO membrane research.

5.2 Methods

Samples for transmission experiments were prepared from additive free Dow commercial membranes BWXE for the TMC-MPD system. The composite membrane was delaminated to remove the polyester backing and the polysulfone layer dissolved to isolate the Polyamide membrane using the method published by fregger.²⁸ In brief the delaminated composite membrane placed PA surface down on the substrate with a drop of Methanol to promote adhesion. Drops of DMF were applied the immobilized membrane using a pipette for 15 minutes thereby dissolving a washing off the Polysulfone support. The Resulting film was soaked in an excess of DMF for 72 hours to remove any residual polysulfone before being rinsed by water followed by methanol. The removal of polysulfone was confirmed spectrally (fig 5-15, supporting information) by the absence of characteristic polysulfone peaks below 1300 cm^{-1} .

RAIRS and ATR experiments were performed as explained in chapter 3. Samples on gold substrates for RAIRS and silicon substrates for ATR were prepared by layer by layer deposition directly on the substrate as described in chapter 3⁸. PM-IRRAS experiments were performed on a Nicolet 6700 (Thermo Electron Scientific Instrument Corp., Beverly, MA) equipped with an external MCT detector and humidity cell with ZnSe windows. Polarization modulation (PM) in this instrument was provided by a Hinds Instruments (Hillsboro, OR) PM-90 with a 50 kHz ZnSe optical head and a synchronous sampling demodulator (GWC Instruments, Madison, WI). Reference spectra were acquired on bare gold plated silicon wafers

The effective incident angle of the IR beam on the sample was fixed at 72° and 1500 scans collected at a mirror velocity of 1.2 cm s^{-1} and resolution of 6 cm^{-1} . Controlled humidified air (RH) was generated for PM-IRRAS experiments by mixing humidified air at dew point with dry air at ambient temperature. Humid air at dew point was produced by sparging air in a water reservoir held in a heated water bath at 30°C . The total flow rate of dry air regulated at a constant flow rate

using electronic mass flow controllers (FMA 5514, Omega Engineering, Stamford, CT) and a custom LabVIEW (National Instruments Corp., Austin, TX) program. Humidity and temperature were measured and recorded using an Omega HX15-W RH probe (Omega Engineering, Stamford, CT). the humidity was held constant for 20 mins to allow equilibration before spectral collection. Transmission experiments were carried out in a cell described in a previous publication²⁹ with the humidity controlled in the same fashion as for PM-IRRAS. For transmission experiments spectra were collected every 45 seconds for 20 minutes.

The Vibrational spectra of a small polymer fragment (figure 5-1) was calculated in the gas phase. The optimal geometries and the Cartesian force fields for all the considered fragments were calculated at the DFT/B3LYP level with the 6-31++G** basis set. This approach was shown to provide very accurate multiparameter-scaled frequencies.³⁰ A scaling factor of 0.9062 was applied to account for the overestimation of vibrational frequencies and the resultant intensities normalized to the experimental ring mode intensity.

X-ray photoelectron spectroscopy (XPS) was performed on a Kratos AXIS Ultra DLD spectrometer with a monochromated Al K α source operating at 1486.6 eV and 140 W. The base pressure of the sample analysis chamber was ca. 2.0×10^{-9} Pa, and spectra were collected from a nominal spot size of $300 \mu\text{m} \times 700 \mu\text{m}$. Measurements were performed in hybrid mode using electrostatic and magnetic lenses. Survey scans were performed over a binding energy window of (1200 to 0) eV, with the pass energy of the analyzer set at 160 eV and an energy resolution of 0.5 eV. High-resolution scans were performed on each element of interest, with the pass energy of the analyzer set at 20 eV and an energy resolution of 0.1 eV. Generally, total acquisition times of 440 s and 180 s were used to obtain survey and high-resolution spectra, respectively. For a 0° take off angle the maximum information depth of the measurements was approximately 8–10 nm. Binding energies were calibrated with respect to C 1s (C-C bond) at 285.0 eV.

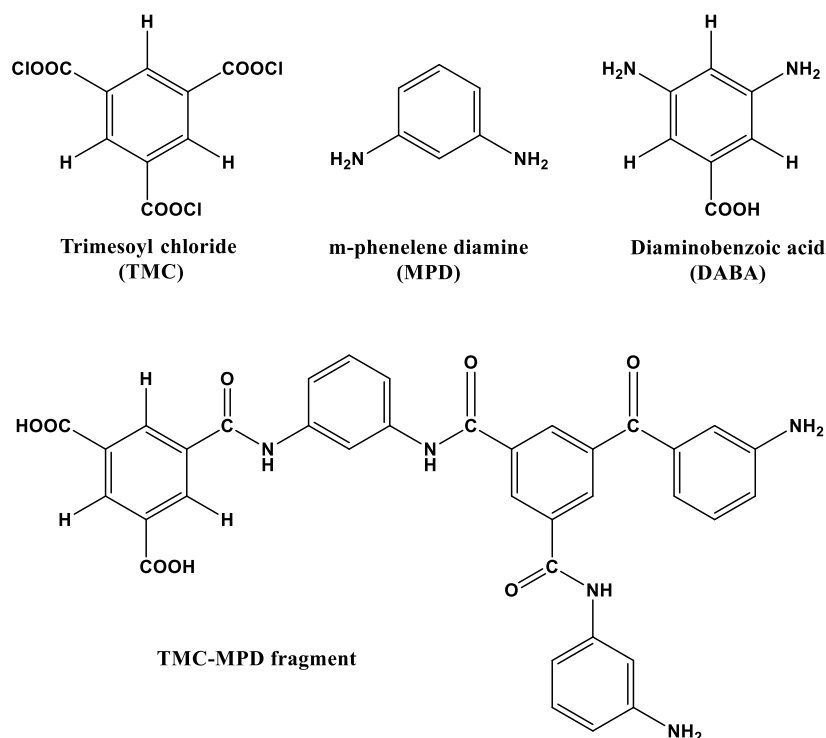


Figure 5-1. Chemical structures of monomers used in synthesis of mLbL films and the TMC-MPD fragment used in DFT calculations.

5.3 Results and Discussion

5.3.1 Fingerprint region peak assignment

DFT calculations of the vibrational spectrum of a small molecule with chemistry representative of the polymer were performed to aid in identifying the vibrational modes that contribute to the peaks observed in the polyamide fingerprint region. While this method of calculating vibrational modes neglects interactions such as hydrogen bonding and may not correctly estimate coupling of vibrational modes it is advantageous as it optimized the use of computational resources. Additionally several researchers^{31,32} have proved that fragment approximation methods yield very accurate predictions of atomic displacements and vibrational activities for

macromolecules including protein polyamides.³³ After scaling a close agreement was observed between the experimentally known positions of the Amide I $\nu(\text{C}=\text{O})$, the aromatic $\nu(\text{C}=\text{C})$ vibration and the Amide II $\delta(\text{N}-\text{H})$ with the computed mode positions hence computed mode positions could confidently be used to assign peak experimental peaks. The intensity of the computed fragment spectrum was scaled to the aromatic $\nu(\text{C}=\text{C})$ peak at 1610 cm^{-1} . This peak was selected arbitrarily and the $\nu(\text{C}=\text{O})$ or $\delta(\text{N}-\text{H})$ could equally have been used however we elected not to normalize each mode in the computational spectrum in order to preserve the calculated intensity ratios. As a result, several of the normalized intensities presented in Figure 5-2a are either over-estimated or underestimated relative to the experimental spectrum. Detailed below are the peak assignments for this system divided into 3 regions (I, II, and III) for clarity as shown in Figure 5-2b. The polymer aromatic ring originating from TMC will be referred to as ring A and the ring originating from MPD will be referred to as ring B to prevent confusion with monomer aromatic rings.

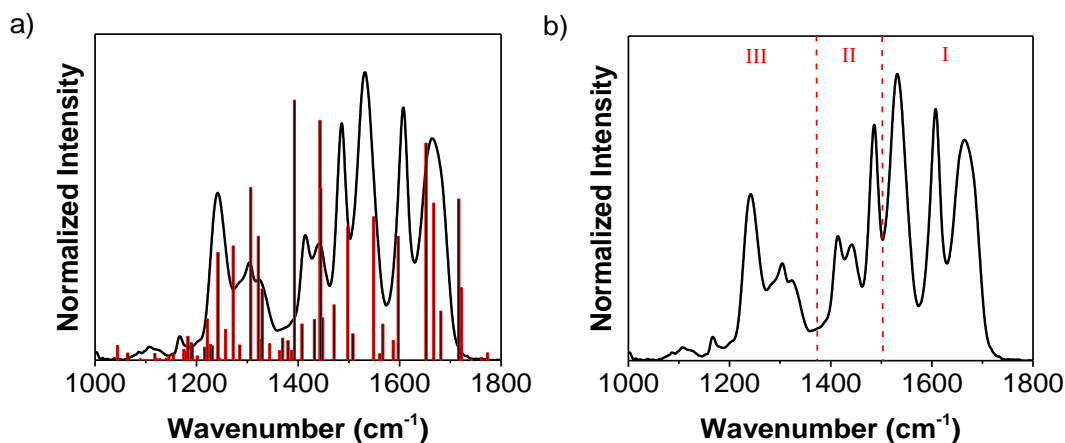


Figure 5-2. RAIRS spectrum of 60 cycle LBL PA film on gold showing the fingerprint region from 1000 cm^{-1} to 1800 cm^{-1} showing the three regions of peak deconvolution.

In the interest of brevity, a brief discussion of the normal vibrations of TMC and MPD rings relevant to our peak assignment will be presented in the supporting information section.

5.4.1.1 Region I

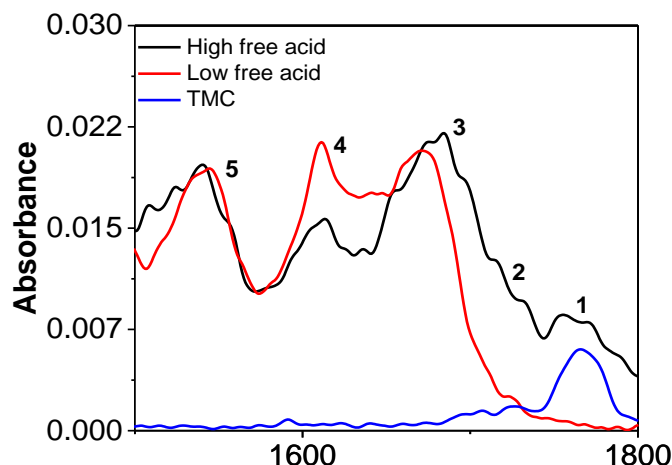


Figure 5-3. Low cycle number spectra overlayed with TMC spin cast on a gold substrate showing the peak position of free acid COO^- groups. The peak numbers correspond to the numbers in the body of the text.

This is perhaps the most studied region in the polyamide system due to the prominent Amide I peak at 1612 cm^{-1} and Amide II peak at 1546 cm^{-1} . The Amide I peak is a combination of the amide $\text{C}=\text{O}$ stretch at 1672 cm^{-1} coupled with a $\text{C}-\text{C}-\text{N}$ deformation and $\text{C}-\text{N}$ stretch. As the amount of unreacted end groups in the system increase a shoulder at 1718 cm^{-1} becomes apparent. This peak will appear when unreacted trimesoyl chloride monomer undergoes nucleophilic addition in the presence of water forming a carboxylic acid, yielding a membrane with appreciable acidic character. This shoulder can be ascribed to the $\text{C}=\text{O}$ stretch from the carboxyl group on the ring A. In pure liquid phase TMC monomer the $\text{C}=\text{O}$ stretch occurs at 1760 cm^{-1} as shown in figure 5-3 and Figure 5-12 in the supporting information when all the acid groups exist in the $-\text{COOCl}$ form. By using mLbL samples on gold where it is possible to add each monomer successively we can clearly observe the TMC $\text{C}=\text{O}$ peak at 1760 cm^{-1} with a broad low frequency shoulder between 1671 cm^{-1} and 1750 cm^{-1} , Figure 5- 3. We believe that at 0.5 cycles TMC exists in its un-hydrolyzed

(-COOCl) form and the hydrolyzed trimesic acid form (-COOH). This would explain the high frequency of the free acid peak in low cycle number samples where the free acid peak appears at 1760 cm^{-1} as shown by peak 1 in Figure 5-3. When the sample has very little free acid this peak now appears close to the DFT has a position and is now observed as a shoulder at 1718 cm^{-1} which is shown in as peak 2 in figure5- 3. The majority of the mLbL samples we have studied and all of the IP samples only show this 1718 cm^{-1} peak and only when isopropyl acid is used as a rinsing agent do we observe the 1760 cm^{-1} peak for low cycle numbers. This observation is discussed in greater detail in section 5.5.2.

We assign the peak at 1612 cm^{-1} to combination of E2g (also known as ν_8)²⁴ derived C=C ring vibrations on both ring A and ring B. Our DFT experiments were not able to provide direct evidence that this peak overlaps with hydrogen bonded C=O at 1610 cm^{-1} as the optimized geometry did not allow any significant intramolecular hydrogen bonding. We do however assign a band at 1610 cm^{-1} to hydrogen bonded C=O based on literature assignments and our observed changes in this peak with hydration which we discuss in section 5.5.3. The amide II vibration at 1546 cm^{-1} results from N-H in plane bending which is coupled to the C-N stretch for Amide group in a trans configuration.^{34,35} There is close agreement between the observed and calculated position of this peak.

5.4.2.2Region II

The interaction of these ring modes of ring A and B in the 1612 cm^{-1} $\nu(\text{C}=\text{C})$ band is complex although it would be desirable to resolve and quantify these rings as a means to obtain monomer the ratio. We did however assign the peak at 1480 cm^{-1} solely to B1 bending stretch mode of the meta bi functionalized ring B and 1448 cm^{-1} to the E' vibration of 1,3,5 tri substituted ring A. This

peak assignment was confirmed by replacing MPD with DABA in the polymerization process. DABA possess the same substituent symmetry on the benzene ring as TMC and as such all the aromatic rings in the TMC-DABA polyamide have identical substituent symmetry. Figure 5-4 shows that when DABA is used the 1480 cm^{-1} B1 mode completely disappears and is replaced by the E' vibration of the 1,3,5 substituted ring. The 1480 peak is therefore a prime candidate for both quantifying incorporated MPD rings and as the dipole change of this vibration is in the plane of the ring³⁶⁻³⁸ it can also be used to calculate the orientation. When using this peak for qualitative studies in IP films care must be taken to completely remove all traces of the polysulfone support as the $\text{CH}_3\text{-C-CH}_3$ stretch of polysulfone (1489 cm^{-1}) has significant overlap.

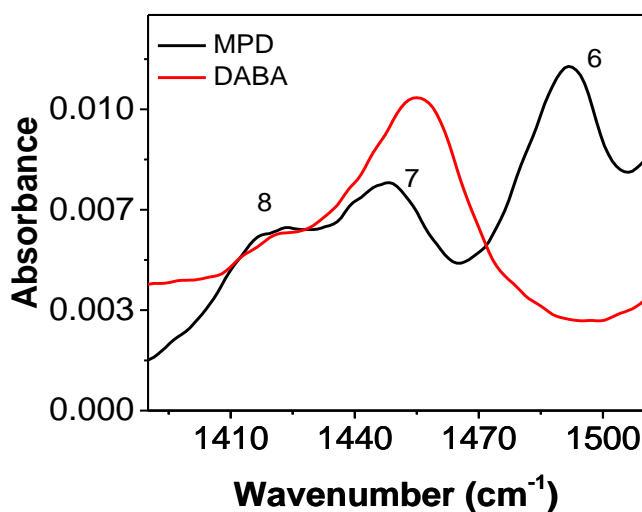


Figure 5-4. a) The three main peaks of region II and b) the spectrum of TMC-MPD poly(amide) overlaid with that of TMC-DABA poly(amide). Both samples are 30 cycles on a gold substrate. The peak numbers correspond to the numbers in the body of the text.

The 1425 cm^{-1} band is mostly the stretching vibration of the aromatic carbon bonded to an amide nitrogen. This peak overlaps with tri substituted E' derived ($\text{C}=\text{C}$) ring mode and appears around 1415 cm^{-1} in the mLbL system.

5.4.1.3 Region III

As is the case with region II we determined that this region is dominated by aromatic ring vibrations. For LBL films this region has few spectral features as displayed in Figure 5-5a, however for delaminated IP films where the polysulfone is not adequately removed there are several characteristic peaks that can be observed Figure 5-5b.

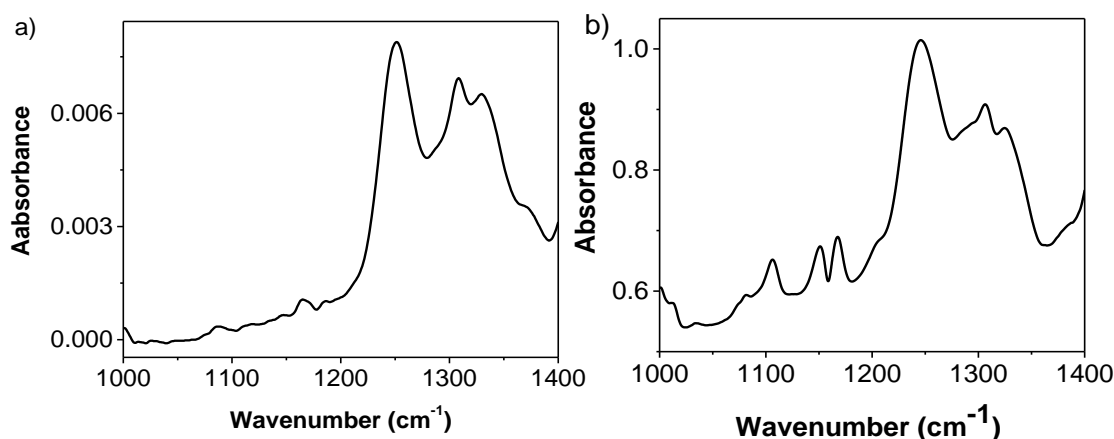


Figure 5-5. a) Region III for a 60 cycle LBL film on gold and b) the spectrum for the corresponding region in an IP film with peak numbers corresponding to peak numbers in the body of the text.

We assign the 1246 cm^{-1} band to the out of plane N-H bending coupled to C-N stretching in amide bond. This makes this peak a purely amide peak which is very sensitive to hydrogen bonding and N-D exchange when a polyamide film is exposed to D_2O . We have assigned the 1287 cm^{-1} to the in plane =C-H deformations on ring A and the 1325 cm^{-1} peak to a similar =C-H deformation on ring B. The peak at 1306 cm^{-1} is predominantly due to the amide C-N-C stretch. The peak assignments described above are summarized in table 5-1 below.

Table 5-1 Summarized peak assignments for MPD-TMC aromatic polyamide films showing the 13 most prominent peaks

peak	Position (cm ⁻¹)	DFT	Assignment	Ref
1	1765	1772	C=O stretch free acid chloride on TMC	27
2	1718	1757	C=O stretch from the COO- group on TMC	27
3	1672	1682	C=O stretch (mostly) coupled with C-C-N deformation and C-N stretch	23
4	1612	1600	combination of E2g (also known as vibration 8) derived C=C ring vibrations on TMC and MPD	26,27,41,42
5	1546	1541	N-H in plane bending and C-N stretch for Amide group in a trans configuration	24
6	1492	1496	B1 bending stretch mode of a meta bi functionalized ring	25,41,42
7	1448	1438	A1 ring vibration in MPD, overlaps with E' ring vibration of TMC	26,27
8	1425	1429	Aromatic C-N stretching (mostly). This peak overlaps with trisubstituted E' derived (C=C) ring mode	24
9	1325	1320	In plane =C-H deformations on MPD ring	41,42
10	1306	1295	Amide C-N-C stretch	34,35
11	1287	1282	in plane =C-H deformations on TMC ring	24
12	1246	1238	Interaction of N-H bending and C-N stretching in amide bond	35
13	1168	1187	CH vibration on MPD ring	24

5.3.2 Effect of sample preparation

With the advent of mLbL PA films there is the potential to translate what we learn from these films to interfacially polymerized systems. It is important to know therefore if any spectral differences arise for chemically identical systems as a result of the method of sample preparation and if those differences can inform us about structural differences. In order to study these differences, we prepared mLbL films on gold and silicon substrates and studied the growth of the initial layers. Unsurprisingly the growth of the initial polymer layers is dependent on the substrate

but is also affected by the solvent used in the rinsing step. In the mLbL deposition process excess monomer is rinsed off using either acetone or isopropyl alcohol. On both substrates consistently higher thickness values were observed when IPA was used as the rinse solvent (Table 5-3 supporting information).

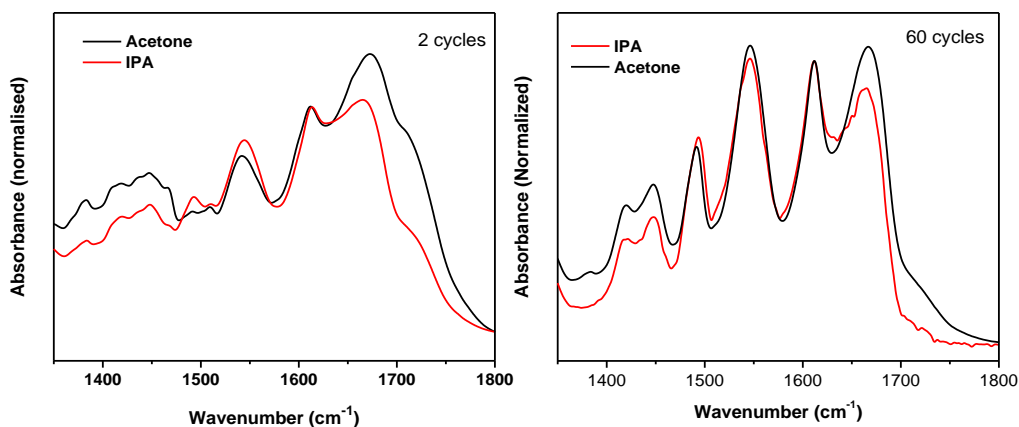


Figure 5-6. a) 2 cycle mLbL film on gold substrate showing spectral differences when rinsed by IPA and acetone and b) corresponding plot for a 60 cycle sample on gold. All spectra were normalized to the 1612 cm^{-1} peak

This is possibly as a result of Acetone being a better solvent and removing more excess monomer. When IPA is used the un-rinsed excess monomer either remains unreacted or forms short loosely cross-linked oligomers which become entangled with the developing polymer and add to the film thickness. With acetone on the other hand most of the excess monomer is removed before subsequent steps resulting in a higher crosslink density and a better defined thin polymer film. As a consequence, the acetone rinsed films have more amide linkages at a given cycle as shown by the increased absorbance at the 1672 cm^{-1} amide C=O peak, Figure 5-6. Acetone rinsed samples were used to study the growth of the initial layers on gold and silicon. On both substrates TMC was deposited as the first half layer. On silicon substrates the introduction of MPD at cycle 1 resulted in the formation of amide bonds indicating the onset of polymerization.

Figure 5-7a shows that the spectrum of 1 cycle sample shows a peak at 1675 cm^{-1} which corresponds to the formation of amide linkages, the 1 cycle sample also shows a sharp peak at 1750 cm^{-1} due to large excess of unreacted TMC. At this low cycle number polymer network is relatively loosely cross-linked and as a result there is a significant amount of free acid which reduces in subsequent cycles as the crosslink density increases. Figure 5-7a reflects this trend as at 1.5 cycles the amide linkage C=O has a higher intensity although there is still a significant free acid absorbance at 1720 cm^{-1} .

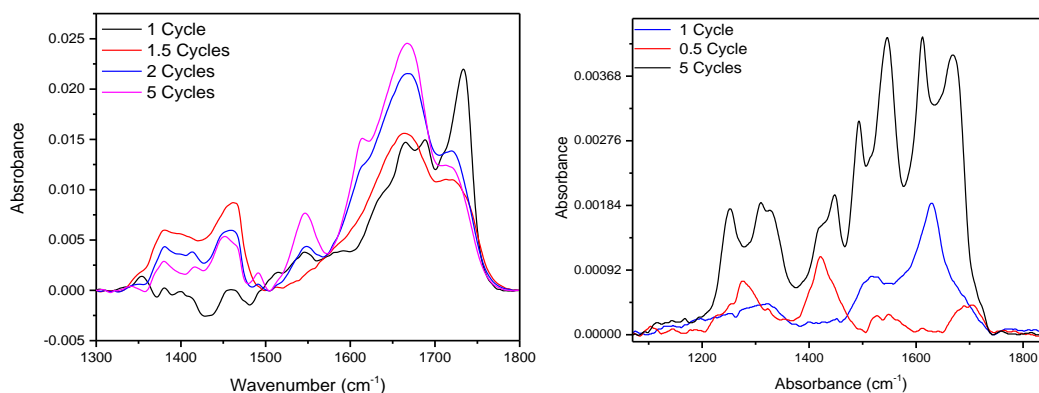


Figure 5-7. SO-ATR spectra of the initial mLBL cycles on a) silicon and b) gold substrates

The XPS data displayed in Figure 5-8 and 5-15 in the supporting information confirms a gradual increase of the ratio of amide to free acid C=O as cycle numbers increase for whole number cycles. The high free acid content observed in half cycle numbers is due to the TMC being the last layer deposited and hence the surface of the film possessing a large amount of unreacted COO⁻ functional groups. On gold however the addition of MPD to the initial TMC half layer results mostly in the non-reactive displacement of the TMC. FTIR data reveals very little amide bond formation and the coexistence of unreacted TMC acid and MPD signatures. This is unsurprising the affinity of amines to gold surfaces is well established.^{39,40}

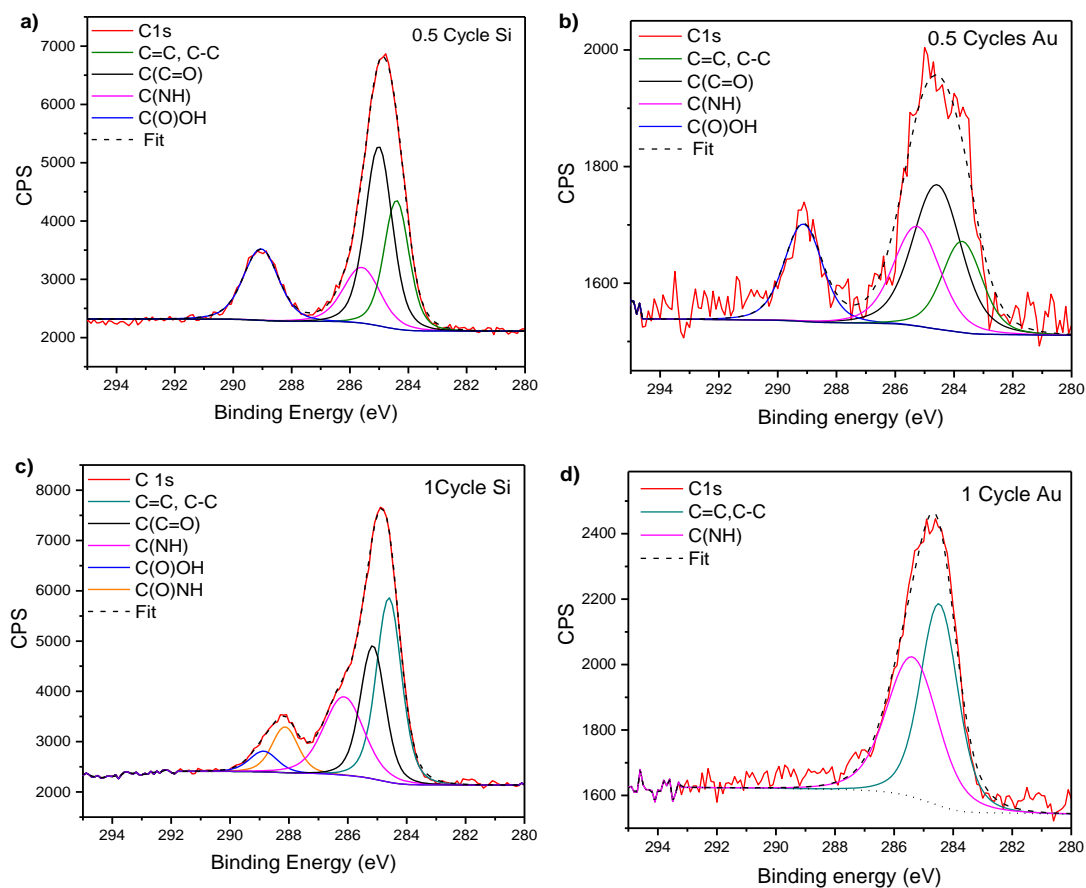


Figure 5-8. XPS spectra of the first layer of mLB film growth, cycle 0.5 is the deposition of TMC monomer and cycle 1 is the deposition of MPD.

Figure 5-7b shows that at 0.5 cycles TMC peaks are observed but at 1 cycles a mixture of TMC and MPD peaks are observed but no peaks that correspond to amide linkages are observed. It is only when the next TMC layer is deposited that amide C=O linkages begin to appear. XPS data in figure 8 d also shows that the TMC COO⁻ peak disappears completely at 1 cycle. From cycle number 2 the XPS profiles on both substrates look similar (figure 5-16 and 5-17) and the FTIR data also shows that the network growth of the two substrates is similar.

5.3.3 Effect of hydration

Upon hydration of the MPD-TMC PA system it is apparent that the δ N-H of the amide II peak blueshifts while the C=O of the Amide I peak redshifts. From Figure 5-9a it is apparent that there is also a noticeable increase in the absorbance between 1500 cm^{-1} and 1700 cm^{-1} which can be attributed to overlap with the three OH bending vibrations located at 1675 cm^{-1} , 1635 cm^{-1} , and 1595 cm^{-1} .⁴¹ This overlap is particularly problematic when attempting to glean information about the hydrogen bonding changes in the polyamide film using subtractive normalization methods as it is difficult to deconvolute peak shifts that arise from hydrogen bonding changes from those induced by the growth of the water peak. One way of overcoming this challenge is to use D_2O as the OD resonances are at lower frequencies. When D_2O is used instead of H_2O N-D exchange takes place converting the amide N-H bond to an N-D bond which is demonstrated in figure 5-9b by the lowering of the intensity of the amide II band at 1546 cm^{-1} and δ N-H band at 1243 cm^{-1} .

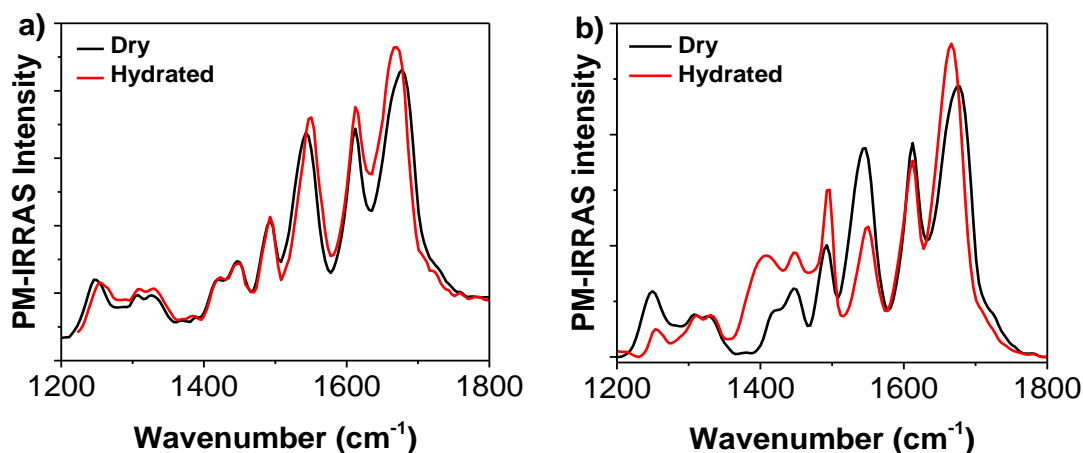


Figure 5-9. a, dry and Hydrated transmission spectra of interfacially polymerized TMC-MPD films and b) the peak position of the amide II peak (1532 cm^{-1}) and N-H bending mode as a function of time exposed to water vapor at 90% RH

Figure 5-9b also shows the expected increase in intensity around 1390 and 1500 cm^{-1} due to overlap with OD bending modes. Efforts to understand water interactions with polymers typically involve interpreting subtle shifts either in the water peaks or the functional groups water interacts with. It has been suggested that for the polyamide system a difference spectrum resulting from subtracting a spectrum of a polyamide in the dry state (0 % RH) from a spectrum of the hydrated state (100 % RH) can be used to analyze the amide I peak at 1661 cm^{-1} and better understand how the carbonyl moieties interact with water.⁴² Our PM-IRRAS experiments reveal this strategy is only valid under certain conditions. The amide I peak can only be used when the water vapor is 100% D₂O to avoid the introduction of artifacts from the OH bending modes of water. Further if 100% H₂O is used the blueshift of the $\delta\text{N-H}$ peak can be used in exactly the same manner as the amide I peak to understand the interaction of the N-H group with water. Figure 5-10 clearly shows that the $\delta\text{N-H}$ peak responds to hydration with H₂O in a similar manner to the amide II peak, which implies that in for determining hydration induced changes in hydrogen bonding that the N-H band at 1243 cm^{-1} can provide equivalent information to the amide I peak.

Figure 5-10 provides prima facie evidence that the 1243 cm^{-1} peak is unaffected by OH band overlap hence its peak position does not fluctuate as much as the amide I peak making it a better candidate for interrogating water N-H interactions.

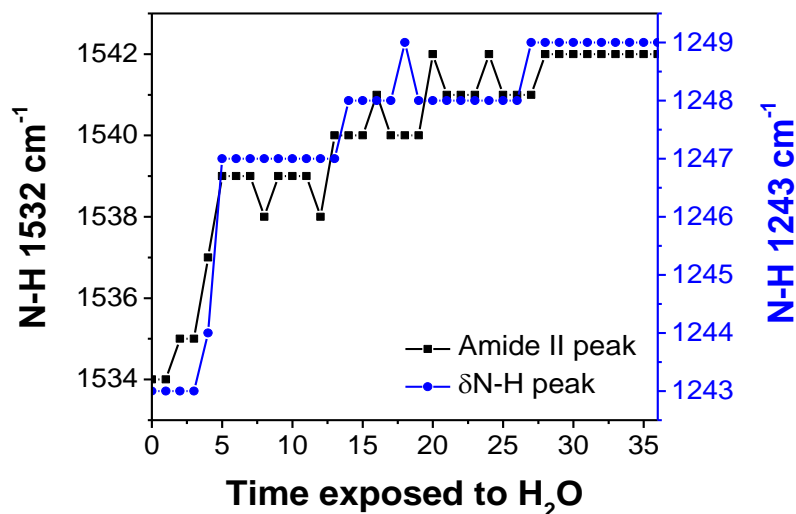


Figure 5-10. peak shifts observed in amide I and δ N-H peak for aa 60 cycle sample on gold exposed H_2O vapor at 90% RH

5.4 Conclusion

In conclusion the fingerprint region of Aromatic polyamide films as with most polymers is highly convoluted. We have demonstrated that although the fingerprint region is dominated by aromatic vibrations there are several peaks that can be used to obtain information about the acid content, structural changes during polymerization and hydration of these films. We have demonstrated that the free acid shoulder at 1710 cm^{-1} which belongs to carboxylic acid groups on TMC derived rings in the polymer network. For mLbL samples with low cycle numbers we observed the free acid peak at 1760 cm^{-1} which is consistent with the position of the $\nu(\text{C=O})$ of the acyl chloride group of un-hydrolyzed TMC. From this observation we draw the conclusion that when there is a large amount of free acid in the developing polymer network not all of the acyl

chloride groups are hydrolyzed but as polymerization proceeds most of the free acid exists in the hydrolyzed form. We have also demonstrated that for mLbL films synthesized on both gold and silicon substrates the initial layers are only loosely cross-linked as evidenced by the high free acid concentration corresponding to the 1718cm^{-1} shoulder. As polymerization increases the ratio of the Amide I to the free acid peaks increases showing that the relative free acid concentration decreases while the concentration of amide bonds increases. This suggests that the degree of crosslinking increases as cycle number increases. On gold substrates The amine group of MPD has greater affinity to the surface than the TMC acyl chloride groups resulting in the displacement of the initial monomer layer upon spin casting, hence amide linkages only begin to form at cycle 1.5. When hydrated subtle shifts are observed in the amide I and Amide II regions. The N-H in-plane mode at 1243 cm^{-1} showed a similar response to hydration as a function of time as the amide II peak and we suggest it is the most reliable peak in the fingerprint region to monitor peak shifts that result from hydrogen bonding changes in the polymer network. Such studies must be conducted by using pure D_2O vapor and monitoring the amide I peak position alone or by using pure H_2O and solely monitoring the $\delta(\text{N-H})$ peak at 1243 cm^{-1} . This work has contributed to our understanding of RO membranes by elucidating all the major contributions to the fingerprint IR spectrum of aromatic polyamide membranes and by specifically identifying the peaks that may be used to obtain information about cross-link density, monomer ratio, acid content and orientation. In the following chapter we shall address the latter.

5.5 Supporting Information

Aromatic Ring vibrations

The fingerprint region of polyamide systems is dominated by aromatic ring vibrations of TMC and MPD monomers. The vibrational spectra of benzene and its derivatives is well studied and understood. In brief the main peaks we observe result from the in plane tangential carbon-carbon vibrations known as vibration 8 and 19. Both these vibrations exist as degenerate pairs and the dipole changes that result from these vibrations are sensitive to the symmetry of the ring hence we obtain distinct peaks for a 1,3,5 substituted ring and a meta substituted ring regardless of the identity of the substituents. This allows us to distinguish between MPD and TMC both as free monomers and when incooperated in the polymer network.

MPD ring modes

Katrinzky, Jones and Simmons have published detailed surveys of frequencies and band intensities of m- substituted benzene rings.^{25,43,44} The vibrational pair 8 occurs between 1590 cm⁻¹ and 1622cm⁻¹ depending on the electronegativity of the substituents. In MPD vib 8a occurs at 1605 cm⁻¹ vib 8b occurs at 1613 cm⁻¹. In MPD the vibrational pair 19 has A₁ symmetry and vib 19a occurs at 1490 cm⁻¹ with A₁ symmetry while vib 19b occurs at 1501 cm⁻¹ with B₂ symmetry. These vibrations in polyamide literature are often referred to as “ring breathing” atomic motions in these vibrations are more accurately described as bending stretching vibrations as shown in Figure 5-11 below.

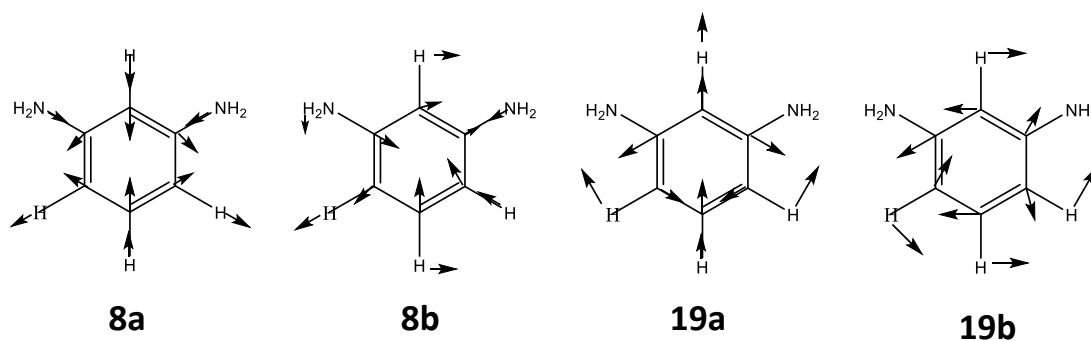


Figure 5-11. Cartesian coordinate representation of bending stretching vibrations 18 and 19 of MPD rings²⁴

Fitting these four modes into the experimental MPD monomer spectrum yielded a good fit when a fifth peak we attribute to the N-H bend is added, Figure 5-12. As the position of these bands is largely governed by the number and position of substituents and these do not change after polymerization, we believe it is a fair assumption that the band positions we assigned are valid for the mLbL system. Some modes overlap with Amide I complicating C=O orientation calculations. There is minimal overlap from the N-H at 1500 cm^{-1} so this band can be used for orientation/quantitative analysis of MPD rings.

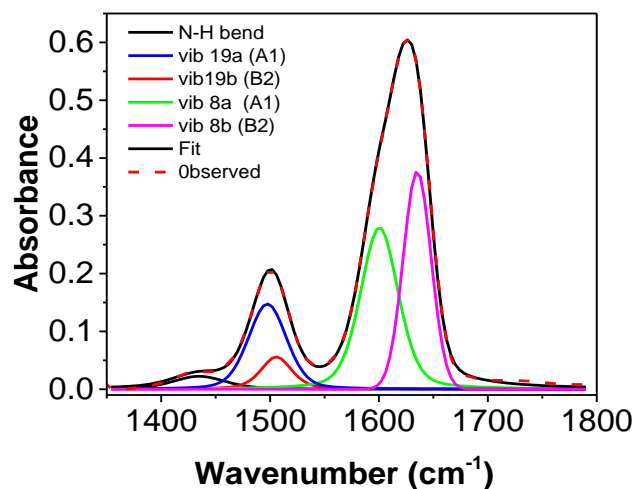


Figure 5-12. Fit of the MPD spectrum between 1350 cm^{-1} and 1800 cm^{-1} showing the positions of the major peaks of vibrations 8 and 19

TMC ring modes

In TMC several ring modes exist, most of which overlap or are in close vicinity with the ring modes of MPD. Figure 5-13 shows the three predominant vibrations. Vibration 9 is observed between 1570 cm^{-1} and 1613 cm^{-1} while vibration 18 is observed between 1100 cm^{-1} and 1230 cm^{-1} . Both these vibrations are predominantly in plane C-H deformations. Vibration 19a is a bending stretching vibration with E_a symmetry at 1432 cm^{-1} in monomer and observed at 1447 cm^{-1} for ring A in the polymer, vibration 19b has E_b symmetry and observed at 1430 cm^{-1} .

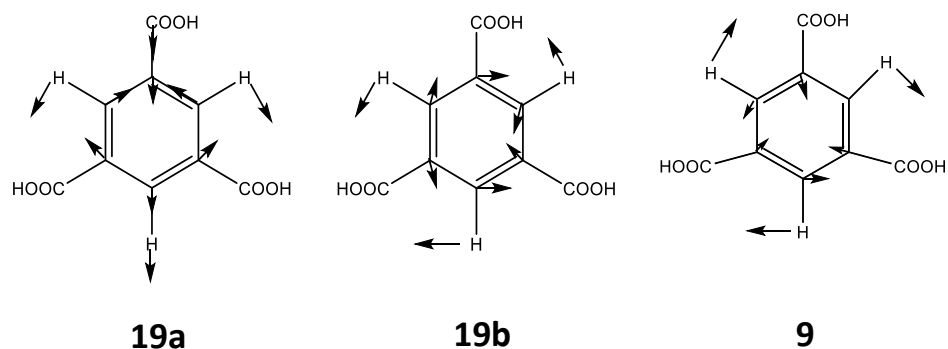


Figure 5-13. the atomic motion in vibrations 18 and 9 of TMC and their observed peak positions in the monomer IR spectrum²⁴

The FTIR spectrum of neat liquid TMC is shown in Figure 5-14 below the 1760 cm^{-1} peak corresponds to the acyl chloride C=O stretch.

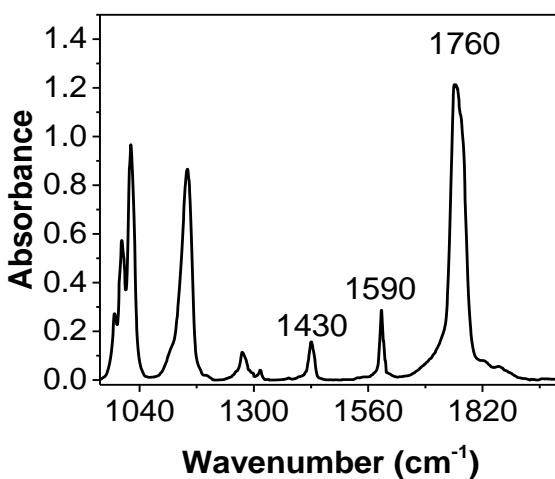


Figure 5-14. ATR spectrum of Neat TMC

The spectrum of delaminated polyamide has is not adequately isolated contains multiple peaks from the support layer. The peaks that arise from the polysulfone support can clearly be seen when an isolated membrane that has been thoroughly cleaned is compared to one that has only been partially isolated. Figure 15 below shows the spectra of two samples washed in DMF for different times.

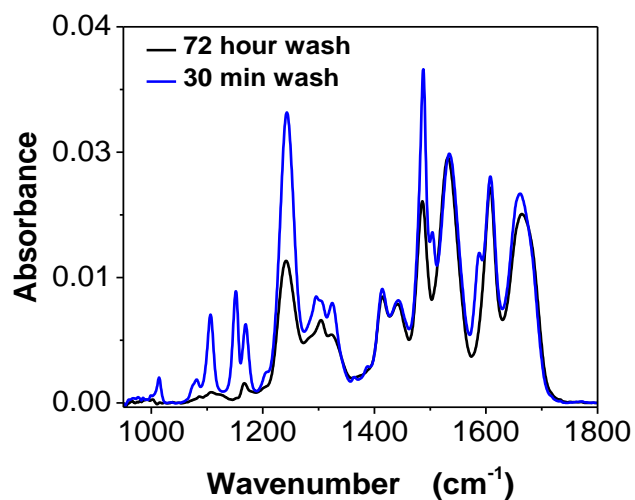


Figure 5-15. Transmission spectrum of delaminated interfacially polymerized polyamide film which has not been adequately rinsed overlaid with one that has been thoroughly isolated over a 72-hour period.

Table 5-1. Thickness of mLbL samples as determined by Ellipsometry

Silicon		Gold	
Cycles	thickness (nm)	Cycles	thickness (nm)
60	13.75	60	13.4
30	6	30	11.3
15	2.1	15	4.4
10	1.1	10	3.4
5	1.2	5	2
2	1	2	1.1
1.5	0.8	1.5	1.2
1	1.2	1	1
0.5	0.5	0.5	

Table 5-2. Thickness of mLbL samples prepared with IPA or acetone rinse as measured by spectroscopic ellipsometry

Cycle	Thickness (nm)	
	Acetone	IPA
Silicon		
5	1.04	12.2
10	2.27	5.1
15	9.18	7.54
30	7.85	12.1
60	19.47	28.8
Gold		
5	4.12	2.37
10	6.45	2.86
25	8.62	5.11
50	12.5	9.26

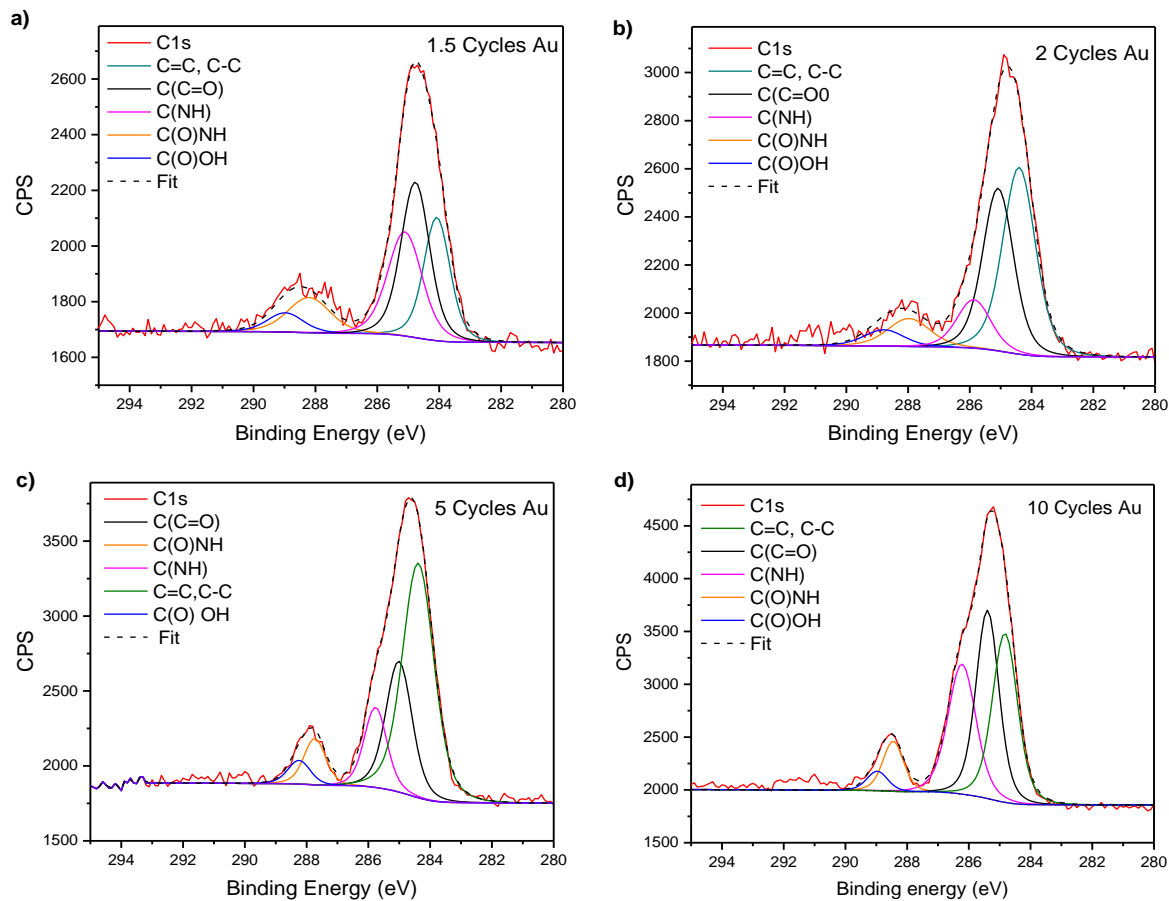


Figure 5-16. XPS spectra of 1.5 – 10 cycle mLBL samples prepared on gold.

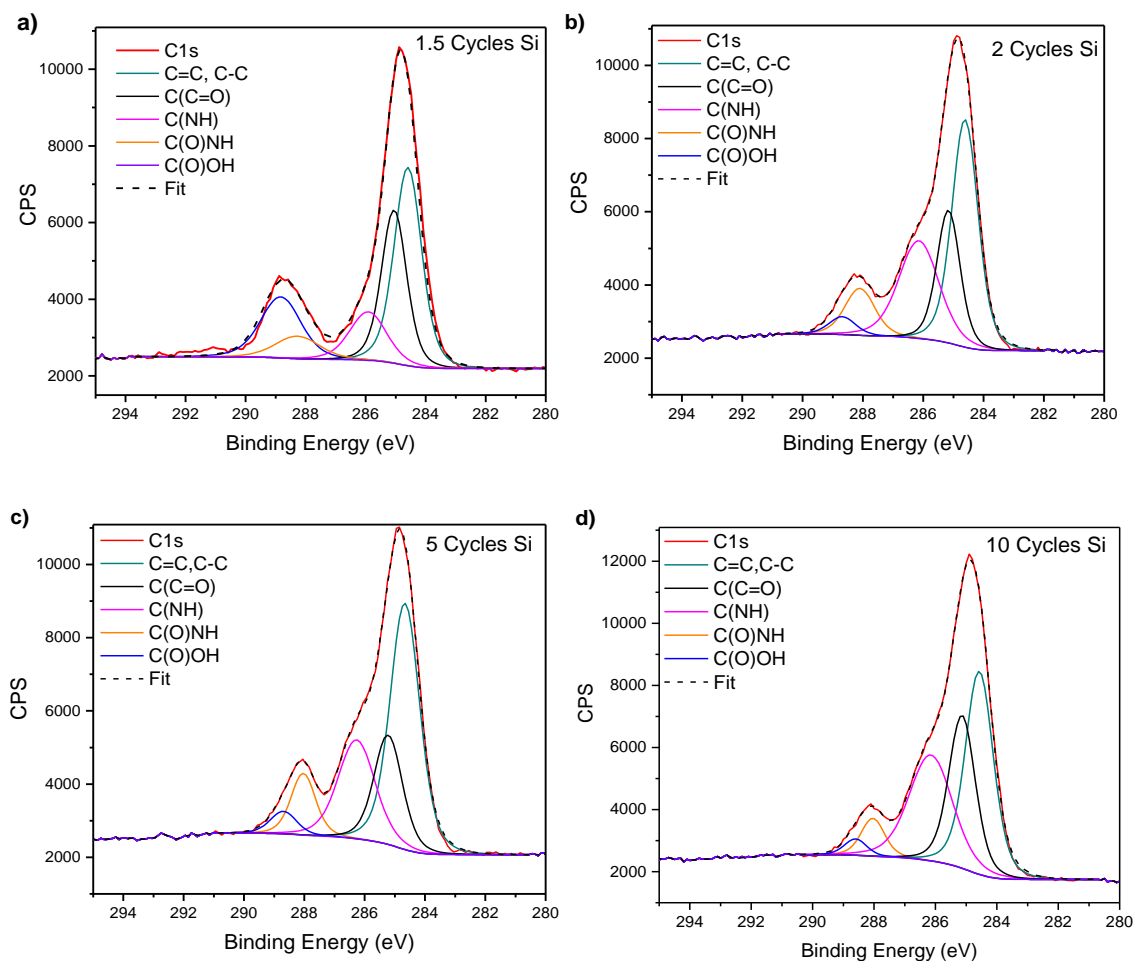


Figure 5-17. XPS spectra of 1.5 – 10 cycle mLBL samples prepared on Silicon

5.6 References

- (1) Elimelech, M.; Phillip, W. A. The Future of Seawater Desalination: Energy, Technology, and the Environment. *Science* (80-.). **2011**, 333 (6043), 712.
- (2) Jeong, B.-H.; Hoek, E. M. V; Yan, Y.; Subramani, A.; Huang, X.; Hurwitz, G.; Ghosh, A. K.; Jawor, A. Interfacial Polymerization of Thin Film Nanocomposites: A New Concept for Reverse Osmosis Membranes. *J. Memb. Sci.* **2007**, 294 (1–2), 1.
- (3) CADOTTE, J. E.; PETERSEN, R. J. Thin-Film Composite Reverse-Osmosis Membranes: Origin, Development, and Recent Advances. In *Synthetic Membranes*; ACS Symposium Series; AMERICAN CHEMICAL SOCIETY, 1981; Vol. 153, pp 21–305.
- (4) CADOTTE, J. E. Evolution of Composite Reverse Osmosis Membranes. In *Materials Science of Synthetic Membranes*; ACS Symposium Series; American Chemical Society, 1985; Vol. 269, pp 12–273.
- (5) Lau, W. J.; Ismail, A. F.; Misdan, N.; Kassim, M. A. A Recent Progress in Thin Film Composite Membrane: A Review. *Desalination* **2012**, 287, 190.
- (6) McKinney, R.; Rhodes, J. H. Aromatic Polyamide Membranes for Reverse Osmosis Separations. *Macromolecules* **1971**, 4 (5), 633.
- (7) Xie, W.; Geise, G. M.; Freeman, B. D.; Lee, H.-S.; Byun, G.; McGrath, J. E. Polyamide Interfacial Composite Membranes Prepared from M-Phenylene Diamine, Trimesoyl Chloride and a New Disulfonated Diamine. *J. Memb. Sci.* **2012**, 403–404, 152.
- (8) Johnson, P. M.; Yoon, J.; Kelly, J. Y.; Howarter, J. a.; Stafford, C. M. Molecular Layer-by-Layer Deposition of Highly Crosslinked Polyamide Films. *J. Polym. Sci. Part B Polym. Phys.* **2012**, 50 (3), 168.
- (9) Freger, V. Nanoscale Heterogeneity of Polyamide Membranes Formed by Interfacial Polymerization. *Langmuir* **2003**, 19 (11), 4791.
- (10) Coronell, O.; Mariñas, B. J.; Cahill, D. G. Depth Heterogeneity of Fully Aromatic Polyamide Active Layers in Reverse Osmosis and Nanofiltration Membranes. *Environ. Sci. Technol.* **2011**, 45 (10), 4513.
- (11) Vasanathan, N.; Salem, D. R. FTIR Spectroscopic Characterization of Structural Changes in Polyamide-6 Fibers during Annealing and Drawing. *J. Polym. Sci. Part B Polym. Phys.* **2001**, 39 (5), 536.
- (12) Ettori, A.; Gaudichet-Maurin, E.; Schrotter, J.-C.; Aimar, P.; Causserand, C. Permeability and Chemical Analysis of Aromatic Polyamide Based Membranes Exposed to Sodium Hypochlorite. *J. Memb. Sci.* **2011**, 375 (1–2), 220.
- (13) Varlot, K.; Reynaud, E.; Kloppfer, M. H.; Vigier, G.; Varlet, J. Clay-Reinforced Polyamide: Preferential Orientation of the Montmorillonite Sheets and the Polyamide Crystalline

Lamellae. *J. Polym. Sci. Part B Polym. Phys.* **2001**, 39 (12), 1360.

- (14) Vasanthan, N.; Salem, D. R. Infrared Spectroscopic Characterization of Oriented Polyamide 66: Band Assignment and Crystallinity Measurement. *J. Polym. Sci. Part B Polym. Phys.* **2000**, 38 (4), 516.
- (15) Kwon, Y.-N.; Leckie, J. O. Hypochlorite Degradation of Crosslinked Polyamide Membranes: II. Changes in Hydrogen Bonding Behavior and Performance. *J. Memb. Sci.* **2006**, 282 (1–2), 456.
- (16) Tang, C. Y.; Kwon, Y.-N.; Leckie, J. O. Effect of Membrane Chemistry and Coating Layer on Physiochemical Properties of Thin Film Composite Polyamide RO and NF Membranes: I. FTIR and XPS Characterization of Polyamide and Coating Layer Chemistry. *Desalination* **2009**, 242 (1–3), 149.
- (17) Antony, A.; Fudianto, R.; Cox, S.; Leslie, G. Assessing the Oxidative Degradation of Polyamide Reverse Osmosis membrane—Accelerated Ageing with Hypochlorite Exposure. *J. Memb. Sci.* **2010**, 347 (1–2), 159.
- (18) Tang, C. Y.; Kwon, Y.-N.; Leckie, J. O. Effect of Membrane Chemistry and Coating Layer on Physiochemical Properties of Thin Film Composite Polyamide RO and NF Membranes. *Desalination* **2009**, 242 (1–3), 149.
- (19) Kang, G.-D.; Gao, C.-J.; Chen, W.-D.; Jie, X.-M.; Cao, Y.-M.; Yuan, Q. Study on Hypochlorite Degradation of Aromatic Polyamide Reverse Osmosis Membrane. *J. Memb. Sci.* **2007**, 300 (1–2), 165.
- (20) Black, S. B.; Chang, Y.; Bae, C.; Hickner, M. A. FTIR Characterization of Water–Polymer Interactions in Supercritical Polymers. *J. Phys. Chem. B* **2013**, 117 (50), 16266.
- (21) Sammon, C.; Mura, C.; Yarwood, J.; Overall, N.; Swart, R.; Hodge, D. FTIR–ATR Studies of the Structure and Dynamics of Water Molecules in Polymeric Matrixes. A Comparison of PET and PVC. *J. Phys. Chem. B* **1998**, 102 (18), 3402.
- (22) Moilanen, D. E.; Piletic, I. R.; Fayer, M. D. Tracking Water's Response to Structural Changes in NAFION Membranes. *J. Phys. Chem. A* **2006**, 110 (29), 9084.
- (23) Kwon, Y.-N.; Tang, C. Y.; Leckie, J. O. Change of Chemical Composition and Hydrogen Bonding Behavior due to Chlorination of Crosslinked Polyamide Membranes. *J. Appl. Polym. Sci.* **2008**, 108 (4), 2061.
- (24) Varsanyi, G. *Vibrational Spectra of Benzene Derivatives*; Academic press: London, 1969.
- (25) Katritzky, A. R.; Sinnott, M. V.; Tidwell, T. T.; Topsom, R. D. Infrared Intensities as a Quantitative Measure of Intramolecular Interactions. V. Ortho- and Meta-Disubstituted Benzenes. Nu16 Band near 1600 Cm.⁻¹. *J. Am. Chem. Soc.* **1969**, 91 (3), 628.
- (26) Green, J. H. S.; Harrison, D. J.; Kynaston, W. Vibrational Spectra of Benzene derivatives—

XII 1,3,5- and 1,2,3-Trisubstituted Compounds. *Spectrochim. Acta Part A Mol. Spectrosc.* **1971**, 27 (6), 793.

- (27) Mahalakshmi, G.; Balachandran, V. FT-IR and FT-Raman Spectra, Normal Coordinate Analysis and Ab Initio Computations of Trimesic Acid. *Spectrochim. Acta Part A Mol. Biomol. Spectrosc.* **2014**, 124, 535.
- (28) Freger, V. Swelling and Morphology of the Skin Layer of Polyamide Composite Membranes: An Atomic Force Microscopy Study. *Environ. Sci. Technol.* **2004**, 38 (11), 3168.
- (29) Smedley, S. B.; Chang, Y.; Bae, C.; Hickner, M. A. Measuring Water Hydrogen Bonding Distributions in Proton Exchange Membranes Using Linear Fourier Transform Infrared Spectroscopy. *Solid State Ionics* **2015**, 275, 66.
- (30) Borowski, P.; Pasieczna-Patkowska, S.; Barczak, M.; Pilorz, K. Theoretical Determination of the Infrared Spectra of Amorphous Polymers. *J. Phys. Chem. A* **2012**, 116 (27), 7424.
- (31) Bouř, P.; Sopková, J.; Bednářová, L.; Maloň, P.; Keiderling, T. A. Transfer of Molecular Property Tensors in Cartesian Coordinates: A New Algorithm for Simulation of Vibrational Spectra. *J. Comput. Chem.* **1997**, 18 (5), 646.
- (32) Bour, P.; Kubelka, J.; Keiderling, T. A. Ab Initio Quantum Mechanical Models of Peptide Helices and Their Vibrational Spectra. *Biopolymers* **2002**, 65 (1), 45.
- (33) Choi, J.-H.; Cho, M. Amide I Raman Optical Activity of Polypeptides: Fragment Approximation. *J. Chem. Phys.* **2009**, 130 (1).
- (34) Barth, A.; Zscherp, C. What Vibrations Tell about Proteins. *Q. Rev. Biophys.* **2002**, 35 (4), 369.
- (35) Tsuboi, M.; Kubo, Y.; Akahane, K.; Benevides, J. M.; Thomas, G. J. Determination of the Amide I Raman Tensor for the Antiparallel β -Sheet: Application to Silkworm and Spider Silks. *J. Raman Spectrosc.* **2006**, 37 (1-3), 240.
- (36) Scherer, J. R. Group Vibrations of Substituted benzenes—I. *Spectrochim. Acta* **1963**, 19 (3), 601.
- (37) Scherer, J. R. Group Vibrations of Substituted benzenes—II. Planar CH Deformations and Ring Stretching and Bending Modes of Chlorinated Benzenes. *Spectrochim. Acta* **1965**, 21 (2), 321.
- (38) Green, J. H. S. Vibrational Spectra of Benzene derivatives—VIII: M-Disubstituted Compounds. *Spectrochim. Acta Part A Mol. Spectrosc.* **1970**, 26 (7), 1523.
- (39) Hooper, A. E.; Werho, D.; Hopson, T.; Palmer, O. Evaluation of Amine- and Amide-Terminated Self-Assembled Monolayers as “Molecular Glues” for Au and SiO₂ Substrates. *Surf. Interface Anal.* **2001**, 31 (9), 809.

- (40) Chen, F.; Li, X.; Hihath, J.; Huang, Z.; Tao, N. Effect of Anchoring Groups on Single-Molecule Conductance: Comparative Study of Thiol-, Amine-, and Carboxylic-Acid-Terminated Molecules. *J. Am. Chem. Soc.* **2006**, 128 (49), 15874.
- (41) Jin, Y.; Wang, W.; Su, Z. Spectroscopic Study on Water Diffusion in Aromatic Polyamide Thin Film. *J. Memb. Sci.* **2011**, 379 (1–2), 121.
- (42) Smedley, S. B. Water Hydrogen Bonding In Proton Exchange and Neutral Polymers, Pennsylvania State University, 2015.
- (43) Katritzky, A. R.; Simmons, P. 414. Infrared Absorption of Heteroaromatic and Benzenoid Six-Membered Monocyclic Nuclei. Part VIII.-Meta-Disubstituted Benzenes. *J. Chem. Soc.* **1959**, No. 0, 2058.
- (44) Katritzky, A. R.; Jones, R. A. 416. Infrared Absorption of Substituents in Aromatic Systems. Part II. Acylamino-Compounds. *J. Chem. Soc.* **1959**, No. 0, 2067.

Chapter 6

Acid Content and Orientation Of Thin Polyamide Reverse Osmosis Membrane Films On Non-Porous Substrates

6.1 Introduction

The formation of stable thin films with well-defined and predictable water transport properties has long been of interest for water purification and reverse osmosis applications.¹ The inextricable tie between membrane structure and properties makes it imperative to first understand the molecular structure of these thin films before any strides can be made in improving the permselectivity, fouling resistance and resistance to oxidation.² Currently thin film composite reverse osmosis membranes are based on a polyamide thin-film made by interfacial polymerization of an aromatic polyamine such as m-phenylenediamine (MPD) with aromatic polyacyl halides such as trimesoyl chloride (TMC). Interfacially polymerized films however suffer from chemical inhomogeneity and high surface roughness making characterization of structure property relationships difficult in most cases.³ To this end molecular layer by layer (mLbL) synthesized RO membranes have been developed with controllable chemical composition and vastly improved surface roughness.^{4,5} The development of mLbL films with controlled thickness opens up new possibilities to employ high-fidelity characterization methods to elucidate the structure of these materials.

Currently the most widely methods used to probe the surface morphology, composition and charge have been X-ray photoelectron spectroscopy (XPS), attenuated total reflection Fourier transform infrared spectroscopy (ATR-FTIR)⁶, atomic force microscopy (AFM)^{7,8} scanning electron microscopy (SEM)⁹ and transmission electron microscopy (TEM).¹⁰ While methods such

as XPS, AFM, and ellipsometry can give information about film thickness and chemical composition these methods cannot directly provide the information about molecular orientation required to fully understand film properties.

NEXAFS provides information about orientation and electronic structure by probing transitions usually from the k-edge of an atomic species into the molecular orbitals of bonds to neighboring atoms.¹¹ When polarized X-rays are used in a NEXAFS experiment for aromatic systems, similar to the polyamide system presented in this paper, the search light effect allows ring orientation to be determined. Peaks due to the out-of-plane π orbitals are observed when the electric field vector of the linearly polarized X-rays is aligned along the surface normal while resonances due to the in-plane σ orbitals are observed when the electric field vector is aligned parallel to the surface.

FTIR methods, on the other hand, can provide detailed molecular orientation and are routinely employed to determine orientation parameters such as dichroic ratios in films and adsorbed layers on ATR crystals.¹²⁻¹⁴ Gliboff et al recently demonstrated that combined FTIR and NEXAFS studies are a powerful tool in determining molecular orientation. They combined angle dependent NEXAFS with polarization modulation infrared reflection absorption spectroscopy (PM-IRRAS) to determine the molecular orientation of a model phenylphosphonic acid on an indium zinc oxide substrate. They found quantitative agreement between the NEXAFS and PM-IRRAS experiments which showed the phenylphosphonic acid was well-orientated with a tilt angle of 12-16° from the surface normal.¹⁵

The use of mLbL synthesis also opens up the use of Reflection absorption infrared spectroscopy (RAIRS) and grazing angle ATR (GAATR) as means to determine molecular orientation. Allara, et al. developed an approach to obtain quantitative orientation information from RAIRS spectra combined with spectral simulations.¹⁶ This approach involves comparing the sample RAIRS spectrum to that of a calculated isotropic film of identical thickness on the same substrate.¹⁷ Unemara, et al. proposed a method that replaced the calculated isotropic spectrum with a real

spectrum of a film deposited on an IR element such as ZnSe, which unfortunately is not always practically feasible.¹² Iida, et al. demonstrated a simplified procedure that eliminated the need for a calculated spectrum provided it is possible to observe three peaks whose transition moments are mutually perpendicular.¹⁸ It is however not always possible to obtain three distinct modes which are mutually orthogonal. This is particularly true for the TMC/MPD polyamide system, where the out of plane aromatic ring modes are either too weak to be observed in nanometer scale thick films or occur outside the spectral window.

6.2 Methods

Optical constants for polyamide films were determined from transmission experiments using KBr pellets containing interfacially polymerized PA film. A 1.87 wt % PA in KBr was made by mixing 3.2 mg PA with 167.8 mg of KBr and grinding the mixture for 400 seconds in a wig-l-bug vibrating mill (Patterson dental, saint Paul,MN) to minimize grinding effects on absorption values.¹⁹ 18 mg of the resulting mixture diluted to 60.9 mg with KBr to give a 5.53 wt% sample mixture. The sample mixture pressed into several 7 mm pellets at a pressure of 2 tons in a hydraulic press and the transmission spectrum was collected immediately after pellet preparation to minimize water uptake by the KBr matrix. All FTIR measurements were conducted as described in chapter 3 identical to PA samples to improve baseline quality.²⁰ After collection of spectra the thickness of each pellet was measured to obtain the path length for Beer-Lambert calculations of k spectra.¹⁷ spectral simulation was conducted as described in section 3.5 of chapter 3 using optical constants provided in the supporting information.

Interfacially polymerized films of 0.11, 0.152, 0.215 0.31 and 0.326 meq/g ion exchange capacity (iec) were provided by Dow Chemical and used to prepare KBr disc samples as described

earlier for the determination of optical constants. The thickness of each pellet was measured and transmission experiments conducted as described in section 3.3 of chapter 3.

6.3 Results and Discussion

6.3.1 Orientation

The intrinsic scalar optical constants were obtained by analyzing the material's optical response in a bulk phase for which on average molecules assume random orientations. This was accomplished by generating a random dispersion of small polyamide crystallites in an inert KBr matrix. The KBr sample provided the basis for a convenient method of determining isotropic scalar optical functions from the analysis of a normal incidence transmission IR spectrum of a pressed pellet of known thickness and concentration of dispersed material. The transmission experiment provided a good first approximation of the absorption constants of the polyamide from a Beer-Lambert type of relationship.

$$I/I_0 = \exp(-4kvt) \quad 6-1$$

This initial guess set of wavelength dependent k values is termed a k spectrum and looks identical to an absorbance spectrum. Each value of the k spectrum was used in the kramers kronig equation to generate a corresponding set of n values. The n and k values were refined in an iterative process until the absorbance spectrum obtained from the final n and k set matched the original experimental spectrum. As a final check two further KBr samples were generated of different thickness were analyzed and compared to spectra simulated from the final set of n and k values. The optical constants of polyamide determined by this method are shown in (figure 6-1) below.

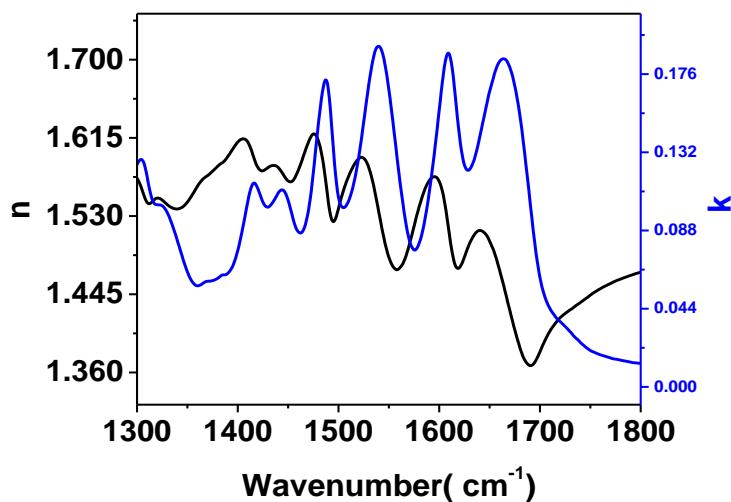


Figure 6-1. The n and k spectrum in the MIR region used as accepted optical constants for spectral simulation.

As discussed in section 3.3 in chapter 3, for surface oriented molecules in an external reflection geometry, there is electric field amplitude at infrared frequencies only normal to the surface. As a result, the absorbance for a vibrational band is proportional to the square of the electric field amplitude at the surface, the magnitude of the transition dipole moment (μ), and the tilt angle θ of μ from the surface normal.

$$A \propto E^2 \mu^2 \cos^2 \theta \quad 6-2$$

Due to the anisotropy of surface electric field amplitude, the absorbance of a mode with a transition moment oriented along the surface normal will be three times as large as the integrated absorbance of the same vibrational band of identical molecules in a thin film of equivalent thickness and molecular density. Thus, the tilt angle of a given transition dipole moment is calculated using

$$\frac{I_{obs}}{3I_{cal}} = \cos^2 \theta \quad 6-3$$

Where I_{obs} is the experimental absorbance of the diagnostic mode, I_{cal} is the simulated absorbance of the same mode and θ is the angle between the dipole change of the mode and the electric field vector. In both the SO-ATR and RAIRS experiments the electric field is surface normal, hence θ is the angle between the dipole change and the substrate normal. The diagnostic peak selected for the C=O bond orientation was the Amide I peak which consists primarily of the amide C=O stretch at 1672 cm^{-1} . There is a minor contribution of the C-N stretch which is coupled to the C=O stretch resulting in the shifting of the orientation of the dipole change out of the C=O bond plane, Figure 6-2. This shift has been demonstrated to be approximately 18° - 20° out of the double bond plane in protein research²¹ and this is consistent with reported dipole orientation in some aromatic amide systems.²² Experimental spectra were obtained using SO-ATR on silicon substrates as it provided superior sensitivity to Brewster angle experiments and because the electric field is exclusively z-polarized in the thickness regime of the mLbL samples analyzed. RAIRS was used for samples on gold because as demonstrated in figure 4-2 in chapter 4 optical simulations of SO-ATR often underestimate absorbance as they do not adequately account for surface plasmon effects.

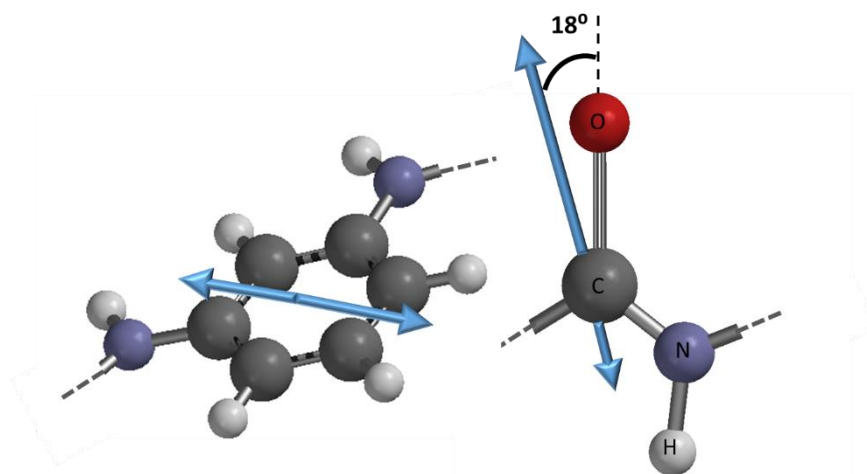


Figure 6-2. The orientation of the dipole changes for the disubstituted aromatic ring and amide I vibration of aromatic polyamide membranes.

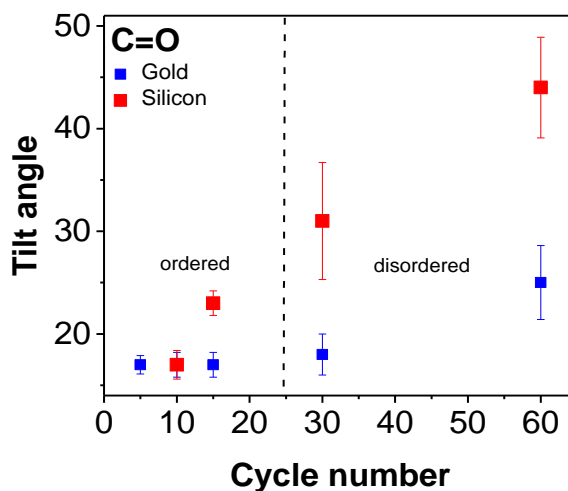


Figure 6-3. The tilt angle of the C=O bond of the amide group with respect to surface normal on gold and silicon substrates

The tilt angles obtained for the C=O group are presented in figure 6-3. At cycle numbers 5 to 15 the average angle with respect to the surface normal was approximately 16- 18° with very little deviation in the measured angle while bigger variations were observed for higher cycle numbers. For 60 cycle films on silicon for example, the average tilt angle tilt angle was 43.2 ± 2.5 while for 10 cycles it was 16.7 ± 0.7 . we attribute this difference to local sample heterogeneity increasing as the cycle number increases and to increasing isotropy of the film. While the amide C=O band provides a fair approximation of molecular order, the overlap of the free acid band and the sensitivity of the band to hydrogen bonding increases the uncertainty in the values obtained. These sources of uncertainty do not exist however for the peak at 1490 cm^{-1} we ascribed solely to the bending stretching aromatic ring vibration of a meta disubstituted benzene ring^{23,24}, hence this vibration was used to determine a more accurate measure of orientation for the rings in the polyamide system. The dipole change for this vibration is in the plane of the aromatic ring hence it can be used to directly obtain the tilt angle of the aromatic rings with respect to the surface

normal. As with the C=O group there was little deviation in the angle measure for cycle numbers 5, 10 and 15 and very large deviation in cycle numbers above 15. As some of the calculated tilt angles for the 60 cycle film were at or close to the magic angle of 54° we believe that these films have very little order.

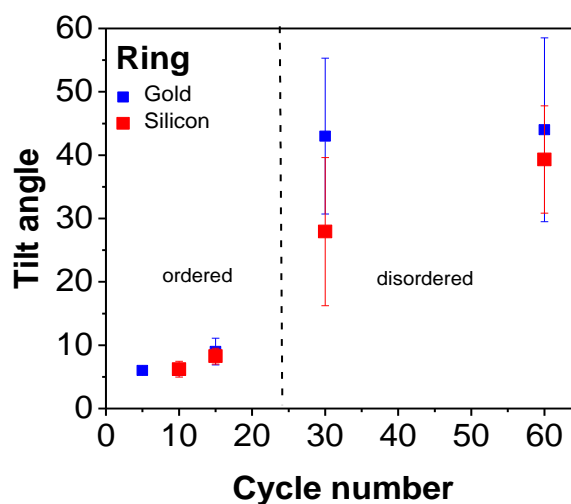


Figure 6-4. Tilt angle of the disubstituted aromatic ring with respect to the surface

This strong ordering at low cycle numbers is confirmed by angle dependent NEXAFS which shows anisotropy in the orientation of aromatic rings at low cycle numbers. Figure 6-5 shows the angular dependence of the C=C π^* feature originating from antibonding orbital of the phenyl rings which is observed in the first half layer and persists up to 10 cycles for samples prepared on silicon.

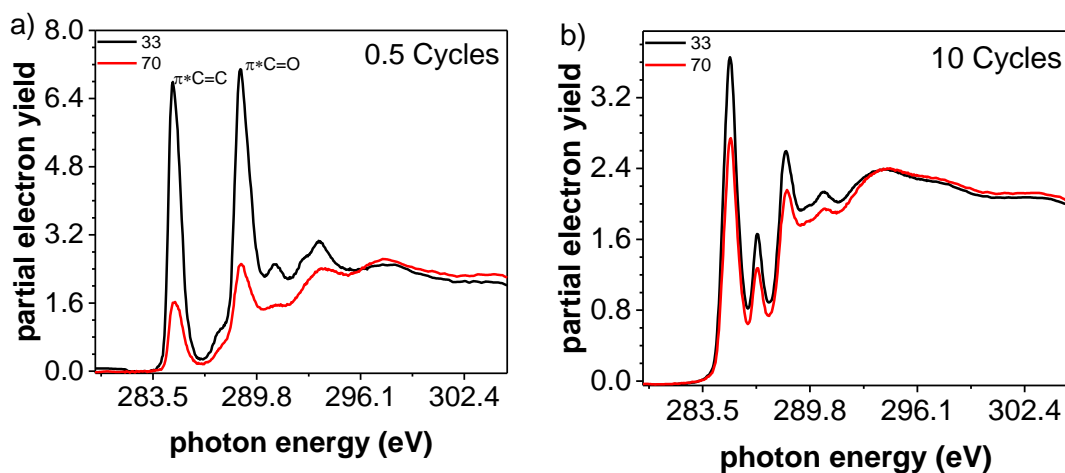


Figure 6-5. Angle dependent NEXAFS spectra of a) half cycle and b) 10 cycle mLbL samples showing the anisotropy of the antibonding C=C pi orbitals.

The C=O bond and aromatic rings are not coplanar hence more work is required to relate the two observed angles to each other by considering bond angles and torsion within the polymer molecule. This analysis is hindered by the accuracy of tilt angle obtained for the C=O bond which is influenced by changes in free acid in the film, and by the difficulty in accurately calculating the bond angles and torsion in polymer systems. NEXAFS is unable to distinguish between the trisubstituted and disubstituted rings in the polymer network while with FTIR only the disubstituted rings can accurately be probed. A direct quantitative comparison of the tilt angles provided by these two methods is only valid under the assumption the two rings are co-planar. As it is not possible to experimentally validate this assumption, computational work on the orientation of functional groups with respect to each other and a surface would provide interesting complimentary information to the work presented here.

6.3.2 Acid content

The ion exchange capacity can be defined as the milliequivalents of exchangeable ion per gram of material (meq.g⁻¹) where an equivalent is the amount of substance that can react with or displace 1 mol of H⁺. The free acid COO⁻ group is the only ionizable group in the material the only contributor to the measured IEC. If the free acid is monoprotic and assumed to be fully dissociated in the polymer network one mol of free acid will be 1eq. The iec value in meq.g⁻¹ therefore directly gives the concentration of COO⁻ groups in mmol.g⁻¹. Based on the KBr dilution factor used to prepare transmission sample the concentration of COO⁻ groups in the KBr pellet were calculated and are presented in table 6-1 below. The transmission spectrum for each sample was recorded and normalized to the thickness of the sample.

Table 6-1. The acid content of the final KBr mixture used to generate pellets for calibration curve

Sample	IEC / meq.g ⁻¹	[COO ⁻] /mmol.g ⁻¹	[COO ⁻] /mmol.g ⁻¹
8	0.116	0.116	2.3
9	0.152	0.152	3.1
10	0.215	0.215	3.8
11	0.31	0.31	8
12	0.326	0.326	8.6

Fitting of the obtained spectrum was performed using a Levenberg-Marquardt algorithm with mixed peak shapes between 1811 cm⁻¹ and 1627 cm⁻¹ to delineate the contributions of the multiple bands that overlap in this region. Peak assignments for this system were made on the basis of an extensive literature survey and experimental spectra as discussed in chapter 5.²²⁻³³ The amide I region was further modelled by fitting three bands in this region, i.e., the free acid shoulder, the amide I band and hydrogen bonded amide C=O. The aromatic ring modes that neighbor the Amide

I region overlap significantly with this region so an aromatic C=C peak was added to the fit to represent this overlap. An initial fit of sample 5 yielded the peak positions and shapes which were refined by iteration and used as shown in Figure 6-6 that shows a good fit is produced by these parameters.

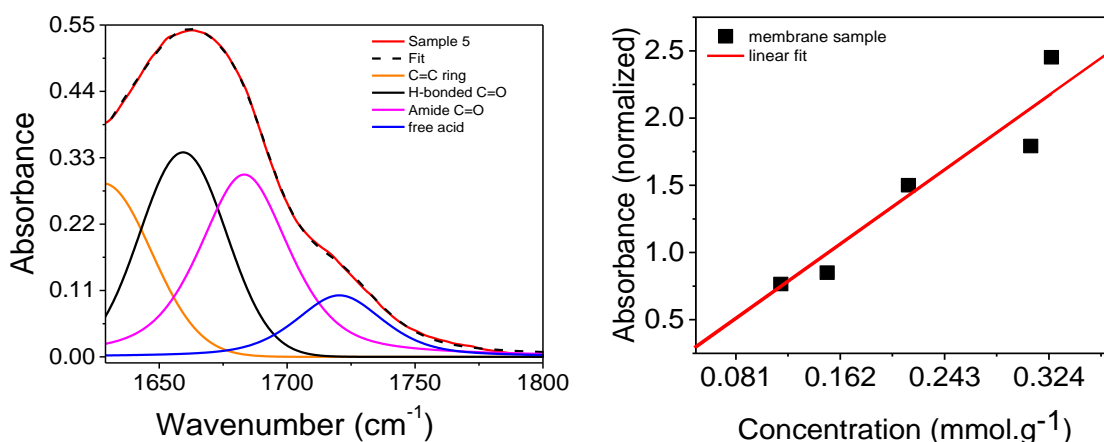


Figure 6-6. a) the FTIR spectrum of the amide I peak showing the components added into the fitting model and b) the calibration line obtained by a beers law plot of the intensity of the free acid component in a.

For fits of the remaining samples, the FWHM, and intensity for all band components except the free acid were set at initial values determined by sample 12 fitting parameters and then allowed to fit unconstrained. The peak position of the free acid peak however was held constant at 1718 cm^{-1} . The fitting parameters used for the calibration samples are provided in the supporting information. A beers law plot of the fitted free acid band component intensity as a function of COO^- concentration yielded a linear plot with the absorptivity of free acid as the gradient. The absorptivity was found to be $298 \text{ M}^{-1}\text{cm}^{-1}$ at 1728 cm^{-1} which falls within the $200 - 400 \text{ M}^{-1}\text{cm}^{-1}$ range reported in literature.³⁴

An identical fitting protocol was used for the molecular layer by layer films and the intensity of the 1718 cm^{-1} peak used to calculate the concentration of COO^- groups in the film from beers law. unlike the interface films used for calibration there was significantly more variation in peak shapes for the mLbL films. this is likely due to the interfacially polymerized films being randomly oriented throughout the film minimizing the variations in peak shape due to thickness dependent changes in the film orientation. A table of the determined acid content is provided in the supporting information and is summarized in figure 6-7.

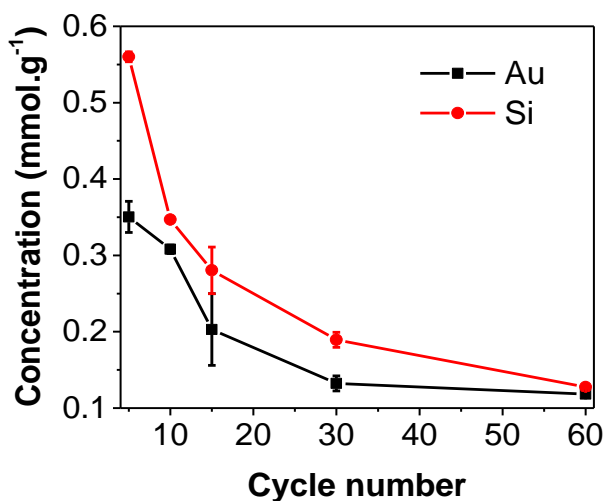


Figure 6-7. The acid content of 5 - 60 cycle mLbL films synthesized on gold and silicon samples.

In general, the acid content decreases as the cycle number increases which is indicative of increased crosslink density for higher cycle number films. The acid content in a 5 cycle film on gold was $0.3503\text{ mmol.g}^{-1}$ and 0.56 mmol.g^{-1} for a similar sample on silicon. The increased acid content on silicon substrates is likely due to the presence of water bound to silanol groups on the silicon substrate which hydrolyses TMC COOCl groups to COO^- . On gold there is evidence that the first layer of TMC is displaced by MPD such that polymerization only begins at cycle 1.5. this difference in the onset of polymerization can explain the dramatic difference at 5 cycles. As the

cycle number increases beyond 10 cycles the influence initial layer growth becomes less significant as the crosslink density of films on both substrates is very similar.

6.4 Conclusions

MLbL films show strong ordering at low cycle numbers which does not persist beyond the 15th cycle. There is evidence that the polymer is oriented close with the aromatic rings close to flat on the surface with a tilt angle of 6°, as polymerization proceeds the aromatic rings become increasingly isotropic assuming higher tilt angles closer to 40°. More work need to be done to tie the tilt angles observed for C=O and the aromatic ring together and to correlate them to NEXAFS data. The acid content of mLbL films were characterized using the intensity of the 1718cm⁻¹ free acid shoulder of the amide I peak. The absorbtivity of free acid in aromatic polyamide systems was determined from a calibration curve using interfacial polymerization samples of known acid content. The acid content range from 0.13 mmol.g⁻¹ for 60 cycles to 0.56 mmol.g⁻¹ for 5 cycles on silicon substrates. On gold however, the acid content ranged from 0.12 mmol.g⁻¹ at 5 cycles to 0.35 mmol.g⁻¹ at 12 cycles. In general, the acid content for the films synthesized on silicon was higher than that on gold possibly due to increased acid group hydrolysis on silicon. At lower cycle numbers on gold the displacement of TMC from the surface may contribute to lower acid content. At 60 cycles the difference in acid content between the two substrates diminished indicating that the mechanism of polymer growth and development of crosslinks is similar on both substrates. Since water flux increases with increased hydrophilicity of the membrane and the crosslink density can be inferred from swelling it would be interesting to carry out swelling experiments as a function of thickness in these films and correlate swelling to acid content.

6.5 Supporting Information

The wavelength dependent optical constants in the mid infrared region for the germanium³⁵ ATR crystal, evaporated gold³⁶ substrate, Silicon^{37,38}, the native oxide layer³⁹ on silicon were obtained from literature and are presented below. It is clear that silicon and native silicon oxide have absorption features in the MIR region that must be adequately considered in order to generate an accurate model. The silicon oxide layer provides the biggest challenge as it is enhanced in SO-ATR to a different extent depending on the sample thickness. We account for this by subtracting the bare silicon substrate absorbance in the experimental spectrum.

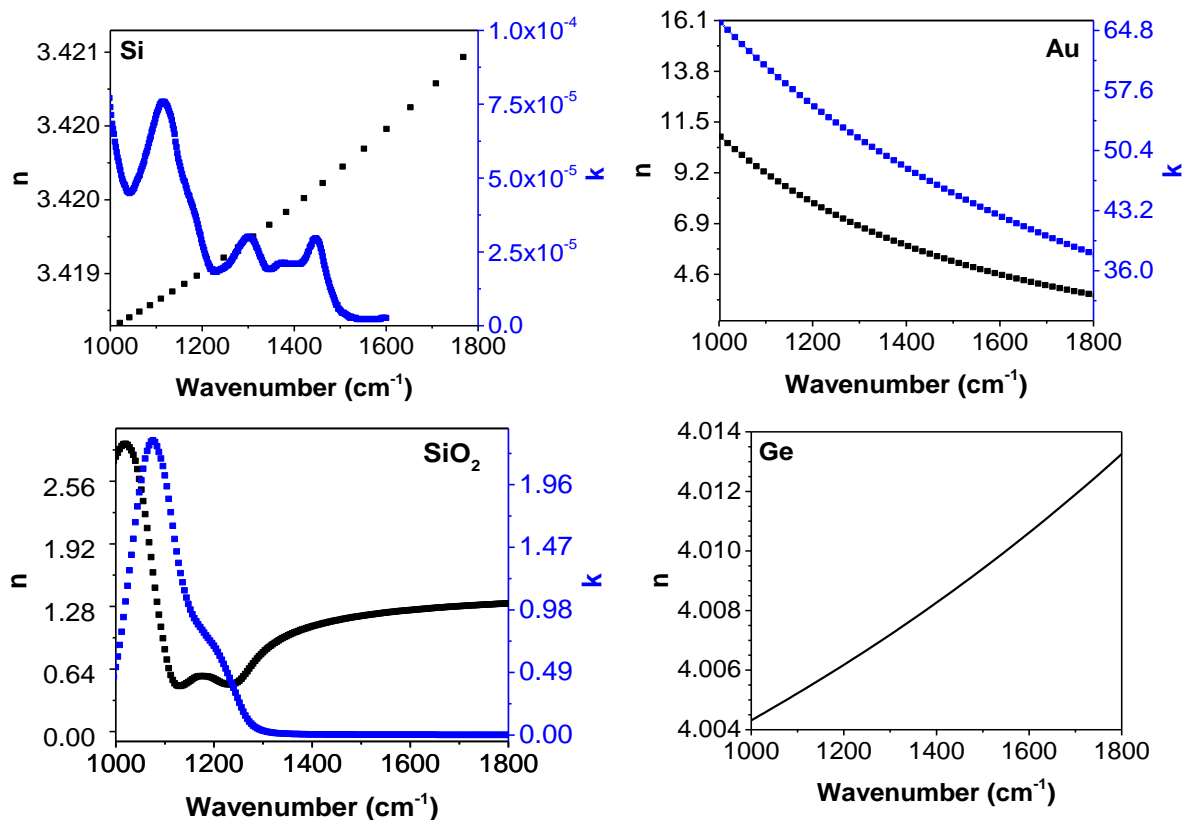


Figure 6-8. The optical constants used to compute mLbl spectra

NEXAFS experiments were carried out on mLbL films on Silicon and aminosilane derivitized silicon substrates to analyze structural anisotropy. Amino silane derivitization introduces short flexible groups to the surface that prevent the polyamide film from ordering resulting in completely isotropic polyamide films. figure 6-8 is analogous to figure 6-4 and shows NEXAFS spectra of films prepared on amino silane derivitized silicon. In contrast to samples On silicon there was no evidence of any anisotropy.

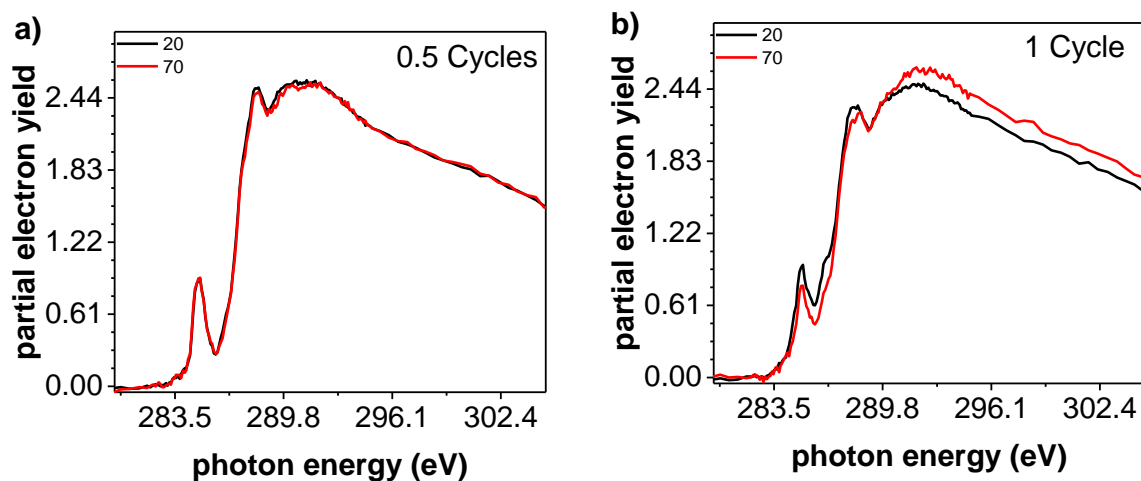


Figure 6-9. NEXAFS spectra of mLbL films synthesized on amino silane terminated silicon, this figure is analogous to figure 6-4 in the results and discussion section.

Table 6-2. The fitting parameters used to obtain unscaled intensities of the free acid component of the amide I peak.

	Position	Intensity	width	Integral	peak shape	absorbance
sample 12	1627.18	0.099847	14.58631	2.227425	92% L+G	
	1645.23	0.295197	41.73023	13.11278	0% L+G	
	1676.84	0.303571	41.54015	13.42332	0% L+G	
	1718.10	0.10588	45.00631	6.66403	66% L+G	2.4517
sample 11	1627.18	0.056614	11.69354	1.013072	* 92% L+G	
	1645.23	0.217874	44.61947	10.34813	* 0% L+G	
	1676.84	0.206394	40.94213	8.994986	* 0% L+G	
	1718.10	0.062563	45.84895	4.011929	*66%L+G	1.7912
sample 10	*1630.37	0.059354	15.11746	1.373101	* 92%L+G	
	1652.95	0.223425	44.86223	10.66954	* 0%L+G	
	1677.25	0.12507	32.8155	4.368827	* 0%L+G	
	*1718.10	0.044192	45.56735	2.816448	*66%L+G	1.5001
Sample 9	1627.18	0.129467	14.99503	2.970842	* 92% L+G	
	1650.70	0.424804	42.86462	19.38294	* 0% L+G	
	1675.86	0.326438	35.72746	12.41468	* 0% L+G	
	*1718.07	0.068811	45.383	4.367761	*66%L+G	0.8502
Sample 8	1627.18	0.181294	16.60632	4.607132	* 92%L+G	
	1648.92	0.434882	39.82769	18.43692	* 0%L+G	
	1677.46	0.399088	37.48674	15.92495	* 0%L+G	
	*1718.10	0.068275	49.42733	4.719959	*66%L+G	0.7656

The Acid content was determined from a set of three samples. Three replicate measurements were made per sample and the average acid content calculated. In general, there was little variation in absorbance within sample reading so between sample values of acid content are reported in table 6-3 below

Table 6-3. The average acid content as determined by FTIR and curve fitting

Cycle	Acid content (mmol.g ⁻¹)				
	Sample 1	Sample 2	Sample 3	Average	Deviation
Gold					
5	0.331	0.329	0.391	0.350	0.020
10	0.313	0.297	0.314	0.308	0.006
15		0.156	0.25	0.203	0.047
30	0.12	0.125	0.152	0.132	0.010
60	0.118	0.117	0.12	0.118	0.001
Silicon					
5	0.562	0.57	0.548	0.560	0.006
10	0.349	0.351	0.341	0.347	0.003
15		0.25	0.311	0.281	0.031
30	0.207	0.173	0.188	0.189	0.010
60	0.125	0.131	0.127	0.128	0.002

6.6 References

- (1) Fritzmann, C.; Löwenberg, J.; Wintgens, T.; Melin, T. State-of-the-Art of Reverse Osmosis Desalination. *Desalination* **2007**, *216* (1–3), 1.
- (2) Yan, H.; Miao, X.; Xu, J.; Pan, G.; Zhang, Y.; Shi, Y.; Guo, M.; Liu, Y. The Porous Structure of the Fully-Aromatic Polyamide Film in Reverse Osmosis Membranes. *J. Memb. Sci.* **2015**, *475*, 504.
- (3) Petersen, R. J. Composite Reverse Osmosis and Nanofiltration Membranes. *J. Memb. Sci.* **1993**, *83* (1), 81.
- (4) Johnson, P. M.; Yoon, J.; Kelly, J. Y.; Howarter, J. a.; Stafford, C. M. Molecular Layer-by-Layer Deposition of Highly Crosslinked Polyamide Films. *J. Polym. Sci. Part B Polym. Phys.* **2012**, *50* (3), 168.
- (5) Chan, E. P.; Young, A. P.; Lee, J.-H.; Stafford, C. M. Swelling of Ultrathin Molecular Layer-by-Layer Polyamide Water Desalination Membranes. *J. Polym. Sci. Part B Polym. Phys.* **2013**, *51* (22), 1647.
- (6) Tang, C. Y.; Kwon, Y. N.; Leckie, J. O. Probing the Nano- and Micro-Scales of Reverse Osmosis Membranes-A Comprehensive Characterization of Physiochemical Properties of Uncoated and Coated Membranes by XPS, TEM, ATR-FTIR, and Streaming Potential Measurements. *J. Memb. Sci.* **2007**, *287* (1), 146.
- (7) Tang, C.; Kwon, Y.; Leckie, J. Probing the Nano- and Micro-Scales of Reverse Osmosis membranes—A Comprehensive Characterization of Physiochemical Properties of Uncoated and Coated Membranes by XPS, TEM, ATR-FTIR, and Streaming Potential Measurements. *J. Memb. Sci.* **2007**, *287* (1), 146.
- (8) Tang, C. Y.; Kwon, Y.-N.; Leckie, J. O. Effect of Membrane Chemistry and Coating Layer

on Physiochemical Properties of Thin Film Composite Polyamide RO and NF Membranes. *Desalination* **2009**, 242 (1-3), 149.

- (9) Kwak, S. Y.; Jung, S. G.; Yoon, Y. S.; Ihm, D. W. Details of Surface Features in Aromatic Polyamide Reverse Osmosis Membranes Characterized by Scanning Electron and Atomic Force Microscopy. *J. Polym. Sci. Part B Polym. Phys.* **1999**, 37 (13), 1429.
- (10) Sundet, S. A. Morphology of the Rejecting Surface of Aromatic Polyamide Membranes for Desalination. *J. Memb. Sci.* **1993**, 76 (2), 175.
- (11) Hahner, G. Near Edge X-Ray Absorption Fine Structure Spectroscopy as a Tool to Probe Electronic and Structural Properties of Thin Organic Films and Liquids. *Chem. Soc. Rev.* **2006**, 35 (12), 1244.
- (12) Umemura, J.; Kamata, T.; Kawai, T.; Takenaka, T. Quantitative Evaluation of Molecular Orientation in Thin Langmuir-Biodgett Films by FT-IR Transmission and Reflection-Absorption Spectroscopy. **1990**, No. 16, 62.
- (13) Hasegawa, T. Infrared External Reflection Study of Molecular Orientation in Thin Langmuir-Blodgett Films. *J. Phys. ...* **1993**, No. 100, 9009.
- (14) Everall, N. J.; Bibby, A. Improvements in the Use of Attenuated Total Reflection Fourier Transform Infrared Dichroism for Measuring Surface Orientation in Polymers. *Appl. Spectrosc.* **1997**, 51 (8), 1083.
- (15) Gliboff, M.; Sang, L.; Knesting, K. M.; Schalnatt, M. C.; Mudalige, A.; Ratcliff, E. L.; Li, H.; Sigdel, A. K.; Giordano, A. J.; Berry, J. J.; et al. Orientation of Phenylphosphonic Acid Self-Assembled Monolayers on a Transparent Conductive Oxide: A Combined NEXAFS, PM-IRRAS, and DFT Study. *Langmuir* **2013**, 29 (7), 2166.
- (16) Parikh, A. N.; Allara, D. L. Quantitative Determination of Molecular Structure in

Multilayered Thin Films of Biaxial and Lower Symmetry from Photon Spectroscopies. I. Reflection Infrared Vibrational Spectroscopy. *J. Chem. Phys.* **1992**, 96 (2), 927.

- (17) Chalmers, J.; Griffiths, P. *Handbook of Vibrational Spectroscopy*; 2001.
- (18) Iida, K.; Imamura, Y.; Liao, C.; Nakamura, S.; Sawa, G. Evaluation of Molecular Orientation in Aromatic Polyimide Films by FT-IR Reflection Absorption Spectroscopy. *Polym. J.* **1996**.
- (19) Arnold, R.; Terfort, A.; Woll, C. INTERFACES: ADSORPTION, REACTIONS, FILMS, ASSEMBLIES, FORCES-Determination of Molecular Orientation in Self-Assembled Monolayers Using IR Absorption Intensities: The Importance of. *Langmuir* **2001**, 17 (16), 4980.
- (20) Allara, D. L.; Nuzzo, R. G. Spontaneously Organized Molecular Assemblies. 2. Quantitative Infrared Spectroscopic Determination of Equilibrium Structures of Solution-Adsorbed N-Alkanoic Acids on an Oxidized Aluminum Surface. *Langmuir* **1985**, 1 (1), 52.
- (21) Tsuboi, M.; Kubo, Y.; Akahane, K.; Benevides, J. M.; Thomas, G. J. Determination of the Amide I Raman Tensor for the Antiparallel β -Sheet: Application to Silkworm and Spider Silks. *J. Raman Spectrosc.* **2006**, 37 (1-3), 240.
- (22) Abbott, N. B.; Elliott, A. Infra-Red Spectrum and Dichroism of Crystalline Acetanilide. *Proc. R. Soc. London A Math. Phys. Eng. Sci.* **1956**, 234 (1197), 247.
- (23) Scherer, J. R. Group Vibrations of Substituted benzenes—II. Planar CH Deformations and Ring Stretching and Bending Modes of Chlorinated Benzenes. *Spectrochim. Acta* **1965**, 21 (2), 321.
- (24) Green, J. H. S. Vibrational Spectra of Benzene derivatives—VIII: M-Disubstituted Compounds. *Spectrochim. Acta Part A Mol. Spectrosc.* **1970**, 26 (7), 1523.

- (25) Bandekar, J.; Krimm, S. Vibrational Analysis of Peptides, Polypeptides, and Proteins: Characteristic Amide Bands of -Turns. *Proc. Natl. Acad. Sci.* **1979**, *76* (2), 774.
- (26) Elzein, T.; Brogly, M.; Schultz, J. Quantitative Calculation of the Orientation Angles of Adsorbed Polyamides Nanofilms. *Polymer (Guildf)*. **2003**, *44* (13), 3649.
- (27) Kwon, Y.-N.; Leckie, J. O. Hypochlorite Degradation of Crosslinked Polyamide Membranes: II. Changes in Hydrogen Bonding Behavior and Performance. *J. Memb. Sci.* **2006**, *282* (1–2), 456.
- (28) Wu, S.; Zheng, G.; Lian, H.; Xing, J.; Shen, L. Chlorination and Oxidation of Aromatic Polyamides. I. Synthesis and Characterization of Some Aromatic Polyamides. *J. Appl. Polym. Sci.* **1996**, *61* (3), 415.
- (29) Larkin, P. *Infrared and Raman Spectroscopy; Principles and Spectral Interpretation*; 2011.
- (30) Katritzky, A. R.; Sinnott, M. V.; Tidwell, T. T.; Topsom, R. D. Infrared Intensities as a Quantitative Measure of Intramolecular Interactions. V. Ortho- and Meta-Disubstituted Benzenes. Nu16 Band near 1600 Cm.-1. *J. Am. Chem. Soc.* **1969**, *91* (3), 628.
- (31) Scherer, J. R. Group Vibrations of Substituted benzenes—I. *Spectrochim. Acta* **1963**, *19* (3), 601.
- (32) Miyazawa, T.; Shimanouchi, T.; Mizushima, S. Normal Vibrations of N-Methylacetamide. *J. Chem. Phys.* **1958**, *29* (3).
- (33) Green, J. H. S.; Harrison, D. J.; Kynaston, W. Vibrational Spectra of Benzene derivatives—XII 1,3,5- and 1,2,3-Trisubstituted Compounds. *Spectrochim. Acta Part A Mol. Spectrosc.* **1971**, *27* (6), 793.
- (34) O'Reilly, J. M.; Mosher, R. A. Functional Groups in Carbon Black by FTIR Spectroscopy. *Carbon N. Y.* **1983**, *21* (1), 47.

- (35) Icenogle, H. W.; Platt, B. C.; Wolfe, W. L. Refractive Indexes and Temperature Coefficients of Germanium and Silicon. *Appl. Opt.* **1976**, *15* (10), 2348.
- (36) Olmon, R. L.; Slovick, B.; Johnson, T. W.; Shelton, D.; Oh, S.-H.; Boreman, G. D.; Raschke, M. B. Optical Dielectric Function of Gold. *Phys. Rev. B* **2012**, *86* (23), 235147.
- (37) Verleur, H. W. Determination of Optical Constants from Reflectance or Transmittance Measurements on Bulk Crystals or Thin Films. *J. Opt. Soc. Am.* **1968**, *58* (10), 1356.
- (38) Chandler-Horowitz, D.; Amirtharaj, P. M. High-Accuracy, Midinfrared ($450\text{cm}^{-1} \leq \omega \leq 4000\text{cm}^{-1}$) Refractive Index Values of Silicon. *J. Appl. Phys.* **2005**, *97* (12).
- (39) Kischkat, J.; Peters, S.; Gruska, B.; Semtsiv, M.; Chashnikova, M.; Klinkmüller, M.; Fedosenko, O.; Machulik, S.; Aleksandrova, A.; Monastyrskyi, G.; et al. Mid-Infrared Optical Properties of Thin Films of Aluminum Oxide, Titanium Dioxide, Silicon Dioxide, Aluminum Nitride, and Silicon Nitride. *Appl. Opt.* **2012**, *51* (28), 6789.

Chapter 7

Summary of Findings and Directions for Future Research

7.1 CONCLUSIONS

7.1.1 FTIR Analysis of Alignment in NAFION Thin Films at SiO₂ and Au Interfaces

There were two main outcomes of this work, firstly we gained a deeper understanding of surface overlayer ATR which despite having first been observed in the mid 90's remains poorly understood. Secondly we were able to show that the CF₃ group of NAFION which has mistakenly been interpreted by some researchers^{1,2} as co-adsorbing with the SO₃ group when NAFION is aligned on metal surface is in fact aligned with the c3 axis parallel to the surface.

When a thin film is probed in ATR geometry at high incident angle (above 60°) with a high refractive index ATR crystal and the polymer sample backed by a high refractive index or metallic substrate a signal enhancement that can be more than 10 times over transmission and RAIRS spectroscopy is observed. We termed this geometry surface overlayer ATR (SO-ATR) as a generalization of the metal overlayer ATR (MO-ATR) first reported by Ishino and Ishida in 1988.³ While Ishino and Ishida grouped MO-ATR with other SEIRA geometries and attributed the enhancement to the surface plasmon and lightning rod effects we show that this effect results mostly from an optical enhancement of the electric field by a mechanism that can be described as constructive interference. Using the SO₃ symmetric stretch of NAFION we calculated the absorbance of the peak based on the electric field intensity in x, y, and z directions. The z-component is significantly enhanced due to multiple reflections within the film between the crystal/polymer and polymer/substrate interfaces. SO-ATR spectra may at times appear confusing as the intensity does not follow the Beer-Lambert law and there are what appear to be unexplained

peak shifts when the thickness is varied. We have demonstrated that the non-linearity of the SO-ATR intensities with thickness and the peak shifts can both be explained by the enhancement of the z-component being dependent on the distance between the crystal/polymer and polymer/substrate interfaces. The intensity of the evanescent wave decays exponentially as a function of distance from the crystal polymer interface hence the further the polymer/substrate interface, the weaker the reflected field amplitude and the lower the enhancement until eventually the substrate is so far that no enhancement is observed. This explains the non-linearity. The peak shifts are explained by the changing polarization associated with the z-component enhancement. In thin films the electric field is almost exclusively z-polarized while for thicker films the contributions of x and y components become more important.

The orientation of the NAFION thin films on planar substrates has been the focus of much interest and has been studied using a variety of vibrational tools ranging from SERS⁴ to SFG.⁵ SO-ATR allowed us to study the orientation of spin cast NAFION films on silicon and directly compare the results to those obtained on gold substrates. Based on the similarity of the spectral features we determined there is little difference in the orientation on both substrates which implies that the orientation was imparted by the spin casting process. As the spin cast film became thinner we observed a peak shift from $\sim 1220\text{ cm}^{-1}$ to 1259 cm^{-1} . As film thickness decreases and the proportion

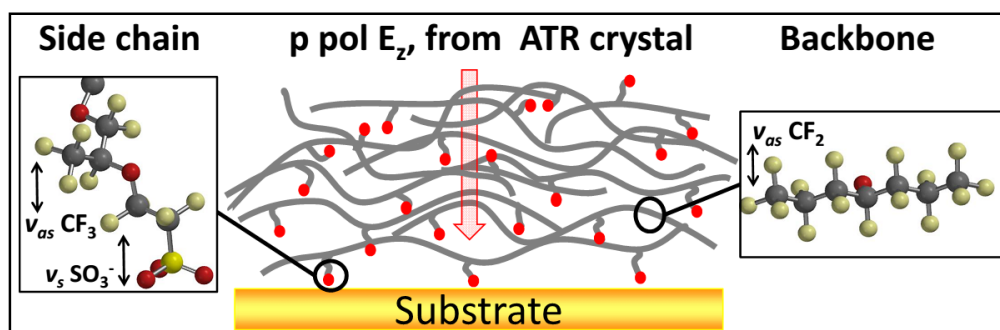


Figure 7-1. Ordered conformation of NAFION® on surface for thin films where the backbone $\nu_{as}(\text{CF}_2)$, side chain $\nu_s(\text{SO}_3^-)$ and $\nu_{as}(\text{CF}_3)$ dipole changes are in the plane of the p-polarized z component of the evanescent wave.

of ordered molecules increases as does the z-polarization of the incident beam resulting in an increase in the absorbance of functional groups with dipoles aligned in the z axis. For the CF_3 group in NAFION the asymmetric stretch (1254 cm^{-1}) dipole change is perpendicular to the C3 axis of the functional group while the symmetric stretch (1232 cm^{-1}) dipole change is parallel to the C3 axis. Similarly, for the backbone CF_2 groups the asymmetric stretch dipole change is perpendicular to the longitudinal axis of the backbone while the symmetric stretch dipole change perpendicular to the asymmetric stretch and along the C2 axis. NAFION is oriented at the substrate-polymer film interface as pictured in figure 7-1 resulting in higher absorbance values with p-polarized light. NAFION is likely to associate with surfaces via the $-\text{SO}_3^-$ groups causing a reduction in backbone motion and alignment of the backbone parallel to the surface with backbone $\text{vas}(\text{CF}_2)$ dipole changes perpendicular to the surface. Side chain ordering results in $\text{vas}(\text{CF}_3)$ dipole changes being aligned perpendicular to the surface. The overall changes in absorbance maximum of the 1220 cm^{-1} and 1140 cm^{-1} peaks results from increased absorbance of the $-\text{CF}_2$, and $-\text{CF}_3$ asymmetric stretch bands and a decreased absorbance of the $-\text{CF}_2$ and $-\text{CF}_3$ symmetric stretch bands.

7.1.2 Understanding the Fingerprint region of aromatic polyamide

We studied the fingerprint region of aromatic polyamide films synthesized by molecular layer by layer deposition and interfacial polymerization in order to assign the major peaks found in this region and interpret changes in this region as a result of sample preparation and hydration.

The fingerprint region of aromatic polyamide membranes is a convolution of aromatic modes and amide vibrations. With the exception of the amide I peak and the amide II peak the spectrum is dominated by aromatic ring modes. We assigned the peak at 1492 cm^{-1} to the B1 Vibration of the bi-substituted aromatic ring that originates from m-phenylenediamine monomer. The significance of this peak assignment is that this peak is unconvoluted and hence can be used

as a diagnostic peak either for quantifying the MPD incorporated into the polymer network or to determine the orientation of the MPD ring. We also demonstrated that the 1610 cm^{-1} peak belongs predominantly to the stretching bending vibration of the tri-substituted ring that originates from the trimesic acid monomer with strong contributions from a similar stretching bending vibration of the MPD derived aromatic ring. The significance of this peak assignment is that this peak has been used in studies to determine the chloride degradation mechanism of aromatic polyamide based reverse osmosis membranes which can either occur by aromatic ring attack via Orton rearrangement or by chlorination of the amide group nitrogen. Our assignment implies that disappearance of this peak during chloride attack can only be ascribed to the breaking of aromaticity during Orton rearrangement. Some researchers have speculated that this peak is predominantly due to hydrogen bonded amide C=O and its disappearance during chloride attack results from the disruption of hydrogen bonding when N-H is converted to N-Cl.⁶ Our humidity studies with polyamide films revealed that the 1610 cm^{-1} peak is only slightly affected by hydration compared to the amide I peak (1672 cm^{-1}) and amide II peak (1546 cm^{-1}). This observation led us to conclude that the 1610 cm^{-1} peak has only minor contributions from hydrogen bonded C=O.

The water uptake characteristics of RO membranes are directly tied to their performance as the swelling often affects the water flux.⁷ We exposed both mLbL films and Interfacially polymerized films to humidity and observed changes in the polymer FTIR spectrum during hydration. We proposed that the 1243 cm^{-1} peak which belongs to the amide N-H bend and C-N stretch is perhaps the best peak in the fingerprint region to monitor hydration as the neighboring vibrations belong to the aromatic rings and their associated C-H modes which are relatively inert to the effects of hydration.

We used FTIR and XPS to study the growth of the initial layers of mLbL films on gold and silicon substrates. We observed that on silicon the first amide bonds begin to form at the first cycle with the introduction of MPD while on gold MPD displaces TMC on the substrate surface and only

at cycle 1.5 do amide bonds begin to form. The initial polymer network on both substrates is loosely crosslinked resulting in a substantial amount of unreacted carboxylic groups for low cycle number as signified by absorbance of the free acid (1710 cm^{-1}) shoulder on the amide I peak. As the cycle number increases the absorbance of the free acid shoulder relative to the amide I peak decreases implying that the crosslink density increases as the film increases in thickness. We demonstrated that the solvent used to rinse excess monomer between each half cycle has a significant impact on the polymerization reaction with consistently thicker films being observed when IPA is used instead of acetone. We suggest that the reason for this difference is that acetone is a better solvent and removes most of the excess monomer while IPA leaves some excess monomer which forms short oligomer chains which become entangled with the growing polymer layer thus making the film thicker yet less cross-linked.

7.1.3 The acid content and Orientation of molecular Layer by Layer polyamide films on silicon and gold substrates

It has been established that the amount of free acid affects the surface charge and flux of reverse osmosis membranes.⁷ We developed a fitting protocol to estimate the amount of free acid present in layer by layer films synthesized on gold and silicon substrates by first generating a calibration curve based on interfacially polymerized films of known acid concentration. We deconvoluted the amide I region into the Amide C=O, Hydrogen bonded C=O, free acid C=O and aromatic C=C bands. Using the Levenberg-Marquardt algorithm we fixed the free acid band at 1718 cm^{-1} with a 66% Lorentz peak shape and allowed the intensity and peak width to vary. In general we observed more free acid for samples prepared on silicon than those prepared on gold. The difference in acid content between substrates decreased with increasing cycle number because at low cycle numbers polymerization begins at the first cycle on silicon while on gold it does not

begin until cycle 1.5. We believe that surface silanol groups on silicon substrates may result in a thin hydration layer on silicon substrates resulting in the hydrolysis of trimesic chloride to trimesic acid resulting in a slightly higher acid content for lower cycle numbers. For higher cycle numbers (above 30 cycles) there is very little difference between the acid content on both surfaces indicating that the growth and crosslinking on both substrates is similar and this is likely to result in similar surface charge, flux and salt rejection.

We utilized spectral simulation coupled with RAIRS and SO-ATR measurements to obtain orientation information for mLbL films synthesized on gold and silicon substrates. While this method is in most cases challenging and highly reliant on obtaining a good quality spectrum in the case of the poly(amide) LBL system it is the only method that is applicable. In this study we compared diagnostic modes in the RAIRS or SO-ATR spectrum to a model isotropic film of identical thickness on the same substrate. The model spectra were generated from the optical constants of the PA material by modeling a three-layer system that included the substrate of interest and either air or the ATR crystal. Simulation of the wavelength dependent interaction of light with this three-layer system yielded the total reflectance of the system which was processed in exactly the same manner as a physical IR experiment to produce a model spectrum. The amide I mode was selected as a diagnostic peak because it is well researched due to its relevance in protein research, hence the orientation of the dipole is well understood and its effect on secondary structure is also widely reported. The tilt angle of amide C=O groups with respect to the surface normal were determined from the 1668 cm^{-1} peak. The orientation of the transition dipole moment for the $\nu(\text{C=O})$ stretch resulting in the 1668 cm^{-1} peak is 18° from the plane of the C=O bond plane. By comparing the simulated isotropic RAIRS absorbance to the experimental RAIRS absorbance of this C=O peak we were able to deduce the tilt angle of this group in the poly(amide) system. The tilt angle was estimated to range between 16° and 18° on gold substrates which seems consistent with the 18° angle observed on silicon for 10 cycles.

The MPD ring mode at 1498 cm^{-1} is attributed solely to two MPD ring modes which are coplanar in the plane of the MPD aromatic ring which suggests that changes in orientation affect them equally. The contribution of the C-N mode overlap was considered minor and assumed not significantly affect the absorbance. For amide C=O and MPD aromatic rings there is a marked transition around 15 cycles where it seems there is one regime of ordering at 5 and 10 cycles which rapidly dissipates at 30 and 60 cycles. While the tilt angles for lower cycle numbers are in close agreement, the angles for cycles above 10 cycles vary significantly for both C=O and MPD on both gold and silicon. The calculated angles were in good agreement for low cycle numbers on both gold and silicon, with silicon in general have slightly higher calculated tilt angles for both functional groups. The MPD ring while not lying completely flat on the surface is on average tilted between 16° - 18° on the surface. The ordering of these films appear to not persist beyond 10 layers on both gold and silicon as indicated by the wide variance in tilt angles for the 30 and 60 cycle samples.

7.2 Future Work

7.2.1 In situ structure and composition changes

Aside from elucidating the basic interactions between ionomers and surfaces, we want to understand the function of the ionomer layer in an electrochemical environment. Most literature on potential-dependent ionomer behavior has been directed at potential-dependent hydration/dehydration cycles.^{8,9} The most widely used method to study the ionomer-electrode interface is ATR- surface enhanced infrared absorption (ATR-SEIRA) in which a subtractively normalized interfacial FTIR spectroscopy (SNIFTIRS) spectrum is obtained in the Kretschmann configuration.¹⁰⁻¹² The SNIFTIRS method is convenient in detecting adsorbed species as it is only sensitive to a monolayer or two above the electrode surface and also allows for in-situ analysis to be performed under electrochemical conditions.

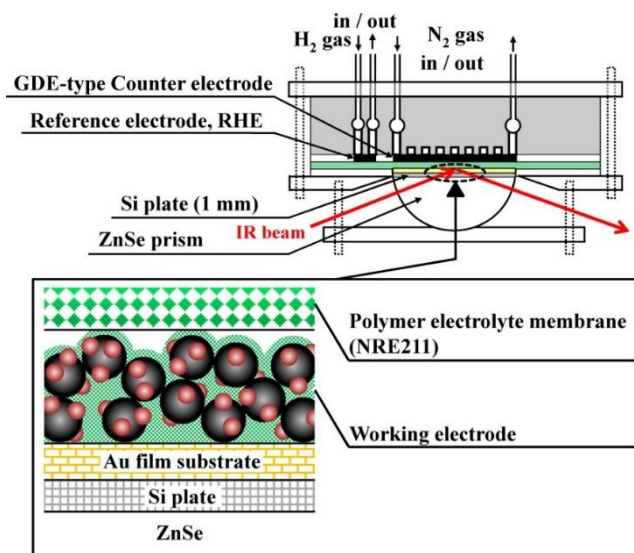


Figure 7-2. Experimental setup of the MEA-type cell for the in situ ATR-FTIR measurements at the NAFION–Pt/C and Pt₃Co/C

Watanabe, et al. have used this method to study the effect of hydration on NAFION conductivity and adsorption of surface species on a gold electrode and concluded the SO₃⁻ group co-adsorbs with

the side chain ether groups as potential increases.^{11,13} The experimental geometry used in Watanabe's experiments is shown in figure 7-2. Kendrick et al used in-operando PM-IRRAS to observe the ionomer in the catalyst layer of a fuel cell while in use.² The experiments conducted by Watanabe were on bulk membranes and it would be extremely valuable to conduct similar experiment's on thin films which represent a more realistic representation of fuel cell construction. The experiments of Kendrick would ideally provide the realistic representation that the Experiments of watanabe lack but suffer the pitfall that it is more difficult to precisely control the experimental parameters in operando and the design of a specialized fuel cell that places the catalyst layer in the IR beam path is technically challenging.

The Kretschmann geometry has been successfully used to determine the mechanism for potential-dependent adsorption of charged small molecules and is the most likely approach to yield surface specific information about the absorption process during electrocatalytic events.^{14,15} For example the SEIRAS studies of the Pt/NAFION interface in HClO₄ aqueous solutions under the potential-controlled conditions conducted by Osawa revealed the potential-dependent adsorption/orientation of the -SO_3^- groups of the NAFION film. The -SO_3^- groups are more or less restricted in their vibration mode due to the interaction with water molecules, upon adsorption to Pt surface. It suggests clearly that the -SO_3^- groups are responding to the electrode potential like single ions, due to flexibility of the pendant side chains of the ionomer membrane.¹⁶ While NAFION is the benchmark catalyst layer ionomer it is thought that the sulfonate group preferred adsorption under operating potential may block catalytic sites hence reducing catalytic activity.^{17,18}

Hickner et al proposed a variety of sulfonated alternative polymer systems for proton

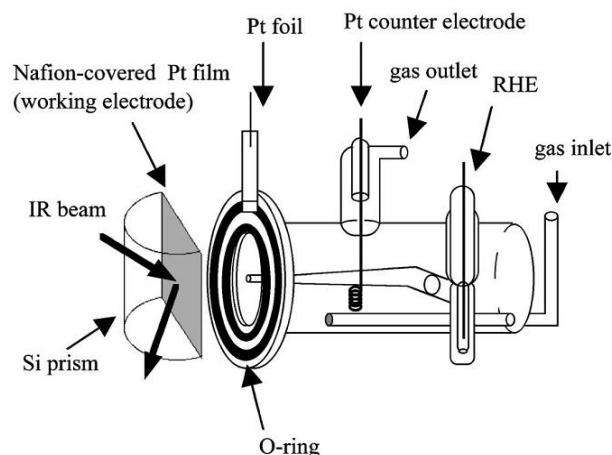


Figure 7-3. Spectroelectrochemical cell used in SEIRA experiments ¹⁶
 exchange membrane systems, including poly(arylene) ethers and post sulfonation existing polymers.¹⁹ The charge density of them sulfonate group in these alternative systems would undoubtedly be different from NAFION and Yeh et al in computational work have demonstrated that the electronegativity of the sulfonate group directly affects the adsorption potential.²⁰ Potential dependent SEIRA experiments similar to those conducted by Osawa with these alternative materials could support the computational conclusions of Yeh et al and lead to the development of an ionomer that does not specifically adsorb to the electrode surface and block catalytic sites at fuel cell operating potentials. Not much spectroelectrochemical research has been conducted on cationic ionomers which is a hot topic for anion exchange membrane fuel cells hence complementary experiments with quaternary ammonium functionalized AEM polymers would help elucidate the fundamental in absorption characteristics and draw parallels and distinctions with PEM polymers.

The geometry used to carry out such experiments is shown in figure 7-3. As with SERS, SEIRA experiments are particularly sensitive to the preparation of the working electrode and for these experiments to be successful both the thickness and roughness of the electrode must be precisely controlled.^{21,22} As with all ATR experiments the acquisition of good quality spectra is contingent on there being intimate contact between the thin polymer film and the ATR element. It

is therefore important to ensure the polymer film does not delaminate from the ATR crystal while submerged in the electrolyte solution. While these challenges complicate experimental design and have made electrochemical SEIRA a niche characterization method, the information it can provide would be a valuable addition to our knowledge about the behavior of ionomer films at electrode surfaces.

7.2.2 Analyzing the hydrogen bonding network in polymer thin films

We have been able to use the HOD FTIR peak as probe for studying the hydrogen bonding in proton exchange and neutral polymers.²³ This peak is characteristic of different hydrogen

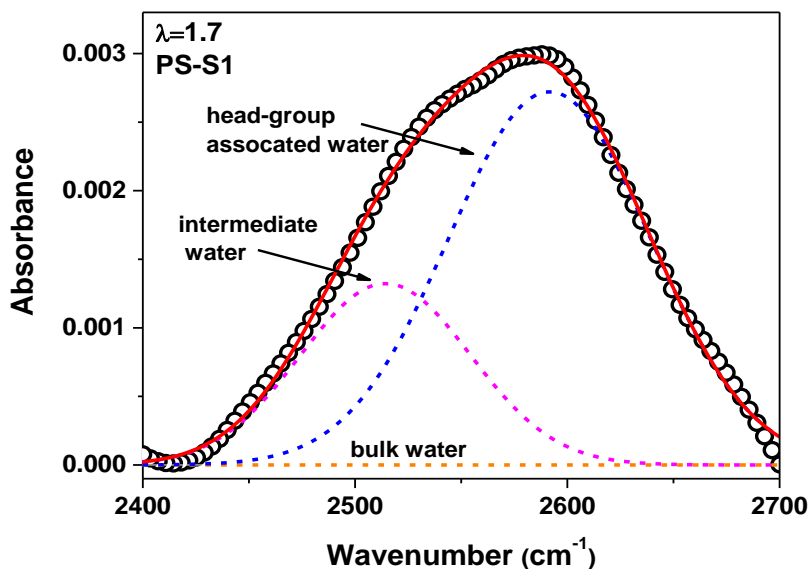


Figure 7-4. Figure 7-4 The OD stretch deconvolution of PS-S1 at a λ of 1.7. Hydration was obtained for each membrane by introducing the sample to 10% HOD vapor at 30% relative humidity.²³

bonding populations within the membrane and can be deconvoluted into headgroup associated, intermediate and bulk states of water as shown in figure 7-4. When dilute HOD is sorbed into a

proton exchange membrane, the OD stretch peak shifts based on the microenvironment that water encounters within the nanophase separated structure of the material.^{23–25} While we have had success using this probe for micron thick membranes no complementary work has been reported for polymer films below 100 nm thick. Davis and Stafford investigated the water vapor diffusion in a NAFION thin film using time-resolved in situ polarization modulation infrared reflection absorption spectroscopy (PM-IRRAS). They measured the steady state effective diffusion coefficients of both hydrogenated (H_2O) and deuterated (D_2O) water by switching between the two penetrants.²⁶ Similar PM-IRRAS studies can be conducted on mLbL samples where RH controlled experiments can provide complimentary information to the XRR data that current swelling models are based on.²⁷ In our preliminary PM-IRRAS experiments we observed the hydration of a 30 Cycle mLbL film upon hydration with vapor from a 10% mol solution of HOD in water. While converting PM-IRRAS intensity to absorbance values^{28,29} is not trivial it will be a worthwhile task to obtain quantitative swelling values. Preliminary data reveals that the OD region of mLbL polyamides is likely to be less complicated than that of NAFION although the contributions of N-D exchange (2400 cm^{-1}) in this region will have to be deconvoluted.

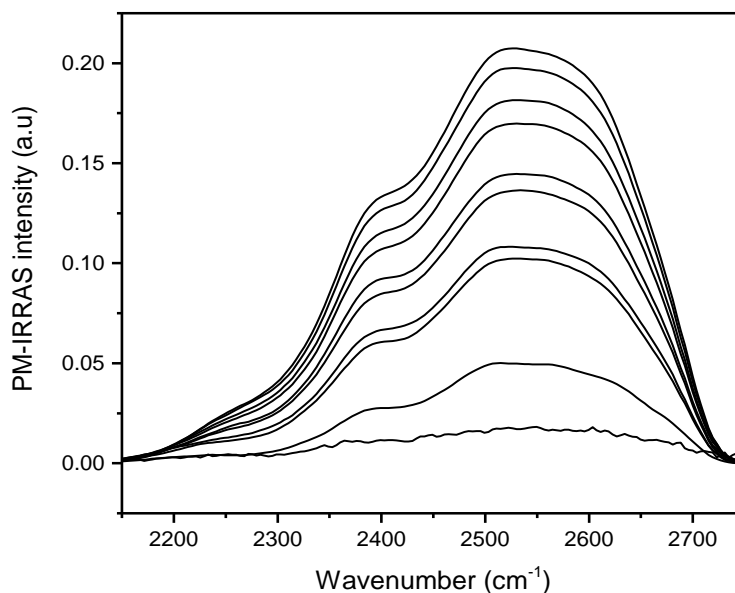


Figure 7-5. OD region of 30 cycle mLbL films exposed to 10 mol % HOD water vapor at 90% relative humidity.

7.2.3 Azides as an alternate probe for HOD in thin polymer films

Azides (N_3^-) have been used to probe the hydrated region of reverse micelles. The azide ion is an attractive probe because it is small and has a strong and narrow vibrational absorption at $\sim 2000 \text{ cm}^{-1}$ which is very sensitive to the local environment. The hydrogen bonding and pore sizes for reverse micelles created from anionic, cationic and neutral surfactants were studied using an azide probe by Zhong et al.³⁰ The FTIR peak positions of the azide probe as a function of ω (water/headgroup) were reported and in all three cases, as ω increases the azide peak position shifts closer to the bulk peak position of 2048 cm^{-1} because as the micelle grows larger, there is more bulk-like water present. In the anionic micelle (AOT) the peak position is blueshifted from bulk-like water

but in the neutral (Igepal) and cationic (CTAB) micelles, the peak is redshifted by a factor proportional to the headgroup charge ($\sim 16 \text{ cm}^{-1}$ and 36 cm^{-1} respectively).

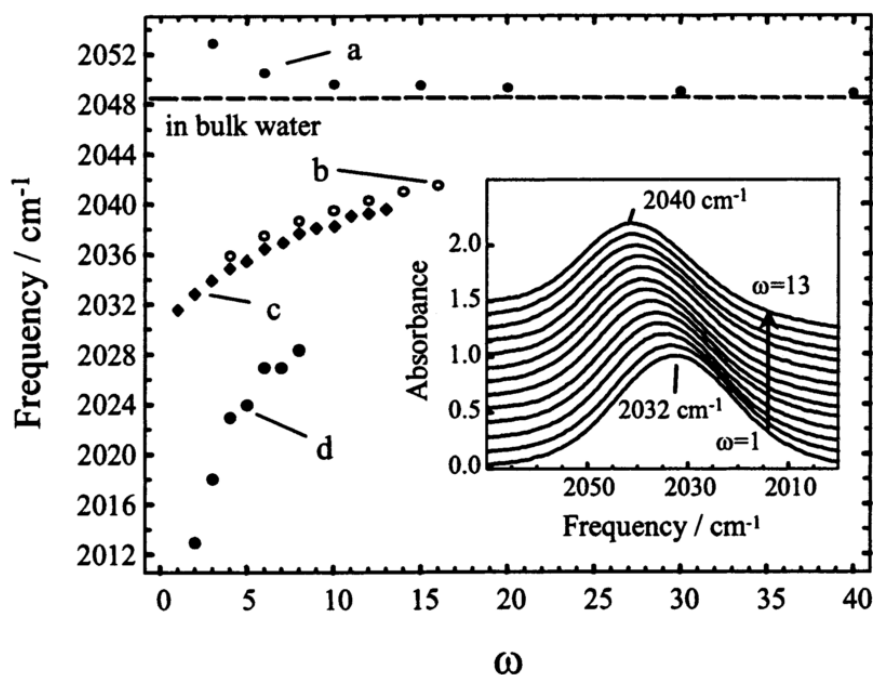


Figure 7-6. The antisymmetric stretching mode of the azide ion as a function of ω in reverse micelles formed using (a) AOT (b) Igepal and (c) CTAB surfactants. The dashed line is the frequency of an azide in bulk water.³⁰

We have recently performed preliminary experiments on quaternized comb-shaped poly(2,6-dimethyl-1,4-phenylene oxide) (QA-PPO) polymers with 0, 6, 10, and 16 carbon alkyl

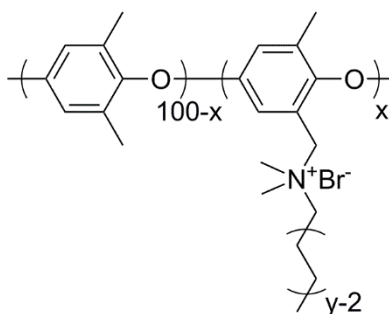


Figure 7-7. Figure 7-7 Structure of QA-PPO samples discussed in the text where x is the degree of functionalization and $y-2$ is the number of carbons after the quaternary ammonium group

side chains (Figure 7-7) to assess the feasibility of using the azide ion to probe the hydrogen bonding anion exchange membrane materials.

When the peak position is plotted as a function of ω as in the case of reverse micelles, a plot analogous to figure 7-6 is obtained which shows the expected redshift in the azide asymmetric stretch, figure 7-8. It is reasonable to believe the charge on the quaternary ammonium group is

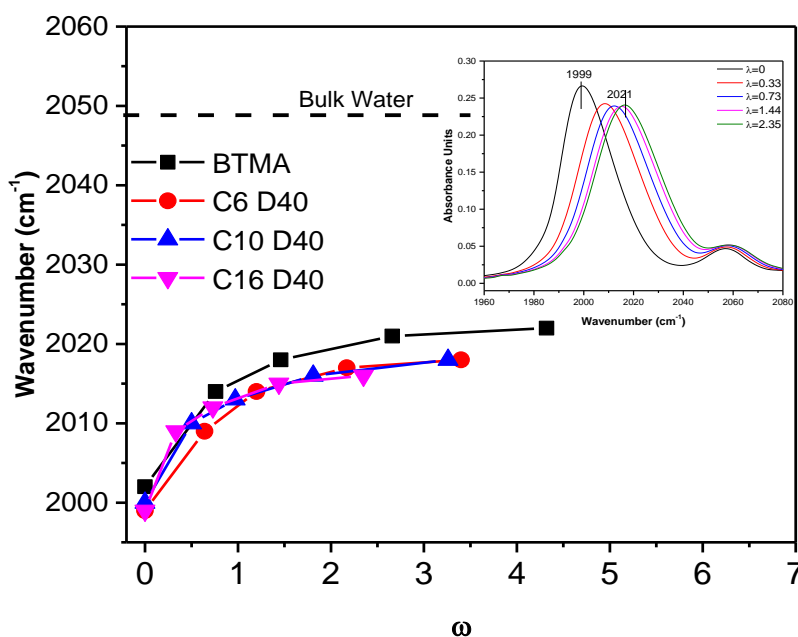


Figure 7-8. Peak position of azide asymmetric stretch as a function of hydration number for QA ppo sample of different cross linker length. This plot is analogous to fig 7-6 for reverse micelles the insert shows the spectrum of BTMA as the hydration number increases

affected by the length of the alkyl chain attached to it, however this is unlikely to be the sole cause for the difference in the shift observed between BTMA and the longer alkyl chain polymers. As the sidechain length increases it is possible that steric effects dictate or at the very least influence the accessibility of the QA group to incoming water molecules.

RH-QCM experiments³¹ show a close correlation between the trend in swelling behavior between samples of different side chain length and the redshift observed in the azide asymmetric stretch, particularly at higher RH values. This close correlation seems to confirm the potential to use the azide peak as a qualitative diagnostic peak to determine trends in water uptake. While this

initial data is very promising the effect of both the quaternary ammonium group counter ion and the azide counter ion must be considered. There is evidence in literature that the azide counter ion does affect the peak position of the asymmetric stretch and our experiments have also confirmed that the identity QA group counter ion can have a significant effect.

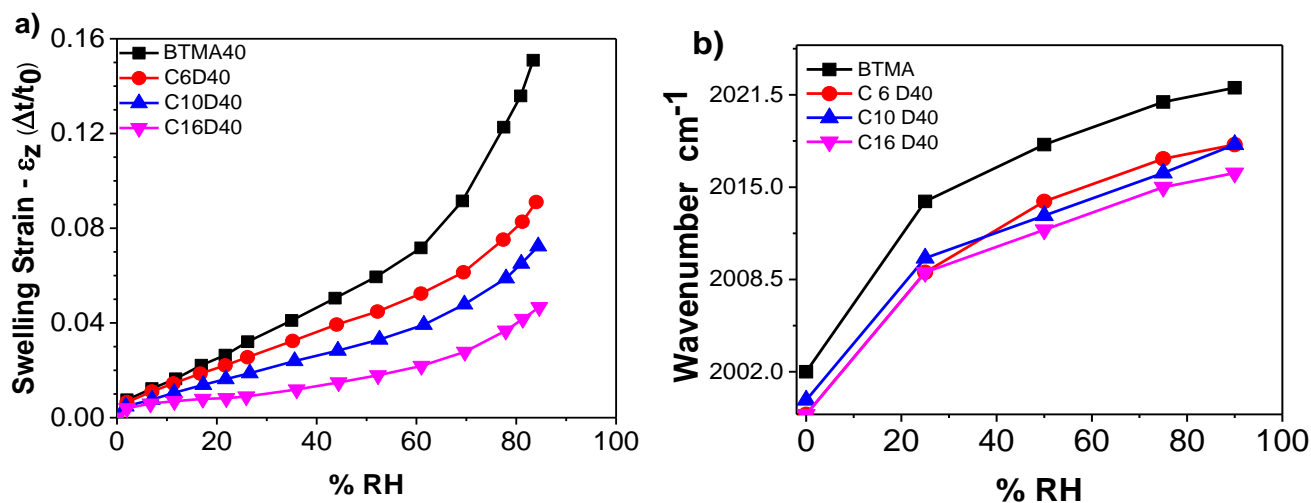


Figure 7-9. a) Swelling strain measured by QCM as a function of humidity³¹ and b) azide asymmetric stretch measured as a function of relative humidity.

7.3 References

- (1) Kendrick, I.; Yakaboski, A.; Kingston, E.; Doan, J.; Dimakis, N.; Smotkin, E. S. Theoretical and Experimental Infrared Spectra of Hydrated and Dehydrated NAFION. *J. Polym. Sci. Part B Polym. Phys.* **2013**, *51* (18), 1329.
- (2) Kendrick, I.; Kumari, D.; Yakaboski, A.; Dimakis, N.; Smotkin, E. S. Elucidating the Ionomer-Electrified Metal Interface. *J. Am. Chem. Soc.* **2010**, *132* (49), 17611.
- (3) Ishino, Y.; Ishida, H. Grazing Angle Metal-Overlayer Infrared ATR Spectroscopy. *Appl. Spectrosc.* **1988**, *42* (7), 1296.
- (4) Zeng, J.; Jean, D.; Ji, C.; Zou, S. In Situ Surface-Enhanced Raman Spectroscopic Studies of NAFION Adsorption on Au and Pt Electrodes. *Langmuir* **2011**, *28* (1), 957.
- (5) Yagi, I.; Inokuma, K.; Kimijima, K.; Notsu, H. Molecular Structure of Buried Perfluorosulfonated Ionomer/Pt Interface Probed by Vibrational Sum Frequency Generation Spectroscopy. *J. Phys. Chem. C* **2014**, *118* (45), 26182.
- (6) Kang, G.-D.; Gao, C.-J.; Chen, W.-D.; Jie, X.-M.; Cao, Y.-M.; Yuan, Q. Study on Hypochlorite Degradation of Aromatic Polyamide Reverse Osmosis Membrane. *J. Memb. Sci.* **2007**, *300* (1-2), 165.
- (7) Childress, A. E.; Elimelech, M. Relating Nanofiltration Membrane Performance to Membrane Charge (electrokinetic) Characteristics. *Environ. Sci. Technol.* **2000**, *34* (17), 3710.
- (8) Kunimatsu, K.; Bae, B.; Miyatake, K.; Uchida, H.; Watanabe, M. ATR-FTIR Study of Water in NAFION Membrane Combined with Proton Conductivity Measurements during Hydration/dehydration Cycle. *J. Phys. Chem. B* **2011**, *115* (15), 4315.
- (9) Kaim, W.; Fiedler, J. Spectroelectrochemistry: The Best of Two Worlds. *Chem. Soc. Rev.* **2009**, *38* (12), 3373.
- (10) Ashley, K.; Pons, S. Infrared Spectroelectrochemistry. *Chem. Rev.* **1988**, *88* (4), 673.
- (11) Hanawa, H.; Kunimatsu, K.; Watanabe, M.; Uchida, H. In Situ ATR-FTIR Analysis of the Structure of NAFION–Pt/C and NAFION–Pt₃Co/C Interfaces in Fuel Cell. *J. Phys. Chem. C* **2012**, *116* (40), 21401.
- (12) Mozo, J.; Dominguez, M. Development of a Spectroelectrochemistry Assembly(SNIFTIRS) Based on a Commercial Spectrophotometer. Test with the Ferrocyanide/Ferricyanide Redox. *Electroanalysis* **2000**, 767.
- (13) Kunimatsu, K.; Yoda, T.; Tryk, D. A.; Uchida, H.; Watanabe, M. In Situ ATR-FTIR Study of Oxygen Reduction at the Pt/NAFION Interface. *Phys. Chem. Chem. Phys.* **2010**, *12* (3), 621.

- (14) Ataka, K.; Yotsuyanagi, T.; Osawa, M. Potential-Dependent Reorientation of Water Molecules at an Electrode / Electrolyte Interface Studied by Surface-Enhanced Infrared Absorption Spectroscopy. **1996**, 3654 (95), 10664.
- (15) Chen, Y. X.; Miki, A.; Ye, S.; Sakai, H.; Osawa, M. Formate, an Active Intermediate for Direct Oxidation of Methanol on Pt Electrode. *J. Am. Chem. Soc.* **2003**, 125 (13), 3680.
- (16) Ayato, Y.; Kunimatsu, K.; Osawa, M.; Okada, T. Study of Pt Electrode/NAFION Ionomer Interface in HClO₄ by In Situ Surface-Enhanced FTIR Spectroscopy. *J. Electrochem. Soc.* **2006**, 153 (2), A203.
- (17) Kocha, S. S.; Zack, J. W. J.; Alia, S. M. S.; Neyerlin, K. C.; Pivovar, B. S. Influence of Ink Composition on the Electrochemical Properties of Pt/C Electrocatalysts. *ECS Trans.* **2013**, 50 (2), 1475.
- (18) Masuda, T.; Ikeda, K.; Uosaki, K. Potential-Dependent Adsorption/Desorption Behavior of Perfluorosulfonated Ionomer on a Gold Electrode Surface Studied by Cyclic Voltammetry, Electrochemical Quartz Microbalance, and Electrochemical Atomic Force Microscopy. *Langmuir* **2013**, 29 (7), 2420.
- (19) Hickner, M. A.; Ghassemi, H.; Kim, Y. S.; Einsla, B. R.; McGrath, J. E. Alternative Polymer Systems for Proton Exchange Membranes (PEMs). *Chem. Rev.* **2004**, 104 (10), 4587.
- (20) Yeh, K.-Y.; Restaino, N. a.; Esopi, M. R.; Maranas, J. K.; Janik, M. J. The Adsorption of Bisulfate and Sulfate Anions over a Pt(111) Electrode: A First Principle Study of Adsorption Configurations, Vibrational Frequencies and Linear Sweep Voltammogram Simulations. *Catal. Today* **2013**, 202 (0), 20.
- (21) Miyake, H.; Ye, S.; Osawa, M. Electroless Deposition of Gold Thin Films on Silicon for Surface-Enhanced Infrared Spectroelectrochemistry. *Electrochem. commun.* **2002**, 4 (12), 973.
- (22) Delgado, J. M.; Orts, J. M.; Rhodes, A. A Comparison between Chemical and Sputtering Methods for Preparing Thin-Film Silver Electrodes for in Situ ATR-SEIRAS Studies. *Electrochim. Acta* **2007**, 52 (14), 4605.
- (23) Smedley, S. B. Water Hydrogen Bonding In Proton Exchange and Neutral Polymers, Pennsylvania State University, 2015.
- (24) Black, S. B.; Chang, Y.; Bae, C.; Hickner, M. A. FTIR Characterization of Water–Polymer Interactions in Superacid Polymers. *J. Phys. Chem. B* **2013**, 117 (50), 16266.
- (25) Smedley, S. B.; Chang, Y.; Bae, C.; Hickner, M. A. Measuring Water Hydrogen Bonding Distributions in Proton Exchange Membranes Using Linear Fourier Transform Infrared Spectroscopy. *Solid State Ionics* **2015**, 275, 66.
- (26) Davis, E. M.; Stafford, C. M.; Page, K. A. Elucidating Water Transport Mechanisms in NAFION Thin Films. *ACS Macro Lett.* **2014**, 3 (10), 1029.

- (27) Chan, E. P.; Young, A. P.; Lee, J.-H.; Stafford, C. M. Swelling of Ultrathin Molecular Layer-by-Layer Polyamide Water Desalination Membranes. *J. Polym. Sci. Part B Polym. Phys.* **2013**, *51* (22), 1647.
- (28) Zawisza, I.; Lachenwitzer, A.; Zamlynny, V.; Horswell, S. L.; Goddard, J. D.; Lipkowski, J. Electrochemical and Photon Polarization Modulation Infrared Reflection Absorption Spectroscopy Study of the Electric Field Driven Transformations of a Phospholipid Bilayer Supported at a Gold Electrode Surface. *Biophys. J.* **2016**, *85* (6), 4055.
- (29) Zamlynny, V.; Zawisza, I.; Lipkowski, J. PM FTIRRAS Studies of Potential-Controlled Transformations of a Monolayer and a Bilayer of 4-Pentadecylpyridine, a Model Surfactant, Adsorbed on a Au(111) Electrode Surface. *Langmuir* **2003**, *19* (1), 132.
- (30) Zhong, Q.; Steinhurst, D. A.; Carpenter, E. E.; Owrutsky, J. C. Fourier Transform Infrared Spectroscopy of Azide Ion in Reverse Micelles. *Langmuir* **2002**, No. 11, 7401.
- (31) Kushner, D. Thin Film Dynamics in Ion Containing Polymers, Pennsylvania State University, 2016.

VITA

Tawanda J. Zimudzi

Tawanda James Zimudzi was born and raised in Borrowdale a suburb of Harare, where he attended Borrowdale primary school and later attended Vainona High where he was a prefect, a house captain for Johnson house and school vice head boy before graduating in 2003. Tawanda continued his education at the University of Zimbabwe where he pursued Chemistry. At the University of Zimbabwe, he worked under the mentorship of Dr. Zvitendo J. Duri studying the phytochemistry of indigenous plants. He graduated in 2009, receiving a first class Bachelor of Science in Chemistry with distinctions in analytical chemistry. Tawanda began graduate school in August of 2012 at The Penn State University, and began working under the tutelage of Prof. Michael A. Hickner in January of 2013 using vibrational spectroscopy to probe the structure and composition of thin polymer films.